JOINT INSTITUTE FOR AERONAUTICS AND ACOUSTICS

STANFORD UNIVERSITY

AMES RESEARCH CENTER

JIAA TR-23

AN EXPERIMENTAL STUDY OF MULTIPLE JET MIXING

A. Krothapalli, D. Baganoff,
and K. Karamcheti

STANFORD UNIVERSITY
Department of Aeronautics and Astronautics
Stanford, California 94305

JUNE 1979

JIAA TR - 23

AN EXPERIMENTAL STUDY OF MULTIPLE JET MIXING

A. KROTHAPALLI, D. BAGANOFF,
AND K. KARAMCHETI

JUNE 1979

The work here presented has been supported by the National Aeronautics and Space Administration under NASA Grant 2007 and NASA 2233 to the Joint Institute of Aeronautics and Acoustics

ABSTRACT

Results of hot-wire measurements in an incompressible jet issuing from an array of rectangular lobes, equally spaced with their small dimensions in a line, both as a free jet, and as a confined jet, are presented. The quantities measured include mean velocity and the Reynolds stress in the two central planes of the jet at stations covering up to 115 widths (small dimension of the lobe) downstream of the nozzle exit. Measurements are carried out in three parts: a) on a single rectangular free jet, b) on the same jet in a multiple free jet configuration, c) on the same jet in a multiple jet configuration with confining surfaces (two parallel plates are symmetrically placed perpendicular to long dimension of each lobe covering the entire flow field under consideration).

In the case of a single rectangular free jet, the flow field of the jet was found to be characterized by the presence of three distinct regions in the axial mean velocity decay and are referred to as: potential core region, two dimensional type region, and axisymmetric type region. In the case of a multiple free jet, the flow field for downstream distance X greater than 60D (D = width of a lobe) resembles that of a jet exiting from a two-dimensional nozzle with its short dimension being the long dimension of the lobe. The field of turbulence is found to be nearly isotropic in the plane containing the small dimension of the lobes for X greater than 60D. In the case of a confined multiple jet the flow field is observed to be nearly homogeneous and isotropic for X greater than 60D.

ACKNOWLEDGEMENTS

The authors gratefully acknowledge the support of NASA Ames Research Center under grants, NASA 2007 and NASA 2233.

Mr. David Hickey, of NASA Ames, provided valuable advice and ideas. Many people in the Joint Institute of Aeronautics and Acoustics contributed suggestions and assisted in the research. We thank all of these people for their generous help.

We would like to thank Mr. Michael Fancher, who initially worked on this project and aided in building the facility and through some experiments.

The facility, models, and many of the hot-wire probes were expertly made by Gerry deWerk, Vadim Matte, and Al Armes. In addition they offered many suggestions that improved the design of the experimental apparatus. Mr. William Janeway assisted in the design and operation of much of the electronics. Our thanks to all of them.

We express our sincere thank to Ms. Minnie Pasin who did an exceptional job in typing this manuscript. The help of Miss Jill Izzarelli is also appreciated.

NOMENCLATURE

AR	Aspect ratio (L/D)
b	Characteristic width of the jet
D	Width (small dimension) of the lobe
G	Gap between the leading edge of the plate and the nozzle exit plane
L	Length (long dimension) of the lobe
L_1	Spacing between the plates
N	Number of jets
p	Pressure
$\overline{q^2}$	$\overline{u^2} + \overline{v^2} + \overline{w^2}$
Re	Reynolds number, $U_o D/\nu$
S	Spacing between the lobes
U	Mean velocity component in the X-direction
U_c	Mean velocity component on the centerline of the jet in the X-direction
U_m	Mean velocity component on the centerline between the jets in the X-direction
U_o	Mean velocity component in the exit plane of the jet in the X-direction
U_s	Mean velocity component of the secondary flow in the X-direction
u	Fluctuation velocity component in the X-direction
$\sqrt{\overline{u^2}}$	rms velocity fluctuations in the X-direction
u_I	Instantaneous velocity in the X-direction
$\tilde{u}$	$\sqrt{\overline{u^2}}/U_c$ (normalized rms velocity fluctuation in the X-direction
V	Mean velocity component in the Y-direction

$\sqrt{\overline{v^2}}$	rms velocity fluctuation in the Y-direction
v_I	Instantaneous velocity in the Y-direction
$\tilde{v}$	$\sqrt{\overline{v^2}}/U_c$ (normalized rms velocity fluctuations in the Y-direction)
w	Mean velocity component in the Z-direction
$\sqrt{\overline{w^2}}$	rms velocity fluctuation in the Z-direction
w_I	Instantaneous velocity in the Z-direction
$\tilde{w}$	$\sqrt{\overline{w^2}}/U_c$ (normalized rms velocity fluctuations in the Z-direction
$\overline{uv}$	Component of the turbulent shear stress tensor
$\overline{uw}$	Component of the turbulent shear stress tensor
$\overline{vw}$	Component of the turbulent shear stress tensor
$\tilde{\overline{uv}}$	$\overline{uv}/U_c^2$ (normalized shear stress)
$\tilde{\overline{uw}}$	$\overline{uw}/U_c^2$ (normalized shear stress)
X	Coordinate along the jet axis
X_c	Crossover location of a single jet
Y	Coordinate along the small dimension of the lobe
$Y_{\frac{1}{2}}$	Local half width of the U profile along the Y axis
Z	Coordinate along the long dimension of the lobe
$Z_{\frac{1}{2}}$	Local half width of U profile along the Z axis
η	Y/X or Y/b
ξ	Z/X
ν	Eddy viscosity
ρ	Density

TABLE OF CONTENTS

LIST OF FIGURES

I INTRODUCTION

Several propulsive-lift concepts have been investigated as a means of obtaining short takeoff and landing (STOL) performance in turbofan-powered aircraft. The augmentor wing is one of such concepts being studied for application to commercial turbofan-powered STOL type aircraft. In this concept, a wing trailing edge ejector system is used to augment the high pressure fan bypass air. An ejector is a simple device in which turbulent entrainment by a jet of primary fluid is used to pump the secondary flow through a duct. Complete mixing of the primary jet and secondary entrained flow is required to achieve significant levels of augmentation.

The application of ejector thrust augmentation to STOL aircraft has, therefore, been an active research goal for several years. In the early 1960's the Canadian Defence Board developed a slot-type augmentor as shown in Figure (1.1) for STOL-type aircraft. During the later part of the 1960's research on a large scale was conducted at the NASA Ames Research Center. This work led to an effective augmentor that was appropriate for flight testing. But this type of augmentor was too noisy to allow commercial application. Since then the research activity was directed towards designing an augmentor wing with improved aerodynamics and reduced noise levels. Experimental investigations have shown that, by combining a lobed primary nozzle to enhance the turbulent jet mixing and an augmentor acoustic lining to absorb the jet mixing noise, a substantial reduction in augmentor noise can be achieved. Any further

reduction of the noise requires a more complete understanding of the nature of the flow field inside the augmentor.

Wind tunnel tests on the overall aerodynamic and noise measurements of an augmentor wing with multi-element nozzles and slot nozzles are reported by Aiken (1973). The results indicate that lobe nozzles offer improved static and wind-on aerodynamics and reduced static noise relative to slot nozzles. These tests led to a design configuration as shown in Figure 1.2. With these advantages in mind, a research project was initiated to investigate the basic fluid mechanical properties, such as the mean and turbulent quantities, of incompressible turbulent jets emanating from a linear array of lobes of equal dimension. The lobes used in this type of application are usually of rectangular cross section. The flow field of a single rectangular jet issuing into quiet surroundings was found to have the characteristics of both the two-dimensional jet and the axisymmetric jet. These two types of jets have been studied in some detail before; however, few experiments have been carried out on a rectangular jet with the degree of thoroughness found in either of the above two cases. Therefore, one of the objectives of the present study is to investigate the characteristics of a single rectangular free jet. This forms the first part of the present study.

Dual jets and coaxial jets have been a subject of investigation for several years and considerable amount of data is available for most engineering purposes. Some experiments have also been carried out on linear nozzle arrays consisting of several circular nozzles equally spaced along a straight line, but there appears to be a need for additional fundamental studies concerning the turbulent mixing of these

multiple jets, in particular, the linear array of rectangular jets. This constitutes the second part of the present investigation. The engineering problem which is of interest in the context of the present work is utilizing these multiple jets in an ejector configuration to augment the lift of an STOL-type aircraft. Most of the experiments which were done previously on this problem were aimed at measuring the gross characteristics of the flow field rather than the detailed turbulence structure of the flow. The third part of the present study is oriented towards understanding of the turbulence structure of these multiple jets in an ejector configuration.

The present study has the following main objectives to the general problem of the turbulent mixing processes in a multiple three-dimensional jet.

1. Investigate the characteristics of a single rectangular free jet.
2. Study the characteristics of the free jet in a multilobe configuration.
3. Include the confining surfaces, to simulate the flap and shroud, and determine the nature of the changes in the flow as a result of the confining walls.
4. Develop a semianalytical method for predicting the aerodynamic performance of a multijet configuration.

In the next chapter a review of previous work related to the problems of a single rectangular jet, single jet in a free multiple jet configuration and multiple jet ejectors is presented along with the nature of the present problem. Chapter III contains the description of

the experimental apparatus and instrumentation used for the present study. The test procedure including calibration of the measuring instruments is also presented. The results of the experiments are presented and discussed in Chapter IV. Chapter V has a brief introduction of Reichardt's inductive theory of turbulence and the application of this theory to the present problem of multiple rectangular free jets. Finally, the conclusions of this study and some recommendations for further research are contained in Chapter VI.

II REVIEW OF PREVIOUS WORK AND NATURE OF THE PRESENT INVESTIGATION

The present study comprises three problems as identified and listed in the Introduction. Results of individual studies of these three problems have been published in the literature in a form somewhat unrelated to one another. For the purposes of this review, it will be convenient to discuss separately the previous work in each area. Comparison will be made between the present study and previous studies wherever possible.

2.1 Single Rectangular Free Jet

Most of the previous investigations in turbulent jets were carried out on two-dimensional jets and axisymmetric jets. Sufficient experimental data are available in the literature to adequately define the structure and development of the flow field of these jets (Everett and Robins, 1978; Gutmark and Sygnanski, 1976; Hinze, 1975; Rajaratnam, 1976; Schlicting, 1968; Townsend, 1976; Wygnanski and Fiedler, 1969; and others). However, few experiments have been carried out on a rectangular jet with the degree of thoroughness found in either of the above two classes of jets. Early work on rectangular jets was done at the Polytechnic Institute of Brooklyn by Sforza and his co-workers (Sforza, Steiger and Trentacoste, 1966; and Trentacoste and Sforza, 1967). Their experimental study was mainly able to measure gross properties of the jet because of their use of the pitot tube. It was revealed from their experiments that the flow field of a rectangular jet

was characterized by the presence of three distinct regions as defined by the decay of square of the mean axial velocity along the axis of the jet. Discussion of these regions are deferred to Chapter IV. The mean velocity and temperature profiles of rectangular jets having different aspect ratios and nozzle geometries were measured using hot-wire anemometry by Sfeir (1975). He pointed out some of the effects of nozzle inlet geometry on the development of the jet. Some measurements of heated rectangular jets were reported by Sforza and Stasi (1977), and these indicated that the nature of the nozzle exit flow conditions play a large role in the development of the near field jet characteristics. Recently Sfeir (1978) reported some measurements of turbulence quantities, using hot-wire anemometry, for three different aspect ratio nozzles (10, 20, 30) with each having two different inlet nozzle geometries. Reference to these measurements will be made in Chapter IV. McGuirk and Rodi (1977) attempted to calculate the flow field using the two-equation turbulence model consisting of those for the turbulent kinetic energy and its rate of dissipation, in terms of which the turbulence stresses are expressed. They were able to calculate some of the observed features with some alternations in the specification of initial conditions.

Systematic measurements, such as those found for two-dimensional jets (Gutmark and Wygnanski, 1976), and axisymmetric jets (Wygnanski and Fiedler, 1969), are not available for a rectangular free jet. There appears to be a need for additional data, in particular, measurements at turbulence quantities to further extend the understanding of its fluid mechanical characteristics. An attempt is made in the present

investigation to provide some of these measurements for a rectangular free jet exiting from a nozzle of aspect ratio 16.7. Results and discussion of these experiments are presented in Chapter IV.

2.2 Free Jets in a Multilobe Configuration

Early work on this subject was done by Corrisin (1944) who studied the flow from seven parallel slot nozzles in a common wall with emphasis on flow stabilization methods. To ensure the two-dimensional character of the flow field, end plates were used normal to the slots and covering the entire flow field. This particular configuration is somewhat similar to the third problem of the present investigation; therefore, it will be discussed in the next section. However, some of the experiments were carried out without the use of end plates to study variation in the flow field. The nature of the flow was determined primarily by means of pitot tube measurements. He observed from these measurements that the jets were partially stabilized (indicated by the symmetric distribution of the total pressure about their axes) by the removal of end plates, permitting a net flow into the system along the axis parallel to the slots. In the present setup, the individual jets are ventilated at the exit of the nozzle, thus allowing flow into system.

In the late 1950's and early 60's a major effort was made to find a nozzle configuration that would serve as a noise-suppression device for turbojet engines. One class of such noise-suppression devices is a linear array of slots located quite close together. The individual jets from the slots pass downstream and mix both with the surrounding

atmosphere and with each other. This mixing results in a lower intensity of turbulence in the common zone between two jets than that found when the jet stands alone. Laurence and Benninghoff (1957) studied the flow field of a jet emanating from four rectangular lobes, where the long dimensions of the lobes are arranged in a line. The quantities measured were the mean velocity and rms values and the turbulent spectrum of the axial component of velocity. Their results show that the scale and intensity of turbulence are less in the common mixing zone of two interfering jets than in the corresponding zone of a single jet in the configuration. The flow field of the jet emanating from four rectangular lobes having their minor axes in line was studied by Laurence (1960). This configuration is similar to the one under study in the present investigation. He selected five different spacing-to-width ratios (S/D) ranging from 0.94 to 3.0. The results indicate that for the turbulent intensity, the eddy size, and spectral density functions, the maximum change occurs for a value of the spacing-to-width ratio of about 2.0. The maximum noise reduction was found to also occur at a spacing-to-width ratio of about 2.0. Measurements were not made at higher spacing-to-width ratios which are of interest in the present investigation.

The flow emanating from a series of closely spaced holes in line has been studied both experimentally and theoretically by Knystantas (1963). The theoretical prediction of the mean axial velocity was based on Reichardt's theory, which is explained in Chapter V of this report. Borchers and Goethert (1977) investigated noise radiation and effects of jet interference for linear nozzle arrays consisting of

several circular nozzles equally spaced along a straight line. Most of the emphasis in the study was placed on acoustic measurements rather than on basic turbulence measurements. Miller and Commings (1960) studied the force and momentum fields generated by identical twin jets of air issuing from parallel slot nozzles in a common wall. Similar studies were also reported by Tanaka (1970) and others. In this case two jets attract each other due to interference. A region of subatmospheric pressure between the converging jets accounts for their convergence. Far downstream the flow structure of the combined jet exhibits all characteristics of a single jet flow except for an altered evolution of the self-preserving turbulence distribution. However, the effect of convergence is not noticed when the jets are ventilated, as shown by the results of Marsters (1977) who studied the flow field of two plane, parallel jets. Recently measurements in the flow field of a linear array of rectangular nozzles are reported by Marsters (1979). Some of the mean and turbulence properties of the axial velocity component are presented. However, the results do not represent a detailed study of the configuration.

2.3 Multiple Jets in the Ejector Configuration

As mentioned in the previous section, Corrisin (1944) reported some experimental results of a flow downstream from a grid (two-dimensional) formed of parallel rods. Two end plates were positioned normal to the rods covering the entire flow field. Since there was no provision for secondary flow to enter the system, this configuration cannot fully resemble the ejector; however, the flow field from these two-dimensional jets, with the presence of end plates, may have some

relevance to the present problem. Some of the conclusions drawn from these experiments are as follows: (1) The flow field of parallel two-dimensional air jets downstream from the grid is unstable (indicated by an asymmetric total pressure distribution about the individual jet axes) for a grid density ($\frac{\text{covered area}}{\text{total area}}$) of 0.83. (2) The flow field can be at least partially stabilized by the "ventilation" of the spaces between the jets, permitting air to flow into the system in the direction parallel to the jet axis. Some of these observations were also made in the present investigation and the discussion of these results will be deferred to Chapter IV.

Ejectors using axisymmetric nozzles as the primary jet have been studied before both theoretically and experimentally, and the results are reported by Quinn (1978), Tia (1977), and several others. Quinn (1973), Bevilaqua (1975), and Salter (1975) showed that by using hypermixing nozzles for the primary jet, a high performance and compact-ejector can be designed. Overall aerodynamic studies have been conducted by Aiken (1973) on an ejector with multiple rectangular lobes with various spacing-to-width ratio and nozzle dimensions. From these studies it was found that the lobe-type nozzles improve static aerodynamic characteristics when compared with single slot type nozzles. A numerical method capable of modeling the turbulent mixing characteristics of three-dimensional primary jets has been developed by Dejoode and Patankar (1977). Predictions of mean velocities were made for the case of an ejector with hypermixing nozzles as the primary jet. The results are in good agreement with the experimental results. However, no attempt has been made in the previous investigations to study the

basic turbulent structure of a flow field which arises from the mixing of these multiple jets.

2.4 Nature of the Present Problem

The experimental studies mentioned above in addition to others have contributed to a limited understanding of the characteristics of a multiple jet configuration (both in free jet and ejector configurations). Very little is understood about the fundamental nature of the mixing phenomenon occurring between these multiple jets. In the present study a methodical set of measurements were made of simple turbulent quantities to evaluate the effects of the interaction of these jets both in a free jet configuration and in an ejector configuration.

In light of past experimental observations the features of the flow are expected to depend upon the following parameters (refer to the sketch below, also see Figure 3.7):

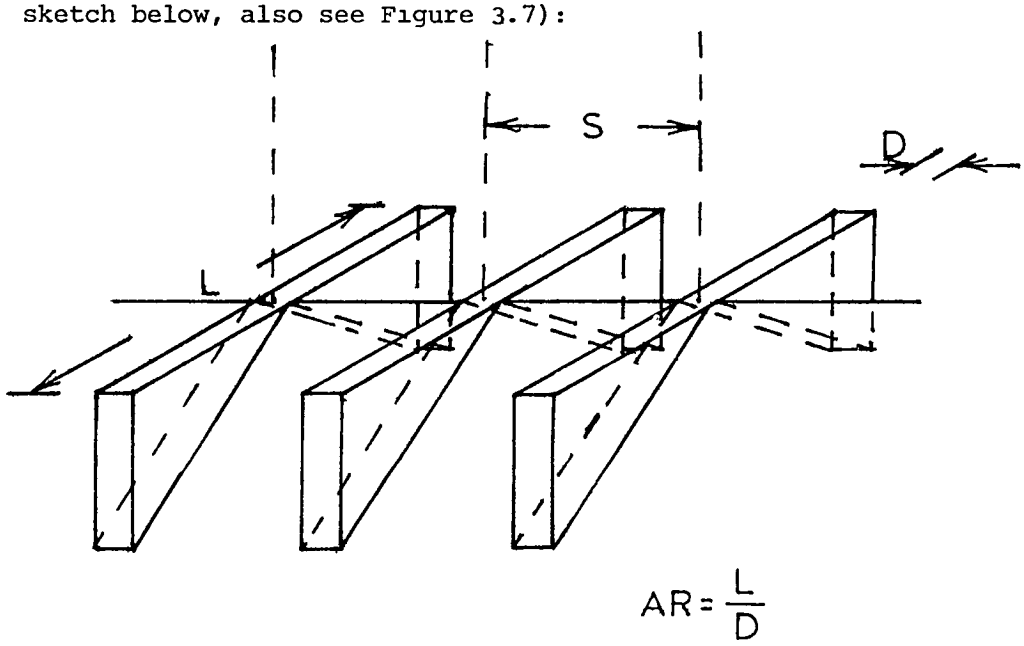

- The aspect ratio, L/D, of each lobe.
- Spacing, S, between the lobes.
- The inlet geometry of each lobe.
- Mach number of the jet exit flow.
- The Reynolds number, $Re = \frac{U_o D}{2}$, at the exit of each lobe.
- Type of exit velocity profile for each lobe.
- Conditions of the ambient medium into which jets are issuing.

If the multiple jets are confined between two surfaces (as shown in Figures 1 and 3.6) the following additional parameters will also enter into the problem.

- Geometry of the confining surfaces to simulate the flat and flap and shroud of the augmentor.
- The spacing between the confining surfaces.

Five rectangular lobes of equal dimensions in line were chosen for the present study. Most of the nozzle dimensions are taken from a NASA 1/3 scale augmentor wing model which was used by Aiken (1973) in his experiments. The inlet geometry of each lobe was designed to obtain a flow with minimum disturbance at the exit. As a first step in simulating the ejector, confining surfaces are introduced as simple flat plates. Hot-wire anemometry was used to make the measurements, and an exit velocity of 60 m/s was chosen for all the measurements reported. This results in a Reynolds number of 1.2×10^4 based on the small dimension of a single lobe. The exit velocity profile for all the lobes was a top-hat profile with a laminar boundary layer at the walls. The magnitude of the turbulence intensity was 0.3% at 60 m/s. The jets issued into a quiet ambient surrounding.

III EXPERIMENTAL APPARATUS, INSTRUMENTATION, AND PROCEDURES

3.1 General Considerations

Most of the gross characteristics of an augmenter wing with lobe-type nozzles were reported by Aiken (1973). A detailed survey of the mean and fluctuating quantities for a lobe-type nozzle (which consisted of a section of a 1/3-scale augmenter wing tested at NASA Ames Research Center) was conducted in the Aeroacoustics Laboratory at Stanford prior to the present investigation. These results have been reported by Fancher, Krothapalli, and Baganoff (1976, 1977). The non-uniformities in the inlet geometry of this nozzle introduced complexities in the flow field which caused many difficulties in interpreting the results. Based on this experience a research model was designed consisting of five rectangular lobes in a line. Most of the geometrical dimensions of the research model were taken from the previous model.

A comparison of the parameters pertaining to an experimental STOL research aircraft with the parameters that have been used in the present investigation is shown in the table below.

	Augmenter Wing	Experiment
Aircraft speed	$\leq$200 knots	0
Plenum pressure ratio	2-3	1.03
Lobe aspect ratio	0-15	16.7
Ventilation ratio	$\leq$10	$\tilde{}$10.0
Reynolds number (Based on lobe width)	40,000-130,000	12,000

The mean and turbulence measurements were performed using a linearized constant-temperature hot-wire anemometer. In the following, the different experimental equipment and measurement methodologies are described.

3.2 Air Supply System

The schematic of the air supply system is shown in Figure 3.1. A four stage compressor is used in conjunction with a 104 cu. ft. storage tank to provide a blow-down air supply with a peak pressure of 2800 psi. The four stage worthington type 280 compressor is able to raise the storage pressure at a rate of 150 psi per hour, thus requiring 19 hrs. to achieve full charge and making possible a 24 hr. test cycle. Figure 3.2 shows the calculated system run time/sq. cm. of nozzle as a function of initial supply pressure for a sonic jet. The run time for a nozzle consisting of five lobes, each measuring 5.0 cm × 0.3 cm, would then be nearly 20 minutes.

The high pressure air from the storage tank passes through a shut-off valve and a 0.5 μm filter before entering into a two-stage regulator control. In the first stage of the regulator the air pressure can be brought down from a supply pressure of 2800 psi to a maximum of 200 psia. A second stage regulator is connected in a feedback loop, and is used to control the pressure in the settling chamber. A relief valve which is set at 200 psia is used between the two stages of the regulator. After leaving the second stage regulator air passes through a second relief valve which is set at 120 psia, and a 5 μm filter before entering into the settling chamber.

A schematic of the settling chamber is shown in Figure 3.3 with the model in place. The air is injected into the settling chamber through a spray bar which helps in distributing the flow uniformly. The velocity of the flow in the settling chamber was measured and found to be very low (less than 1 m/s). To ensure a low turbulence level at the exit of the nozzle, six fine mesh screens were placed at 2 inches apart in the exit section of the settling chamber. These are shown in Figure 3.4. Following the screen pack, the flow enters into an adapter which connects the model to the settling chamber. The adapter with the original model is shown in Figure 3.4. In the present experiments the adapter was designed so that it allows the flow to make a smooth transition from a circular cross section at the exit of the settling chamber to the rectangular cross section of the model. The turbulence level at the exit of the nozzle was about 0.3% for an exit velocity of 60 m/sec. The total temperature in the settling chamber varies anywhere from 50^0F to room temperature.

3.3 Model

Most of the geometrical dimensions of the nozzle listed were obtained from an earlier study for which the model was constructed from a nozzle section supplied by NASA Ames Research Center. The nozzle model consists of five rectangular lobes, each measuring 5.0 cm × 0.3 cm, with the lobes spaced 2.4 cm apart. A design drawing of the model is shown in Figure 3.5. A picture of the model with the adapter and a close-up view are shown in Figure 3.6. To ensure a smooth secondary flow between the lobes a 70^0 triangular-shaped ventilation entry was employed.

All the measurements for the case of a single jet were performed on the center lobe with the remaining four lobes blocked. The aspect ratio of the center lobe was varied from 5.5 to 12.5 by introducing streamlined plugs into the lobe. The measurements of the multijet configuration are performed on the center lobe with all five lobes operating. To simulate the flap and shroud of the augmenter two parallel Plexiglas plates were added to the multilobe nozzle as shown in Figure 3.6. The leading edge of the plates are rounded with no fairing added as shown in the figure. The supports for the plates are designed such that the separation between them can be varied. A diffuser configuration can also be obtained by including an angle between the plates. The position of the leading edge of the plates can also be varied with respect to the exit plane of the lobes. Plates of 30 cm length were used in the experiment described in this report; however, this length can be varied if desired.

3.4 Nature of Measurements

To obtain a clear understanding of the structure of the flow field in three-dimensional turbulent jets, one requires at least the following measurements: mean quantities of the three components of velocity (u, v, and w), their rms values, and the Reynolds stress components. For a thorough understanding of the flow field these measurements should be made nearly everywhere in the flow field. In addition to these it is desirable to have some way to visualize the flow, so that the measurements can be interpreted more easily.

As a first step in understanding the fluid mechancial characteristics of multiple jets, the measurements were primarily confined to the

two central planes (xy and xz) of a center lobe in an array of five rectangular lobes (see Figure 3.7). Measurements include mean values of the three components of velocity, rms intensities for the three components of velocities, turbulent shear stresses ($\overline{uv}$ and $\overline{uw}$, see Figure 3.7), and the component spectra of the three components of velocity at some selected stations in the flow field. Some schlieren pictures were also taken to help visualize the flow. All the measurements were taken at a fixed Reynolds number (based on the small dimension of the lobe) of 12,000.

3.5 Flow Visualization System

The conventional schlieren technique has been adapted for flow visualization. A schematic of the system is shown in Figure 3.8a. The configuration is a single pass design with the light path folded twice, and uses a collimating lens and two ten-inch diameter, ten-foot focal-length spherical mirrors. The system was chosen to allow flexibility in converting from a schlieren to a direct shadow visualization arrangement. A schematic of the shadowgraph arrangement used is shown in Figure 3.8b.

The light source employed was a stroboscopic high intensity flash unit (U.S. Scientific Instruments, model 3015 stroboscope) that can be operated in two modes. First, it can be triggered manually to produce a single flash, as in a standard schlieren system. The second mode of operation is as a stroboscope. Operated in this mode any periodic motion in the jet can be frozen. The flash unit used in the present investigation provides five levels of light output, from 20×10^6 to

300×10^6 beam candles, and flash rates from a single pulse to 1,000 Hz. The duration of each flash is a function of the light intensity and varies from 1.25 to 7.0 microseconds. The standard flash lamp was replaced with a U.S. Scientific instruments ultrahigh intensity flash lamp (model HiCP-1) with an arc length of 1.0 mm. This lamp was mounted behind a metal plate containing a 1 mm diameter iris. All the photographs were taken using a single pulse from the light source. However, the stroboscopic light source was very valuable in observing the flow phenomenon with the naked eye.

3.6 Probe Traversing System

The traversing mechanism with the probe in position is shown in Figure 3.9a. The system has three translational and three rotational degrees of freedom. A three-axis probe traversing mechanism supplied by Velvex Corporation gave the three translational degrees of freedom. The rotational degrees of freedom were provided through a simple modification of a commercially available machine tool, a three-way vise made by the Universal Vise and Tool Company, which was attached to the traverse base as shown in Figure 4.9b. This unit allows virtually any orientation of the three orthogonal traverse axes. Such flexibility is necessary for establishing a model or flow-oriented coordinated system which is more convenient than some arbitrary laboratory system of coordinates.

The lead screws of the two horizontal axes of the traverse mechanism were automated with the installation of stepper motors and associated drive and control logic circuitry. The lead screw drive employs a stepper motor which is driven by a series of pulses, each pulse

causing the motor to rotate through a fixed angle. Thus, the total angular rotations can be determined by keeping track of the number of pulses sent to the motor. The logic of the stepper motor control circuitry has been designed to pass two pulses at a time, giving a minimum positioning increment of 10^{-2} mm, which is the increment marked on the lead screw hand-crank, and deemed satisfactory for position resolution. The probe can be moved continuously, or it can be advanced by increments, the size of which is selected by the operator. There is also provision for converting the numerical count into a proportional voltage which can be used to drive a scope or an x-y plotter. A mechanical coupling allows the motors to be disengaged from the lead screws for hand-cranking, if desired. The vertical axis differs from the two horizontal axes in that the lead screw may be cranked by hand or at a fixed speed by a Bodine induction synchronous motor rather than a stepper motor.

3.7 Hot-Wire Anemometry and the Associated Electronics

The Equipment

A DISA two-channel linearized constant temperature anemometry system was adopted to make the velocity measurements. The system is composed of two of each of the following instruments.

55M10	Main Unit Power Supply
55M10	Standard Bridge
55D10	Linearizer
55D31	Digital Voltameter
55D35	rms Voltameter

To calibrate the wires in a known velocity field, a DISA Type 55D90 calibration equipment was used. This includes the following units.

55D44 Pressure Control Unit

55D55 Nozzle Unit

55D46 Pressure Converter

This equipment is pictured in Figure 3.10 along with an x-y plotter used to record velocity voltage calibration curves. A regulated 12 bar air supply is provided for the calibration equipment by compressed air bottles in the laboratory. This equipment permits rapid and efficient calibration of hot-wire probes at velocities from 0.5 m/sec to approximately Mach 1, at a low turbulence level, with correction for compressibility. The calibration nozzle unit itself is provided with a probe mounting arrangement that allows determination of probe directionality characteristics, essential to the correct application of the x-wire measurement technique.

The signals from the linearizers were sent through a sum and difference unit which was calibrated from dc to 100 kHz. The signals were then passed through a DISA type 55D31 digital voltameter, DISA type D35 rms unit and TSI model 1076 voltameter to get the mean and rms values. The integration times on these instruments can be selected at discrete steps from 0.1 to 100 sec. Correlation measurements were made using an HP3721A correlator. The correlator is a digital instrument capable of computing and displaying, in real time, auto correlation, cross correlation and probability functions. Measurements of the component spectra were obtained using an HP8556A spectrum analyzer. It was capable of measuring frequencies ranging from 0 to 200 kHz, with a constant

bandwidth. The size of the bandwidth can be varied from 10 Hz to 10 kHz depending on the range of frequencies. A line drawing of this arrangement is shown in Figure 3.11.

3.8 Calibration and Interpretation of X-Wire Signals

Measurements of mean velocities, rms values, and turbulent shear stresses in a plane require the use of an x hot-wire system. Wires used here were 5 μm platinum-plated tungsten wires obtained from DISA (type P61).

To facilitate signal interpretation, the two wires must be calibrated in a test flow where the magnitude and direction of the flow are accurately known. The calibration of a constant-temperature hot-wire system is usually expressed directly in terms of the bridge voltage E, as a function of velocity V, using an equation similar to equation (1).

$$E^2 = E_o^2 + BV^2 \quad . \tag{1}$$

The experimentally determined calibration curve for E(V) represents the working information needed to use the hot-wire. The general form of equation (1) suggests that a signal processing circuit could be arranged to produce a linear relationship between E and V, i.e.,

$$E = KV \tag{2}$$

This linearization was achieved by using the DISA 55D10 type linearizer. The gains and exponents for each wire, entered in the corresponding linearizers, were set such that the outputs of both wires were the same

when exposed to identical flow conditions. The velocity interval selected for this calibration ranged from 10 to 70 m/s. The x-wire calibration was carefully performed by using the DISA type 55D90 calibration equipment.

The two wires of the x-array were oriented at 45^0 to the direction of the calibration flow as shown in Figure 3.12. The linearized outputs of both wire 1 and 2, precisely in the form traced by the x-y plotter, are shown in Figure 3.13, where the flow velocity is the independent variable. We note that the calibration curves for the two wires superpose so closely that they cannot be distinguished from one another.

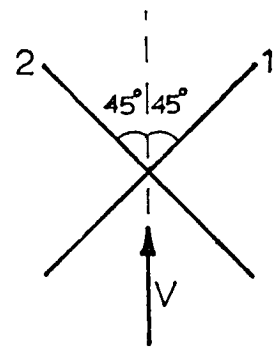

Figure 3.12

The directional sensitivity of each wire must also be quantified by a calibration scheme. The heat transfer rate between a wire and a fluid stream has a strong dependence upon the orientation of the wire with respect to the flow. Generally, one assumes that the heat transfer rate depends only upon the component of velocity perpendicular to the axis of the wire, this is often referred to as the "sine" or "cosine law", or simply as vector decomposition. The assumption that the component of flow velocity parallel to the heated wire does not contribute to the heat transfer from the wire is not strictly correct for a variety of reasons, but the effect is usually small. That the effect is small enough to be neglected in a given experiment, for a prescribed

level of accuracy, must, however, be confirmed by the calibration process. Using the simple cosine law, the decomposition equation becomes

$$V_{eff} = V \cos\alpha \tag{3}$$

The x-wire probe was mounted on a positioning gear located at the top of the nozzle calibration unit. The positioning arrangement allows the flow in the plane of the x-wire to be varied with respect to the axis of the probe in a known way. The probe was carefully oriented to match the output voltages of the two wires, and this orientation was used to define $\alpha = 45^0$ as shown in Figure 3.14. The plane of the x-wire was then adjusted precisely to match the plane of the positioning gear by the following procedure. Wire 2 was set normal to the flow by use of the positioning gear and the body of the probe was rotated about its axis until wire 1 gave a minimum output voltage. After making these adjustments, two calibration curves for angular displacement were obtained as shown in Figure 3.14. The output voltages of both wires were normalized with respect to the maximum output voltage of wire 2. The results indicate that there is a small asymmetry between the outputs of the two wires. This can be attributed to non-orthogonality of the two wires. In practice, it is very difficult to construct the two wires exactly perpendicular to each other. Because the calibration curves are used in the vicinity of $\alpha = 45^0$, the prediction for the u and v components of velocity by the use of vector decomposition requires only a small correction.

The percentage error in the predicted u component of velocity is shown in Figure 3.15, where percentage error is plotted against the

angle of incidence α. In the range $\alpha = 25^0$ to $\alpha = 75^0$ the error is within 1% of the value 4.5%. Because the v component goes to zero at $\alpha = 45^0$ and thus any error becomes infinite, the same format cannot be used to display the error. In this case the predicted v component is plotted against the experimentally derived value of v as shown in Figure 3.16. The dashed line represents perfect correlation, and the solid line represents the best fit of the data in the range $\alpha = 20^0$ to $\alpha = 70^0$.

These results suggest that the instantaneous velocity vector can only be allowed to fluctuate in the range $\alpha = 25^0$ to $\alpha = 70^0$. There is an asymmetry about the position $\alpha = 45^0$ because the two wires are not perfectly normal to each other. Use of this x-wire probe in turbulent flows is, therefore, confined to situations where the angular rotation of the velocity vector does not exceed $\pm 25^0$.

Temperature Compensation

A critical flow parameter to consider when interpreting a hot-wire anemometer output voltage in terms of velocity is the mean temperature of the flow, or more precisely, the difference, if any, between the temperature of the flow in which the probe was calibrated and that of the flow being measured. Often it is not convenient or even possible to perform the calibration at the same mean temperature to be found in the experimental flow, especially when that flow features a wide distribution of temperatures as well as velocities. These differences must be accounted for, however, since the response of the anemometer to the velocity field, that is, the heat transfer rate of the hot-wire, depends

strongly upon the difference in temperature between the heated wire and the fluid flowing around it. Temperature fluctuations may go undistinguished from velocity fluctuations, and a change in the mean temperature of the flow may be interpreted as a change in the mean velocity when in fact that velocity has not varied.

An effective means of correcting for such temperature changes is the use of so-called temperature-compensated probes and the corresponding bridge circuit. These probes feature two wires of identical composition. One wire is the unusual heated sensor while the other is connected to the opposite branch of the bridge and is not heated; this wire balances changes in resistivity of the heated wire due to thermal variations present in the flow, and thus in effect keeps the overheat ratio of the velocity sensor constant. The frequencies of the temperature variations that can be compensated for depend in an inverse manner on the thermal inertia of the unheated sensor, which depends on the diameter of the wire. To properly account for temperature fluctuations, the compensating sensor ideally would be exactly coincident with the velocity sensor; some compromise is, of course, necessary here.

Various configurations of temperature-compensated probes are available commercially, but all of these feature only a single velocity sensor; no temperature-compensated x-probes, with two velocity sensors and two compensation sensors, are to be had. Considering the large size of even the triple-wire sensors available, such a four-wire sensor, did it exist, would indeed be unwieldy and quite large in comparison to the lobed model under study.

In cold jet flows such as the one at hand the temperature fluctuations are relatively small though not necessarily negligible compared to the velocity fluctuations, but any difference between the calibration and experimental mean flow temperatures retains its importance. It should also be noted that locally normalized measurements such as turbulence intensities are little effected by mean temperature drift, since the effect there tends to cancel. For any absolute measurements the effect must be fully accounted for. The problem, then, remains of how to correct the output of the x-wire, which is to be the main tool of the multijet investigation, for mean flow temperatures different from that of calibration without the availability of a temperature-compensated x-probe.

Two alternative approaches have been considered. The first is to use 55M14 temperature compensator Bridge, with a DISA probe type 55P86 for measuring the mean velocity along the axis of the center jet. Thus, compare the results obtained from this method to the results of x-wire configuration. The second alternative is to use a correction formula to the linearized anemometer output of the x-wire. There are several correction formulas available in the literature, but the one used in these measurements is as follows.

$$(E - E_o)_{lin} = S \cdot U(1 - \frac{2\alpha}{a} \Delta Tm)$$

α = temperature-resistance coefficient = 0.0036^0C^{-1}

a = overheat ratio = 0.8

S = constant

E_o = is the measure voltage at U = 0

Tm = fluid temperature

Tmc = calibration fluid temperature

$\Delta Tm = Tm - Tmc$

3.9 Procedure

The experiment is divided in three parts, each one corresponding to three different aspects of the problem as described in the objective part of the Introduction. In the first part of the experiment the jet exiting from a single rectangular lobe, i.e., the center lobe has been surveyed. In the second part, the flow field of a multiple rectangular free jet is investigated. Profiles of the mean axial components of velocity were made for the three center lobes at different downstream locations and with all five lobes blowing. Detailed measurements were made only in the flow field of the center lobe with all five lobes blowing. Finally in the third part of the experiment, two end plates were introduced as shown in Figure 3.6. Again mean U profiles were measured across the three center lobes with all lobes blowing. The detailed measurements were made only in the flow field of the center lobe. The separation distance between the plates was varied to study its effect on the flow field.

All the measurements were made at an exit velocity for each lobe of 60 m/sec. This velocity was maintained constant at an accuracy of better than one percent.

A Cartesian coordinate system (x,y,z) was used as shown in Figure 3.7 with the x-axis oriented along the centerline of the jet. Hot-wire

traverses were made in the two central x,y and x,z planes at various stream-wise (x) locations covering up to 115D. Unless otherwise stated, all the data presented here were taken with the x-wire probe. Mean velocity measurements were made across the entire jet in order to establish the symmetry of the flow about its central planes; however, only the data for each half plane will be presented. For most of the present measurements errors were estimated to be of the order of 2 $\sim$ 3 percent and a systematic error in the axial component of velocity (due to cosine law decomposition) of approximately 5 percent was present.

IV RESULTS AND DISCUSSION

This chapter is divided into three sections, each being concerned with one of three parts of the problem. The first section presents the results of a single rectangular free jet. The second section deals with the results of multiple free jets, and finally, the last section is concerned with the results of multiple jets in an ejector configuration. Interpretations and discussions are presented together with the data.

4.1 Single Rectangular Free Jet

On the basis of the present investigation and the results reported by Sforza et al. (1966, 1967), Sfeir (1975, 1978), and those summarized by Rajaratnam (1976), the flow field of a rectangular jet may be represented schematically as shown in Figure 4.1. Also shown in the figure (as an insert) is the variation of $\ell n(U_c/U_o)^2$ with ℓn X/D. The three regions, as shown in the figure may be classified as follows: the first region is referred to as a potential core region in which the axial velocity is constant; the second region marked by AB, in which the velocity decays at a rate roughly the same as that of a planar jet, will be referred to as the two-dimensional region; and the third region downstream of B, in which the velocity decays at nearly the same rate as that of an axisymmetric jet will be referred to as an axisymmetric region. The two-dimensional type region originates at about the location where the two shear layers in the X,Y plane (containing the short dimension of the nozzle) meet. Correspondingly, one may expect that

the axisymmetric region to originate at the location where the two shear layers in the X,Z plane (containing the long dimension of the nozzle) would meet. This will be discussed further below.

Profiles of the mean axial velocity in the X,Y and X,Z planes at three different locations are shown in the schematic of flow structure in Figure 4.1. In regions I and II, the width of the jet in the X,Z plane is greater, as expected, than the width in the X,Y plane. At B the widths in both planes are about the same. In region III, the width in the X,Y plane becomes larger than that in the X,Z plane.

The solid and dashed lines shown in the flow schematic depict the loci of maximum turbulent stresses in the two planes being considered. Further discussion of this will be given later.

4.1.1 Mean Velocity Field

Figure 4.2a shows, for a nozzle of aspect ratio 16.7, the measured decay of the square of the axial velocity along the centerline. The three regions noted in Figure 4.1 are identified as the potential core region which ends at approximately 4D, the two-dimensional jet type region extending up to about 60D, and the axisymmetric jet type region extending beyond 60D. In regions II and III, U_c^2 , as indicated by the dashed lines, decays as X^{-1} and X^{-2}, respectively. Results obtained using the temperature-compensated probe are also plotted in the figure to show the effect of the temperature variation on the mean velocity measurements, along the jet axis. For X greater than or equal to 30D, the temperature-compensated probe data result in higher velocities when compared with the X-wire data. The calibration procedure and

usage of these (temperature-compensated) probes are not well-documented in the literature and thus the data should be treated with some caution.

The extent of these regions (as shown in Figure 4.1 and 4.2a) were shown by Trentacoste and Sforza (1967) and Sfeir (1975, 1978) to be functions of both the initial geometry and the aspect ratio of the nozzle. To identify the effects of aspect ratio on these regions, three additional aspect ratio nozzles of 5.5, 8.3 and 12.5 were tested. Results of the decay of the square of the mean axial velocity with downstream distance for these nozzles are shown in Figure 5.2b. As the aspect ratio decreases, the position of point B, that is where the centerline velocity first assumes the axisymmetric character, moves upstream toward the exit of the jet. From these measurements and the results of Sforza et al. (1967, 1978) and Sfeir (1975, 1978), one finds that for nozzles of aspect ratio less than or equal to 10 U_c^2 in region II does not decay as X^{-1}. The exponent in this power law decay is dependent on orifice geometry as shown by Sferi (1978) and on the aspect ratio.

Figure 4.3 shows the distribution of mean velocity U across the jet in the X,Y plane at different downstream stations, ranging from 20 to 100 widths. The velocity U is normalized with respect to U_c at each station, while the distance Y is normalized by the distance X to the station in question (η = Y/X). The profiles are geometrically similar, within the limits of error for the experiment, for X greater than or equal to 30D. The results of Sfeir (1978) and Gutmark and Wygnanski (1976) for nozzle aspect ratios of 10 and 38, respectively, are plotted for comparison. The agreement between the three sets of data is good for η less than or equal to 0.1, but for η greater than 0.1 the

profiles from the present investigation are somewhat wider than the rest. The shape of the profiles from these three sets of data seem to be similar. From these observations it appears that the aspect ratio does not play a critical role in determining the shape of the similarity profile in the X,Y plane, at least for aspect-ratios greater than 10. However, Everette and Robins (1978) reported that the downstream distance where the profiles first assume self-similarity appears to be directly related to the nozzle aspect ratio. This similarity persists both in regions II and III as shown in the figure. Often one nondimensionalizes the distance Y with respect to the local half-width of the jet $Y_{\frac{1}{2}}$ (the width corresponding to the point where the mean velocity is equal to one-half of its value on the axis). As discussed later, the half-width in the present investigation varies linearly with X. This being the case, the parameter η, but for a scale factor, represents equally the ratio $Y/Y_{\frac{1}{2}}$. For comparison purposes, the error function $\exp[0.5(Y/Y_{\frac{1}{2}})^2]$ of Reichardt's analysis (1944) for a two-dimensional jet is also shown in the figure, and seems to agree satisfactorily with the present measurements.

Normalized mean velocity profiles in the X,Z plane for different downstream locations are shown in Figure 4.4. The distance Z is again normalized with respect to the local longitudinal distance, $\xi = Z/X$. For locations X less than or equal to 60D, profiles have a saddle shape with the maximum velocity occurring near the centerline of the jet. The magnitude of the overshoot seems to be dependent on the type of the initial geometry of the jet (Marsters, 1979). This has also been noted by others (Sforza et al. (1967, 1978), Sfeir (1975, 1978),

Marsters (1979), Bradbury (1965) and VanderHegge Zigen (1957)). As suggested by VanderHegge Zigen (1957), such a profile may be explained as resulting from the superposition of a uniform stream with the flow due to a system of vortex rings representing the jet. However, more detailed study of the flow field is needed to understand clearly the origin of such profiles. At large distances downstream, i.e., for X greater than 80D, the profiles appear to have a shape similar to that of an axisymmetric jet. The similarity profile of an axisymmetric jet reported by Wygnanski and Fiedler (1969) is shown for comparison. It is also observed from Figures 4.3 and 4.4 that the velocity profiles at X equal to 60D in both planes are almost identical, and at this location the centerline velocity first assumes the axisymmetric character. True axisymmetry (profiles are identical in both planes) of the mean velocity profiles was observed by Trentacoste and Sforza (1967) far downstream of the jet (i.e., for X greater than or equal to 150 for aspect ratio of 10). In the present investigation, measurements are not made far enough downstream to confirm this.

The growth of the jet in X,Y and X,Z planes with downstream distance is shown in Figure 4.5a. The ordinate $Y_{\frac{1}{2}}$ and $Z_{\frac{1}{2}}$ are the distances from the centerline of the jet to the point where the axial mean velocity in each plane is equal to one-half of its centerline value. The jet in the X,Y planes spreads linearly with X and the locus of the half-velocity points is given by

$$Y_{\frac{1}{2}} = k(X - X_o)$$

where k = 0.109 and X_o = -2.5D. For planar jets the value of k varies between 0.09 and 0.12 and a listing of these values for various experiments is given by Katsovinos (1976). Similarly, the value of X_o for the different experiments also varies. The variation of these constants can be attributed to different initial conditions and the free stream turbulence level (Bradshaw, 1966, 1977). As discussed later, these also depend upon the aspect ratio of the nozzle.

The variation of the half-width in the X,Z plane as shown in Figure 4.5a is neither linear nor does it increase monotonically. At some intermediate location (X ≃ 60D for AR = 16.7) the half-widths in the central planes cross over which corresponds to the point B in Figure 4.1. The distance from the nozzle exit to the crossover point along the X axis is denoted by X_c. For comparison purposes, the results of Sfeir (1978) for a nozzle aspect ratio of 10 and for different inlet geometries are shown in the figure. It is noted that $Y_{\frac{1}{2}}$ exhibit linear variation for different aspect ratios, although the slopes of the lines are different for different inlet geometries. Although the variation of $Z_{\frac{1}{2}}$ exhibits similar characteristics in the two studies compared in the figure, significant differences are found owing to different inlet geometries. It appears that the inlet geometry plays an important role in the development of the jet in the X,Z plane.

To observe the effect of aspect ratio on the growth of a jet, three additional aspect ratio nozzles are tested and the results are presented in Figure 4.5b. It is observed that $Y_{\frac{1}{2}}$ exhibits linear variation for different aspect ratios, although the slopes of the lines are different for different aspect ratios. The variation of $Z_{\frac{1}{2}}$ exhibits

similar characteristics for all four aspect ratios studied. As shown in the figure, the distance X_c (downstream location of the crossover point) increases with aspect ratio.

The variation of X_c with aspect ratio is plotted in Figure 4.6. The results of Sforza et al. (1967) and Sfeir (1975) are also included in the figure. From the data of Sfeir it appears that, for a given aspect ratio, X_c appears further downstream for a jet exiting from a long channel than for a jet exiting from an orifice. This indicates that X_c depends strongly on the character of the initial flow. For aspect ratios greater than 10 it appears that X_c varies linearly with X as shown by the shaded region.

The mean lateral velocities in the two central planes were measured and are shown in Figures 4.7 and 4.8. These velocities are a small fraction (5-6%) of the mean axial velocity, thus an experimental accuracy of about 20 percent was the best attained. Furthermore, large errors are inherent in using hot-wire anemometry in the outer regions of the jet. Profiles of the mean velocity V in the central X,Y plane for different downstream locations are shown in Figure 4.7. They are geometrically similar for $30D \lesssim X \lesssim 60D$ and have the expected distribution. Very little entrained flow (indicated by the negative V component of velocity) is found in the outer region of the jet for X greater than 20D.

The mean W component of velocity in the central X,Z plane for different downstream locations is plotted in Figure 4.8. For most of the profile at X equal to 20D, the W component of velocity points toward the axis of the jet (indicated by the negative values). This behavior is consistent with the growth of the jet in X,Z plane. More detailed

measurements in the entire cross-section plane are required to interpret these results properly.

4.1.2 RMS Intensities and Shear Stresses

The rms values of the three components of velocity fluctuations on the centerline of the jet are shown in Figure 4.9. These values are normalized with respect to the local mean axial velocity on the center line. The magnitude of $\tilde{u}$ increases sharply close to the jet exit and reaches a maximum value of about 0.195 at X equal to 10D. It then decreases and increases again gradually. Such a behavior, for X less than 30D, is typical of a jet with laminar top-hat profile (starting boundary layers are laminar) at the exit plane and which goes through a transition region before it becomes a turbulent jet. This has been observed by Sato (1960) for a two-dimensional jet. The variation of $\tilde{u}$ with X has been observed to depend upon the state of the initial boundary layers at the nozzle exit. See, for instance, Hill et al. (1976) for a rectangular jet of aspect ratio 10.5 and Bradshaw (1966) for an axisymmetric jet. They found that when the initial boundary layers are laminar, $\tilde{u}$ varies as discussed above while, when the boundary layers are turbulent, $\tilde{u}$ varies monotonically with X.

The results of Sfeir (1978) for a jet of aspect ratio 10 and those of Gutmark and Wygnanski (1976) for an aspect ratio of 38 are included in Figure 5.9 for comparison. In both cases, the exit velocity profiles were top-hat distributions. On examining the variations of $\tilde{u}$ with X close to the jet exit, one may conclude that the boundary layers in these two cases were likely turbulent. From these observations, we

note that both the state of the boundary layer at the nozzle exit and the aspect ratio affect the way $\tilde{u}$ varies with X as well as its absolute magnitude.

To account for the temperature variation in the jet, a DISA temperature compensated probe was used to make some additional measurements. The rms values obtained with this method, which are denoted by $\tilde{u}_t$, are shown in Figure 4.9. The difference between $\tilde{u}$ and $\tilde{u}_t$ are quite small.

The variation of $\tilde{v}$ and $\tilde{w}$ along the centerline as shown in Figure 4.9 also exhibit characteristics similar to $\tilde{u}$. In the fully developed region of the jet, i.e., for X greater than 30D, the magnitude of $\tilde{u}$ is greater than that of either $\tilde{v}$ or $\tilde{w}$, as is also found in other free shear layer flows.

In investigating the effect of the initial boundary layer on jet mixing, Hill et al. (1976) studied the flow by means of spark schlieren photographs. They found coherent large scale structures in the jet shear layer when the initial layer was laminar. When it was turbulent, such structure was not observed. A typical schlieren picture (with an exposure time of 5 μs) of the jet flow in the present investigation is shown in Figure 4.10. Here, large scale structure is observable, as in the case of Hill et al. (1976), for the laminar top-hat profile present in the experiments.

To further examine the large scale structure, oscillograph records of u fluctuations along the centerline of the jet, for $2D \leq X \leq 20D$, are shown in Figure 4.11a. Oscillograms of the autocorrelation function for the respective signals are shown in Figure 4.11b, where the scale for the time variable is in microseconds. Figure 4.11c shows the

frequency spectrum of the u fluctuations along the centerline of the jet. The horizontal scale is kilohertz. Close to the jet exit (i. e., at X equal to 2D), strong periodicity is observed in both the time signal and the autocorrelation function. A strong distinctive peak is observed in the spectrum at about 5800 Hz. Some periodicity remains in the signal for stations up to 10D. This is also shown by their respective autocorrelation functions. The position of the distinct peak in the frequency spectrum observed for X < 10D moves slightly with downstream distance. With increasing distance, downstream of the jet, the spectral energy shifts toward the low frequencies as shown in the figure. At 20D the oscillograph record of the u fluctuation resembles a typical signal in a turbulent flow field. The autocorrelation function is also typical of a turbulent flow. Most of the energy in the frequency spectrum is in the low frequencies (i.e., less than 10 kHz). Similar measurements were also made for the v and w fluctuations and the results show features similar to the ones discussed above. Measurements of this kind were also made at locations off the centerline of the jet, and no significant differences were found. From these observations along with the schlieren pictures, one may conclude that discrete frequencies appear only in the initial stages of transition from laminar to turbulent flow.

Profiles in the X,Y plane of $\tilde{u}$, $\tilde{v}$ and $\tilde{w}$ at different downstream locations X are shown in Figures 4.12-4.14. The $\tilde{u}$ profiles indicate geometrical similarity for $30D \leq X \leq 60D$ and show a distinct saddle shape. Similar measurements have been made by Sfeir (1978), and he concluded that the profiles across the jet are self-similar for all X greater than 30D. However, after careful examination of his data and in light

of the present measurements, it is noted that both sets of data (Sfeir, 1978, and present investigation) are fully similar only in the so-called two-dimensional region of the jet (see region II of Figure 4.1). The maximum value of $\tilde{u}$ occurs at $\eta \simeq 0.075$. The $\tilde{u}$ profiles for two-dimensional jets show fairly large variations from one investigation to another (see Figure 5 of Everett and Robins, 1978). A typical profile of Everett and Robins (1978) is plotted for comparison. In general, the shape of the profile agrees with present measurements. For locations of X greater than 60D (i.e., in the so-called axisymmetric region) the profiles assume an axisymmetric character (see Figure 4 of Wynganski and Fiedler, 1969).

The profiles of $\tilde{v}$ and $\tilde{w}$ are shown in Figures 4.13 and 4.14, respectively. In the two-dimensional region, each of these profiles shows behavior similar to that of a two-dimensional jet.

It is sometimes useful to study the spatial distribution of the turbulent kinetic energy per unit volume, which is one-half the sum of the Reynolds normal stresses $\frac{1}{2}\rho(\overline{u}^2 + \overline{v}^2 + \overline{w}^2)$. The normalized turbulent energy distribution in the central X,Y plane for various downstream locations are shown in Figure 4.15. The distribution in region II is similar to that of a two-dimensional jet and has a saddle shape. The maximum value of $\overline{q}^2$ occurs at $\eta = 0.075$. In the central region of the jet ($\eta \leq 0.1$), profiles for X greater than 60D (i.e., in region III) show a character similar to that of an axisymmetric jet with magnitudes greater than those in region II.

Profiles of $\tilde{u}$, $\tilde{v}$ and $\tilde{w}$ in the X,Z plane are shown in Figures 4.16-4.18. It appears when comparing the $\tilde{u}$ profiles in Figure 4.16 with the

corresponding mean velocity profiles in Figure 4.4 that the point of maximum turbulence intensity coincides with the point where the velocity gradient ($\partial U/\partial z$) is maximum. The $\tilde{u}$ profile in the X,Z plane develops a strong saddle shape for X greater than 60D as shown in the figure. The appearance of a saddle-shape profile in a jet usually indicates the end of the so-called potential core, which marks the merging of the two shear layers of the jet. With this in mind, it may be argued that the two shear layers from the long dimension of the nozzle, in the present investigation, meet at X $\simeq$ 60D.

The profiles of $\tilde{v}$ and $\tilde{w}$ in the X,Z plane are shown in Figures 4.17 and 4.18, respectively. At each downstream location the magnitudes of $\tilde{v}$ and $\tilde{w}$ are about the same at their corresponding positions in the lateral direction (i.e., along the Z axis).

The normalized turbulent energy ($\bar{q}^2$) distribution across the jet in the X,Z plane for different downstream locations are shown in Figure 4.19. As observed earlier, a strong saddle shape in the distribution occurs for locations of X greater than 60D.

The normalized turbulent shear stress $\widehat{uv}$ in the X,Y plane for different downstream locations is shown in Figure 4.20. The stress is normalized with respect to the square of the local centerline velocity. The profiles are geometrically similar for X greater than or equal to 30D. The maximum value is observed at $\eta \simeq 0.075$, and this is also where the gradient ($\partial U/\partial y$) and the turbulent energy in region II were found to be maximum. The similarity profiles given by Gutmark and Wygnanski (1976) and Sfeir (1978) represent the shape well but not the ordinant of the mean profile drawn through the data in Figure 5.20. The

magnitude of the normalized turbulent shear stress $\widetilde{uw}$ was found to be much less than that of $\widetilde{uv}$ at corresponding locations in the X,Y plane.

Figure 4.21 shows the normalized shear stress $\widetilde{uw}$ profiles in the X,Z plane. At each location X, the point of maximum shear stress corresponds to the point of maximum velocity gradient ($\partial U/\partial z$) and the point of maximum turbulent energy. In region III, at any given X, the magnitude of the maximum uw in the X,Z plane is found to be greater than the maximum uv in the X,Y plane. At each location X, for both the X,Y and X,Z planes, the point of maximum shear stress corresponds to the point of maximum $\tilde{u}$, $\tilde{v}$, and $\tilde{w}$. The loci of these points are shown in the flow schematic of Figure 4.1.

4.2 Multiple Rectangular Free Jet

A schematic of the flow field of a multiple rectangular free jet is shown in Figure 4.22. Mean velocity profiles in the two central planes for the center three nozzles are shown in the figure. For the configuration tested (for S/D = 8, AR = 16.7), the flow from each lobe does not exhibit any mutual interaction for X less than 15D. Complete merging of the jets (i.e., individual jets lose their identity) is observed for X equal to 60D, and is indicated by a flat velocity profile across the lobes. The mean velocity in the central X,Z plane at different downstream locations exhibit characteristics similar to that of a single free jet. The shaded region is an attempt to show the pseudo-potential core region, after which the jet acts like a single two-dimensional jet with its minor axis being along the Z axis.

4.2.1 Mean Velocities

Mean axial velocity profiles in the central X,Y plane for the center three lobes at various downstream locations covering up to X equal to 60D are shown in Figure 4.23. These profiles were plotted with an X-Y recorder with the input to the X axis connected to the position sensor of the probe and the input to the Y axis connected to the output of a digital voltameter, the input of which is the linearized output of a single normal hot-wire. The integration time on the digital voltameter was held at one second. At the exit plane, top-hat profiles having equal magnitudes were found with very little secondary flow between the jets. Significant merging of the jets first seems to occur at a location of about 18D. The flat profile establishes that complete mixing of the jets has occurred at a location of approximately 60D. Velocity profiles are observed to be flat across the center three jets for locations $60D < X \leq 115D$.

For the configuration studied, a significant region exists where the mean velocity profiles of the individual jets behave quite independently of each other. A similar phenomenon was also observed by Marsters (1977) for the case of two ventilated parallel plane jets. However, two unventilated parallel plane jets, such as the ones studied by Miller and Cummings (1960) and Tanaka (1974), show a subatmospheric pressure region between the jets near the nozzle exit, and the jets attract each other. To further examine this phenomenon, a short exposure (5 μs) schlieren picture was taken of the center three lobes, and is shown in Figure 4.24. Here it is observed that the individual jets do not attract each other, and mixing with ambient air takes place quite

independently. The large scale structure such as that observed in the single free jet can also be seen clearly in the picture. The flow exiting from each lobe seems to be identical for the center three lobes.

The profiles were found to be symmetric about their individual jet axes; therefore most of the detailed measurements are made from Y equal to zero to Y equal to 4D (midway between two adjacent jets) along the positive Y axis. The measurements discussed below were made only in the two central half-planes of the center lobe.

The decay of the square of the mean axial velocity for both single-jet and multiple free-jet configuration is shown in Figure 4.25. The results for the two cases are identical up to X equal to 40D. For locations X greater than 40D, the decay is slower, as shown in the figure. The dashed lines in region II and region III represent the characteristic decay of a single two-dimensional jet and an axisymmetric jet, respectively.

The normalized mean velocity profiles in the X,Y plane for the center jet are shown in Figure 4.26 for the cases of single jet and multiple free jet. The profiles upstream of the merging region agree quite well as depicted by a typical profile at X equal to 10D. A nearly flat profile is observed at 60D.

The normalized mean velocity profiles in the central X,Z plane are shown in Figure 4.27 for various downstream locations covering up to 100D. For X less than or equal to 40D, the profiles exhibit a saddle shape with the maximum appearing near the centerline, and are identical to that of a single jet when compared at their corresponding locations. Profiles for X greater than 40D, in the multiple jet case are broader

than that of a single jet at their corresponding downstream locations. To further examine this, the growth rate in the X,Z plane of the center jet in both the single and multiple jet configurations are plotted with downstream distance in Figure 4.28. The growth rate in the X,Y plane for a single jet is also included in the figure. As one expects from the above discussion, the growth rate of the jet in the X,Z plane for both cases is almost identical up to X equal to 40D. For X greater than 40D, growth rate in the multiple jet configuration is greater than that of a single jet. From these observations, it may be concluded that, for the spacing studied, the mutual interaction between the jets is strongly felt at about X equal to 40D, while significant merging of the jets in the central X,Y plane occurs at X equal to 20D.

4.2.2 RMS Intensities and Shear Stresses

The rms intensity for the axial component of velocity along the centerline of the jet for both the single and multiple jets is shown in Figure 4.29, along with the results (data represented by a solid line) of Gutmark and Wygnanski (1976) for a planar jet. The rms intensity is normalized with respect to the mean axial velocity at the exit rather than with the local mean centerline velocity. With this type of normalization that any changes in the absolute value of the intensity can be brought out very clearly. The rms values are almost identical in both cases for X less than 40D, and a maximum value of about 0.125 occurs at a location of X equal to 10D. For X greater than 40D, the magnitude is less than that of a single free jet, as shown in the figure. This substantial reduction in magnitude is the result of a mutual

interaction between the adjacent jets. The results for a planar jet are shown for purposes of comparison, and are seen to exhibit values higher than that of a single rectangular jet. It is felt that this difference can be attributed to different initial conditions in the two experiments as discussed 4.1.2.

The normalized rms intensities $\tilde{u}$, $\tilde{v}$ and $\tilde{w}$ along the centerline of the center lobe are shown in Figure 4.30. The variation $\tilde{u}$ is almost identical to that of a single jet for X less than 40D. For X greater than 40D, it reaches a constant value of about 0.12. The quantities $\tilde{v}$ and $\tilde{w}$ have a behavior similar to that of $\tilde{u}$. For X greater than 60D, the magnitudes of $\tilde{u}$, $\tilde{v}$ and $\tilde{w}$ are about the same ($\tilde{v} = \tilde{w} = 0.9\ \tilde{u}$), which suggests isotropy along the centerline of the jet. This is not the case in a single free jet, where the magnitude of $\tilde{u}$ is higher than that of either $\tilde{v}$ or $\tilde{w}$.

The $\tilde{u}$ profiles in the X,Y plane for different downstream locations are shown in Figure 4.31. Profiles for X less than 20D are almost identical to a single free jet when compared at appropriate locations. For X greater than or equal to 60D, the profiles become flat just as the mean velocity profiles. Similar observations are also made from the $\tilde{v}$ and $\tilde{w}$ profiles in the X,Y plane, as shown in Figures 4.32 and 4.33, respectively. For X greater than 60D it is noted that the magnitudes of $\tilde{u}$, $\tilde{v}$ and $\tilde{w}$ are nearly equal across the lobes, which suggests isotropy in the central X,Y plane.

The profiles of $\tilde{u}$ in the X,Z plane for various downstream locations covering up to 100D are shown in Figure 4.34. For X less than 40D, the profiles are similar to those for a single free jet. For X greater

than or equal to 60D, the profiles develop a pronounced saddle shape as shown in the figure. The appearance of a saddle shape profile in a jet usually indicates the end of a potential core. The ratio of $\tilde{u}_{max}/\tilde{u}_{center}$ is about 1.5, which is higher than that observed in a single free jet. The larger the ratio, the stronger is the indication that the measurements are made close to a potential core. With this in mind, one may conclude that the flow field appears as though it is emerging from a single two-dimensional slot with the width of the slot being the long dimension of the lobe. The shaded region in Figure 5.23 was drawn to represent a pseudopotential core for this equivalent two-dimensional jet which ends at X equal to 60D.

The profiles of $\tilde{v}$ in the X,Z plane are shown in Figure 4.35. For X greater than or equal to 60D, the profiles exhibit a saddle shape. This further supports the above discussion. However, $\tilde{w}$ profiles, which are shown in Figure 4.36, do not exhibit a significant saddle shape, which is consistent with the observation of the profiles at the end of a potential core of a two-dimensional jet. In the outer portions of the jet (i.e., for $\xi > 0.15$) the magnitudes of $\tilde{v}$ and $\tilde{w}$ are the same for X greater than 40D. For X greater than 40D, the magnitudes of $\tilde{u}$, $\tilde{v}$ and $\tilde{w}$ are lower when compared with that of a single jet at corresponding downstream locations.

To further examine the degree of isotropy in the central X,Y plane, the normalized turbulent shear stress $\widetilde{uv}$ for different downstream locations are plotted in Figure 4.37. The stress, as before, is normalized with respect to the square of the local centerline velocity. For X equal to 20D, the profile is quite similar to that of a single free jet.

For X greater than 60D, the normalized stress is quite small in contrast to a single jet where it varies only slightly with downstream distance. The normalized turbulent shear stress $\widetilde{uw}$ in the X,Y plane is found to be negligible for all the downstream stations measured.

The normalized turbulent shear stress $\widetilde{uw}$ in the central X,Z plane for various downstream locations are shown in Figure 4.38. At each location X, the point of maximum shear stress corresponds to the point where the velocity gradient ($\partial U/\partial z$) and turbulent intensities are maximum. It is again found, when compared with that of a single jet, that the values of uw for X greater than 40D are less at corresponding locations. In addition, the magnitudes of uv are negligible in the central X,Z plane.

From these measurements it is observed that the magnitudes of the turbulence quantities for X greater than 40D was found to be less in both the X,Y and X,Z planes, when compared with those of a single jet at corresponding locations. This reduction in magnitude can be attributed to two causes: (1) Most quantities are normalized with respect to the local centerline velocity. In the multiple jet case, for X greater than 40D as shown in Figure 4.26, the centerline velocity decays much slower than that of a single jet. However, this in itself is not the complete explanation. (2) The reduction in magnitude is also due to the mutual interaction of the adjacent jets, and this is clearly shown in the variation of $\sqrt{\bar{u}^2}$ along the centerline of the jet. This seems to be the major contribution to the reduction in all of the turbulence quantities. To further understand this interaction, one needs to make additional detailed measurements such as the two-point space time correlations in the flow field.

4.3 Multiple Jet in an Ejector Configuration

A schematic of the configuration under consideration is shown in Figure 4.39. As before, the long dimension of the lobe is denoted by L (equal to 5 cm), while the spacing between the plates is denoted by L_1. The separation distance L_1 can be varied from 6 cm to 7.5 cm. The gap G as shown in the figure can be adjusted to a location where the maximum secondary flow is induced. Most of the detailed measurements were made in the two central planes X,Y and X,Z of the center lobe. For most of this section the data of the two central half-planes will be presented.

4.3.1 Mean Velocities

Mean axial velocity profiles in the central X,Y plane for the center three lobes at various downstream locations for L_1 equals to 1.34L and 1.5L are shown in Figure 4.40 and 4.41 respectively. These profiles were plotted with an X-Y recorder with the output of the averaged, linearized single normal wire connected to the Y axis while the position of the probe was displayed on the X axis. The integration time on the digital voltameter was held at one second for both cases. For L_1 less than 1.5L, low frequency disturbances (characteristic time greater than 1 sec) were present, and mean axial velocity profiles in the X,Y plane were found to be asymmetrical about their axes. Profiles typical of such a situation at L_1 equal to 1.34L are shown in Figure 4.40. Even at large downstream distances, for example, at X equal to 80D, low frequency disturbances were observed. Similar observations were also made by Corrisin (1944) in an investigation of the behavior of parallel two-dimensional air jets. In his case asymmetry of the profiles was

more pronounced than in the present case, and can be attributed to his jets being unventilated.

For L_1 greater than or equal to 1.5L fewer low frequencies were present, and the profiles looked very similar to those of a multiple free jet with some secondary flow induced between the jets. Profiles typical of such a situation at L_1 equal to 1.5L are shown in Figure 4.41. As before, top-hat profiles with equal magnitudes are found at the exit plane. At X equal to 5D, a noticeable amount of secondary flow is induced between the jets in contrast to a free jet configuration. The ratio of U_s (secondary flow velocity) to U_o (exit velocity) is about 0.08. Marsters (1977) reports the ratio being 0.125 for two ventilated plane parallel jets at the corresponding spacing and Reynolds number (R_{e_D} = 12,000). A nearly flat profile establishes that complete mixing of the jets has occurred at a location of approximately 60D. The effect of the finite number (5) of jets is indicated by the drop in the magnitude of the velocity at the tips of the profile, which first appears at X equal 60D. This is not noticeable in the free jet configuration. Most of the measurements described hereinafter are for the case of a separation distance of 7.5 cm (1.5L).

The decay of the square of the mean axial velocity with downstream distance for the three cases (single free jet, multiple free jet and confined multiple jet) is shown in Figure 4.42. The decay for the case of the multiple confined jet is almost identical to that of a multiple free jet. Judging from this it seems that the effect of the confining surfaces on the centerline velocity of the jet is minimal. As described in the previous section, the decay of the single jet follows the multiple jet data closely in the first region and most of the second region.

The normalized mean velocity profiles in the X,Y plane for the center jet are shown in Figure 4.43. The secondary flow induced between the jets is seen in the profile at X equal to 10D. Profiles for this case, for X less than 40D, have magnitudes less than those of the single and multiple free jets, when compared at their corresponding locations. For X greater than or equal to 60D, the profiles for the multiple free jet and multiple confined jet are almost identical, and the mean velocity is uniform across the lobes.

The profiles in the central X,Z plane show marked differences when compared with a multiple free jet configuration, and a schematic of this flow field is shown in Figure 4.44. The profiles are plotted to scale. The dotted line in the figure correspond to a pseudopotential core where the jet begins to act like a single jet (see Figure 5.23). The end of this pseudopotential core occurs at X equal to 60D. For X greater than 60D, the mean velocity profiles are almost flat across the jet. This observation along with the previous discussion (regarding profiles in the X,Y plane) suggest that the mean velocity for X greater than 60D is homogeneous.

The normalized mean velocity profiles in the X,Z plane are shown in Figure 4.45. The abscissa Z is normalized with respect to the lobe width D, while as before the mean velocity is normalized with respect to the centerline mean velocity at the corresponding station. The figure also locates the position of the plate. For X less than or equal to 40D, the profiles exhibit a saddle shape. For locations X greater than or equal to 60D, the profiles are more nearly uniform across the jet, and have a local minimum as shown in the figure.

To exhibit the influence of the plates on the flow field, the profiles in the X,Z plane for the two cases of the multiple free jet and the multiple confined jet at a typical location of X equal to 60D are shown in Figure 4.46. The profiles in the center portion of the jet ($Z \lesssim 6D$) are almost identical. The area under the profile of the confined jet is greater than that of a free jet, while the areas in the X,Y plane for both cases are nearly identical at this location ($X = 60D$). This suggests a greater mean flow through the channel than for the case of a multiple free jet.

4.3.2 Turbulent Intensities and Shear Stresses

The rms intensity for the axial component of velocity on the centerline of the jet, along with the results of a multiple free jet are shown in Figure 4.47. The rms intensity is normalized with respect to the mean axial velocity at the exit rather than with the local mean centerline velocity. The results for both cases are almost identical. As discussed in the previous section, for X greater than 40D the magnitudes are less than that of a single free jet.

The normalized rms intensities along the centerline of the jet are shown in Figure 4.48. For X less than 10D, the results are the same as that of the previous two cases, and are therefore not displayed in the figure. The $\tilde{u}$ value reaches a maximum at X equal to 30D instead of 10D as in the two previous cases. For X greater than 60D, it reaches a constant value of about 0.12. The quantities $\tilde{v}$ and $\tilde{w}$ have a behavior similar to that of $\tilde{u}$. For X greater than 60D it is found that $\tilde{v} \simeq 0.88\ \tilde{u}$, $\tilde{w} \simeq 0.83\ \tilde{u}$ which suggest a near isotropic behavior along the centerline of the jet. The values of the ratios $\tilde{v}/\tilde{u}$ and $\tilde{w}/\tilde{u}$ in the present case are lower than those of a multiple free jet.

The $\tilde{u}$ profiles in the central X,Y plane for different downstream locations are shown in Figure 4.49. For X greater than or equal to 60D, the profiles become flat just as the mean velocity profiles. Profiles for all downstream locations are almost identical to those of the multiple free jet when compared at their corresponding locations. Similar observations are also made from $\tilde{v}$ and $\tilde{w}$ profiles in the X,Y plane, which are shown in Figure 4.50 and 4.51 respectively. The values of the ratios $\tilde{v}/\tilde{u}$ and $\tilde{w}/\tilde{u}$ in the present case are lower than those of a multiple free jet when compared at appropriate locations along the Y axis.

The profiles of $\tilde{u}$ in the central X,Z plane for different downstream locations, are shown in Figure 4.52. The distance along the Z axis is normalized with respect to the width D. Profiles for X less than 20D are almost identical to those of a multiple free jet at corresponding locations. Unlike the previous case, a very mild saddle shape profiles is developed at X equal to 60D, and the profile is nearly uniform. Further flattening occurs for locations of X greater than 60D. This observation along with the corresponding profiles in the X,Y plane suggest that the field of turbulence is quite homogeneous.

The profiles of $\tilde{v}$ and $\tilde{w}$ are also uniform for X greater than 60D as shown in Figures 4.53 and 4.54, respectively, with the values $\tilde{v} \simeq 0.88\ \tilde{u}$ and $\tilde{w} \simeq 0.83\ \tilde{u}$. Judging from these results one can conclude that the flow field in the channel for X greater than 60D is nearly homogeneous and isotropic in structure, and the flow field for the center three jets has characteristics quite similar to that of a flow generated by a grid.

The normalized turbulent shear stress $\widetilde{uv}$ for different downstream locations are plotted in Figure 4.55. The profiles are almost identical

to those of a multiple free jet when compared at corresponding locations. For X greater than 60D, as in the previous case, the normalized stress is quite small. The normalized turbulent shear stress $\widetilde{uw}$ in the X,Y plane is found to be negligible for all downstream stations measured.

The normalized turbulent shear stress $\widetilde{uw}$ in the X,Z plane for various downstream locations are shown in Figure 4.56. The values of uw in the present case are lower than those for the multiple free jet at corresponding locations. The values of uw across the jet for X equal to 100D are very small (of the order of 0.003). Likewise, the magnitudes of $\widetilde{uv}$ in the X,Z plane are found to be very small. These results along with mean velocities and turbulent intensities in both X,Y and X,Z planes suggests that the flow field is nearly homogeneous and isotropic in the channel for X greater than 60D.

V THEORETICAL CONSIDERATIONS

In this chapter an attempt is made to develop an analytical model to predict the mean velocity profiles for the case of a two-dimensional jet at low (incompressible) speeds discharging into still fluid of similar density. The analysis is based on Reichardt's inductive theory which linearizes the equation of motion for the mean square velocity and thus enables the superposition of this parameter for multiple interfering jets. As a result a prediction can be made for the distance downstream of the jet exit at which the flow becomes uniform, that is, where the merging two-dimensional jets lose their individual identities and behave as a single jet.

5.1 Equations of Motion: the Boundary Layer Approximation

A right-handed cartesian coordinate system is chosen with coordinate x pointing along the direction of the mean flow U. The Navier-Stokes equations in the absence of body forces for incompressible flow can be written as

$$\frac{\partial u_I}{\partial x} + \frac{\partial v_I}{\partial y} + \frac{\partial w_I}{\partial z} = 0 \tag{1}$$

$$\frac{\partial u_I}{\partial t} + \frac{\partial u_I^2}{\partial x} + \frac{\partial u_I v_I}{\partial y} + \frac{\partial u_I w_I}{\partial z} = -\frac{1}{\rho}\frac{\partial p_I}{\partial x} + \nu\nabla^2 u_I \tag{2a}$$

$$\frac{\partial u_I}{\partial t} + \frac{\partial v_I u_I}{\partial x} + \frac{\partial v_I^2}{\partial y} + \frac{\partial v_I w_I}{\partial z} = -\frac{1}{\rho}\frac{\partial p_I}{\partial y} + \nu\nabla^2 v_1 \tag{2b}$$

$$\frac{\partial w_I}{\partial t} + \frac{\partial w_I u_I}{\partial x} + \frac{\partial w_I v_I}{\partial y} + \frac{\partial w_I^2}{\partial z} = -\frac{1}{\rho}\frac{\partial p_I}{\partial z} + \nu\nabla^2 w_I \tag{2c}$$

where u_I, v_I and w_I are instantaneous velocities and ∇^2 denotes laplace's operator.

By introducing each variable as the sum of a mean value and the fluctuation from the mean value, i.e., the velocity is U + u where U is the mean velocity (by definition the mean value of the fluctuation is zero), the mean value equations can be written as

$$\frac{\partial U}{\partial x} + \frac{\partial V}{\partial y} + \frac{\partial W}{\partial z} = 0 \tag{3}$$

$$\frac{\partial U^2}{\partial x} + \frac{\partial UV}{\partial y} + \frac{\partial UW}{\partial z} + \frac{\partial \overline{u^2}}{\partial x} + \frac{\partial \overline{uv}}{\partial y} + \frac{\partial \overline{uw}}{\partial z} = - \frac{\partial p}{\partial x} + \nu\nabla^2 U \tag{4a}$$

$$\frac{\partial UV}{\partial x} + \frac{\partial V^2}{\partial y} + \frac{\partial VW}{\partial t} + \frac{\partial \overline{uv}}{\partial x} + \frac{\partial \overline{v^2}}{\partial y} + \frac{\partial \overline{vw}}{\partial z} = - \frac{\partial p}{\partial y} + \nu\nabla^2 V \tag{4b}$$

$$\frac{\partial UW}{\partial x} + \frac{\partial VW}{\partial y} + \frac{\partial W^2}{\partial z} + \frac{\partial \overline{uw}}{\partial x} + \frac{\partial \overline{vw}}{\partial y} + \frac{\partial \overline{w^2}}{\partial z} = - \frac{\partial p}{\partial z} + \nu\nabla^2 W \tag{4c}$$

For many turbulent flows, the mean value equations may be simplified by using a boundary layer approximation similar to that introduced by Prandtl for laminar boundary layer flow at large Reynolds numbers. However, separate justification for turbulent flows is needed (see Townsend, 1976, Chapter 6). Using this approximation, for a jet issuing into still fluid, equations (4a), (4b), and (4c) reduce to a single equation

$$\frac{\partial U^2}{\partial x} + \frac{\partial UV}{\partial y} + \frac{\partial UW}{\partial z} + \frac{\partial (\overline{u^2} - \overline{v^2})}{\partial x} + \frac{\partial \overline{uv}}{\partial y} + \frac{\partial \overline{uw}}{\partial z} = 0 \tag{5}$$

where the term $\partial(\overline{u^2} - \overline{v^2})/\partial x$ is usually small. Equation (5) is valid for any three-dimensional jet.

It is difficult to solve the above equations analytically for a three-dimensional flow. However, the flow field close to the jet exit can be approximated by a two-dimensional flow. For this case equations (3) and (5) can be simplified further. The following analysis is based on the above assumption.

5.2 The Plane Turbulent Free Jet

Let us consider a jet of air coming from a plane nozzle into a large expanse of air. Let the width of the jet be D and let U_o be the uniform velocity at the exit plane of the jet. Figure 5.1 shows a schematic representation of the configuration discussed above. Experimental observations on the mean turbulent velocity field indicates that in the axial direction of the jet, one could divide the flow into two distinct regions. In the first region, close to the nozzle, known commonly as the initial region, there is a wedge-like region of constant mean velocity, equal to U_o. This wedge is known as the potential core and is surrounded by a mixing layer on top and bottom.

In the second region, known as the fully developed flow region, the transverse distribution of the mean velocity in the x-direction, i.e., the variation of U with y at different sections has the same geometrical shape. Let us now try to compare the distributions at different sections in a dimensionless form. At each section, let us make the velocity U dimensionless by dividing it by U_c at that section and let b represent a typical length for that section. Let us take b as the value of y where U is equal to half the maximum velocity. In these non-dimensionless coordinates (i.e., U/U_c vs y/b) one finds (see for example Gutmark and Wygnanski, 1976, and Figure 4.3) that the velocity

distributions at different sections fall on common curve. This property is called the self-similarity. In order to use these similarity profiles for predicting the mean velocity field, we have to be able to predict the manner of variation of the velocity (U_c) and length (b) scales.

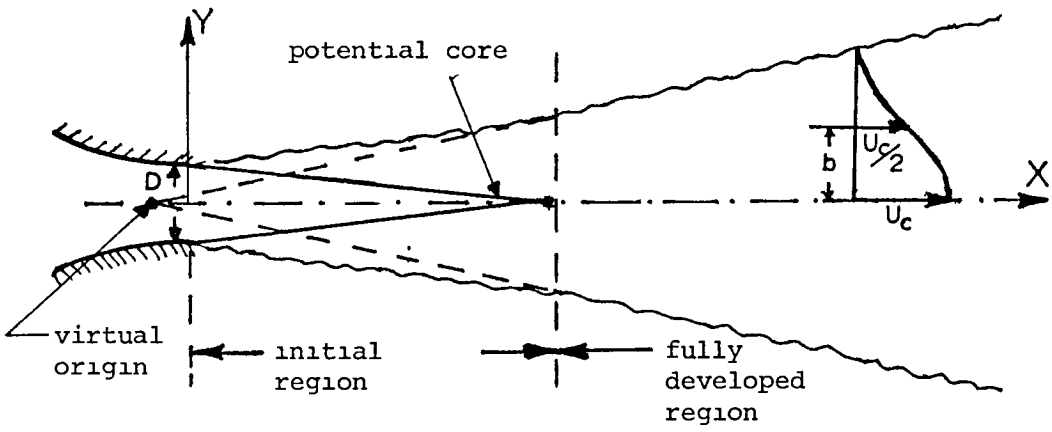

Figure 5.1 Schematic Representation of a Plane Turbulent Jet

5.2.1 Initial Region

Let us consider a half plane jet as shown in Figure 5.2. The thickness of the shear layer at any x could be denoted as $\overline{b}$. If one observes the growth of the shear layer, it will be found that $\overline{b}$ increases continuously with x. In Figure 5.2, OA and OB denote approximately the edges of this shear layer. If we look at the velocity distributions at different x-stations (see for example Liepmann and Laufer, 1947), they appear to have the same shape but are not symmetrical with respect to the x-axis.

For testing possible similarity of these velocity profiles at different sections, let us measure transverse distance downwards from the point where $U = U_o$ and let us denote it as y and let b denote the value of y where $U/U_o = 0.5$. If we plot U/U_o against y/b for various sections, they all fall on a single curve (see Liepmann and Laufer, 1947), thereby showing that the velocity distribution is indeed similar. We will use these basic observations to develop a relation for the growth of the mixing region and we will also predict the mean velocity distribution based on suitable shear stress model. In the following, we will use the theory developed by Reichardt (1944) which linearizes the equation of motion for the mean square velocity.

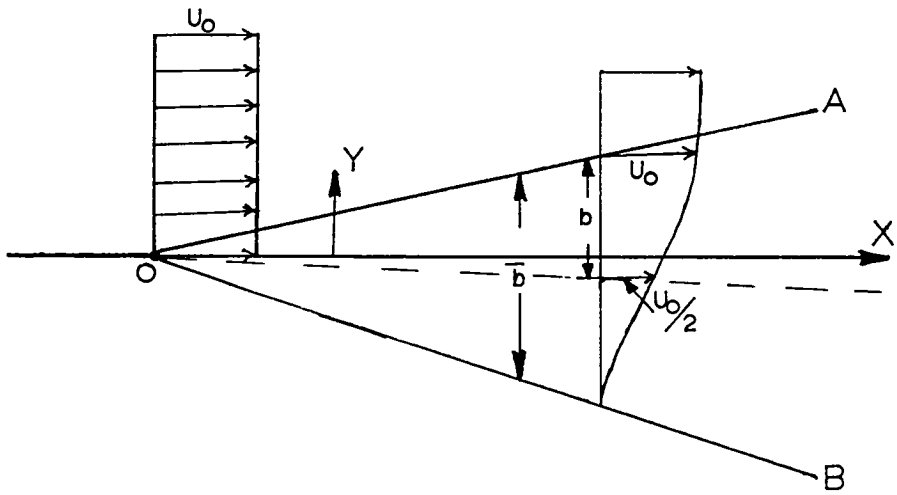

Figure 5.2 Schematic of a Plane Turbulent Shear Layer

From the equation of motion for the plane shear layer we have (from equation (5))

$$\frac{\partial U^2}{\partial x} + \frac{\partial \overline{u_I v_I}}{\partial y} = 0 \qquad (6)$$

where $\overline{u_I v_I} = UV + \overline{uv}$.

We assume that the mean square velocity profiles are self-similar, but not those of mean velocity as was assumed in the theories of Tollmien and Göetler (see Chapter 5 of Rejaratnam, 1976). Letting

$$U^2 = U_o^2 f(\xi)$$

$$\xi = y/b \quad , \tag{7}$$

where b is the characteristic width of the shear layer which varies with x.

Reichardt also assumes the following empirical relation which states that the flux of the x-component of momentum, which is transferred in the transverse direction, is proportional to the transverse gradient of momentum. That is

$$\overline{u_I v_I} = \Lambda(x) \frac{\partial \overline{u_I^2}}{\partial y}$$

$$(u_I^2 = U^2 + \overline{u^2}) \tag{8}$$

where $\Lambda(x)$ is an arbitrary function of x.

In eliminating $\overline{u_I v_I}$ from equations (7) and (8) and utilizing the fact that $\overline{u^2}/U^2$ is small (4-5 percent), we obtain Reichardt's fundamental equation

$$\frac{\partial U^2}{\partial x} = \Lambda(x) \frac{\partial^2 U^2}{\partial y^2} \tag{9}$$

Substituting equation (7) into equation (9), we obtain

$$-\xi f'(\xi) = \Lambda(x) f''(\xi) \frac{1}{b} \frac{dx}{db} \quad .$$

The mean square velocity profiles will become similar if we assume

$$\Lambda(x) = \text{const}\ \ b\,\frac{db}{dx} \quad ,$$

and on further taking the constant to be $\frac{1}{2}$ we get

$$\Lambda(x) = \frac{b}{2}\,\frac{db}{dx} \quad . \tag{10}$$

To obtain the variation of the length scale b with x, Reichardt uses the idea that because the dimensionless velocity profiles are self-similar, the ratio of the product of the component velocities $\overline{u_I v_I}$ to the square of the characteristic velocity U_c^2 at a given cross section can depend only on the dimensionless ordinate ξ

$$\frac{\overline{u_I v_I}}{U_c^2} = g(\xi) \tag{11}$$

but not on the absolute distance x.

Using equations (8), (10) and (11) we find the quantity

$$\frac{db}{dx}\ \frac{d(U^2/U_c^2)}{d(\xi)} = g(\xi)$$

depends only on ξ.

From this it follows further that

$$\frac{db}{dx} = \text{constant} = c \quad .$$

whence b = cx, and consequently

$$\Lambda = \frac{c^2}{2}\,x \quad , \tag{12}$$

where the constant c is taken from the experimental data and is equal to 0.109.

Substituting equation (12) in equation (8) we obtain

$$\overline{u_I v_I} = \frac{c^2}{2} \times \frac{\partial U^2}{\partial y^2} \qquad (13)$$

$$\left(\frac{\overline{u^2}}{U^2} << 1 \right)$$

Equation (9) can be rearranged, with the aid of equation (12), to give

$$\frac{\partial U^2}{\partial x} = \frac{c^2}{2} \times \frac{\partial U^2}{\partial y^2} \qquad (14)$$

Substitution $c^2x^2 = 4X$ gives

$$\frac{\partial U^2}{\partial X} = \frac{\partial^2 U^2}{\partial y^2}$$

which is the two-dimensional diffusion equation where X is always positive and replaces the time variable.

A solution of equation (14) for the shear layer is

$$U^2 = -\frac{1}{2} U_o^2 \operatorname{erf}\left(\frac{y}{b} \right) + \frac{1}{2} U_o^2$$

or

$$U^2 = \frac{1}{2} U_o^2 \operatorname{erfc}(y/b) \qquad (15)$$

which satisfied the boundary conditions.

$$U^2 \to 0 \quad \text{as} \quad y \to \infty$$

$$U^2 \to U_o^2 \quad \text{as} \quad y \to -\infty$$

This is a known solution for a free turbulent shear layer and has been verified by experiments (see Reichardt, 1944).

We will now consider the initial region of the plane turbulent jet, which consists of two plane shear layers as shown in Figure 5.3.

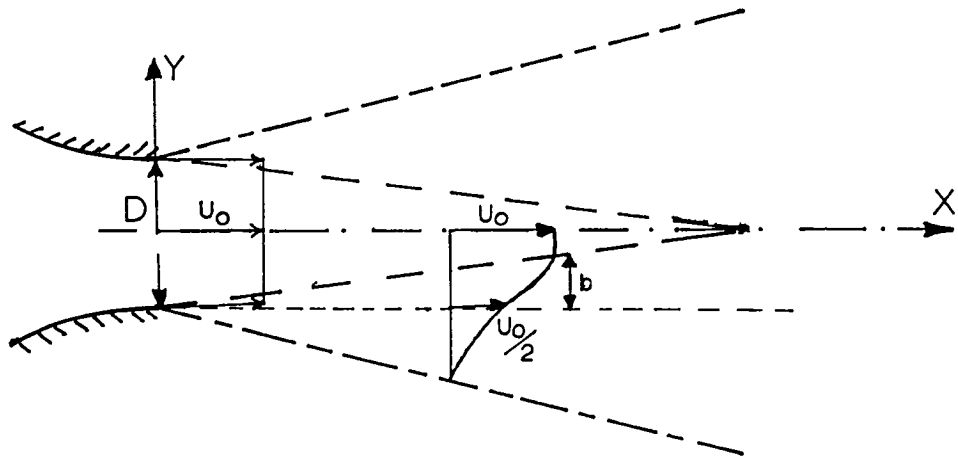

Figure 5.3 Schematic of Initial Region of a Plane Jet

Equation (14) is a linear partial differential equation for which the solution for the shear layer is given by equation (15). Because the sum of individual solutions of a linear differential equation is by definition itself a solution, this important result allows extension of the theory to the initial region. A solution of equation (14) for the initial region of a two-dimensional jet of width D at the exit plane can be written as

$$U^2 = \frac{U_o^2}{2}\left[\text{erf}\left(\frac{y + \frac{D}{2}}{b}\right) - \text{erf}\left(\frac{y - \frac{D}{2}}{b}\right)\right] \tag{16}$$

which satisfies the boundary conditions.

$$U^2 \to 0 \quad \text{as} \quad y \to \infty$$

$$U^2 \to 0 \quad \text{as} \quad y \to -\infty$$

$$U^2 = U_o^2 \quad \text{at} \quad y = 0 \text{ and } b << \frac{D}{2} \quad .$$

5.2.2 Fully Developed Region

Far downstream of the jet exit where b >> D/2, equation (15) can be rearranged as

$$U^2 = \frac{U_o^2}{2} \frac{D}{b} \frac{2}{\sqrt{\pi}} e^{-(y/b)^2}$$

$$= \frac{U_o^2}{2} \frac{D}{b} e^{-(y/b)^2} \qquad (17)$$

which is a known solution for a two-dimensional jet as given by Reichardt. Solutions similar to equation (16) can also be derived from other theories such as the ones developed by Tollmin and Göetler (see Rejaratnam, 1976). The empirical law of momentum given by Reichardt's theory (equation 14) has been used in correlating the present data and the results are plotted in Figure 5.4. Because of the assumptions used, the law holds only in the two-dimensional type region, thus the results of only region II are presented. The normalized instantaneous shear stress $\overline{u_I v_I}$ is represented by the dark symbols in the figure, while the right-hand side of the equality in equation (14) is represented by open symbols. The measurements confirm the equation fairly well as shown in the figure, thus indicating the correctness of this empirical law.

5.3 Multiple Jet Solution

The arrangements of the multiple two-dimensional jets are shown in Figure 5.5. The individual jets are arranged in a line with an equal spacing, denoted by S, between them. The exit velocity of each lobe is constant and is equal to U_o. The origin of the coordinate system is taken to be at the center of the center lobe, with the other lobes extending symmetrically in both directions along the y axis. We will once again use equation (6) along with the proper assumptions discussed in the previous section. Invoking once again the superposition principle the above analysis allows extension of the theory to a jet emanating from a series of two-dimensional lobes.

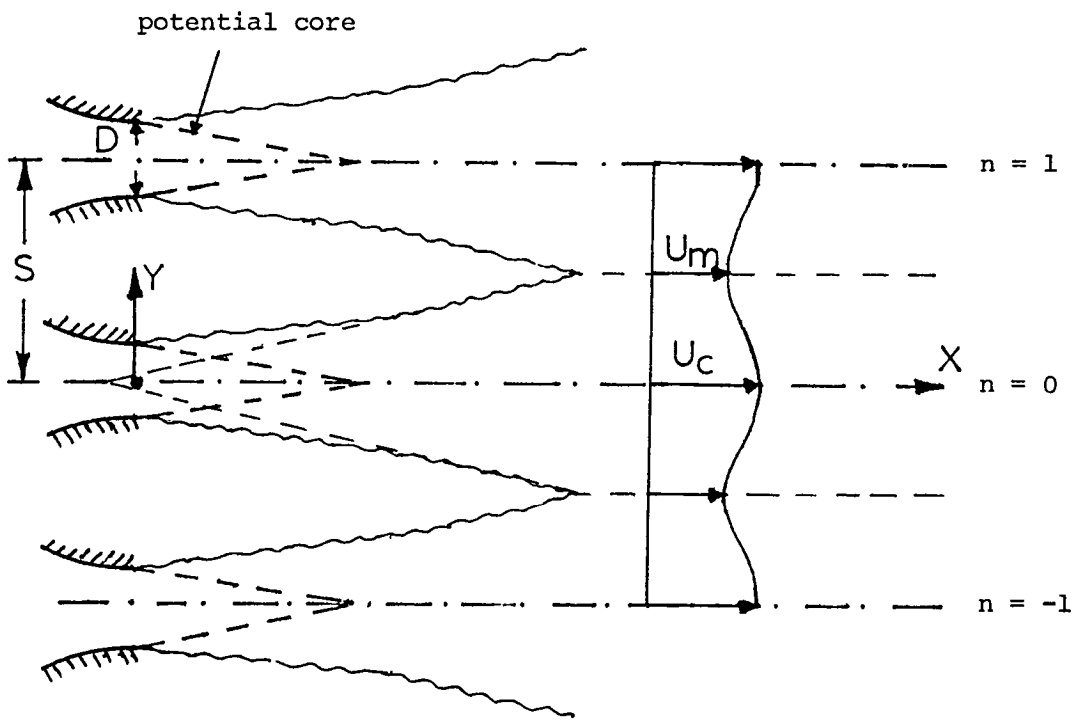

Figure 5.5 Schematic of Multiple Plane Jets

The square of the mean velocity for the case of multiple jets can therefore be written as follows.

$$\frac{U^2}{U_o^2} = \frac{1}{2}\sum_{n=-N}^{N}\left[\operatorname{erf}\left(\frac{y + ns}{cX} + \frac{D}{2cX}\right) - \operatorname{erf}\left(\frac{y + ns}{cX} - \frac{D}{2cX}\right)\right] \tag{18}$$

On the center plane y = 0, we have

$$\frac{U_c^2}{U_o^2} = \frac{1}{2}\sum_{n=-N}^{N}\left[\operatorname{erf}\left(\frac{ns + \frac{D}{2}}{cX}\right) - \operatorname{erf}\left(\frac{ns - \frac{D}{2}}{cX}\right)\right] \tag{19}$$

and midway between the jets (y = S/2) equation (19) reduces to

$$\frac{U_m^2}{U_o^2} = \frac{1}{2}\sum_{n=-N}^{N}\left[\operatorname{erf}\left(\frac{(2n + 1)S + D}{2cX}\right) - \operatorname{erf}\left(\frac{(2n + 1)S - D}{2cX}\right)\right] \tag{20}$$

The profiles of (U_c^2/U_m^2) in the x,y plane for the center jet from y = 0 to y = 4D along with the experimental results are shown in Figure 5.6. The agreement between the data and the analytical model is satisfactory as shown in the figure.

Defining the velocity defect E

$$E = \frac{U_c^2 - U_m^2}{U_c^2} \quad ,$$

Equation (20) can be written as follows.

$$E = \sum_{n=-N}^{N} \left[\operatorname{erf}\left(\frac{ns + \frac{D}{2}}{cX}\right) - \operatorname{erf}\left(\frac{ns - \frac{D}{2}}{cX}\right)\right] - \left[\operatorname{erf}\left(\frac{(2n+1)S + D}{2cX}\right) - \operatorname{erf}\left(\frac{(2n+1)S - D}{2cX}\right)\right] \Bigg/ \left[\operatorname{erf}\left(\frac{ns + \frac{D}{2}}{cX}\right) - \operatorname{erf}\left(\frac{ns - \frac{D}{2}}{cX}\right)\right] \tag{21}$$

The downstream distance at which the individual jets begin to merge can be defined as the point where the value of E deviates from unity for a given amount. Beyond this the flow becomes effectively uniform. The velocity defect E is plotted with the downstream distance in Figure 5.7 and compared with the present experimental results. The agreement between the data and the model seem to be in satisfactory agreement.

VI CONCLUSIONS

In this chapter a brief summary of the results are reviewed along with some recommendations for future work. In the case of a single rectangular jet, the flow is characterized by the presence of three distinct regions when the decay of the square of the axial mean velocity along the centerline of the jet is used to describe the flow field. These regions are: the potential core region, a two-dimensional type region and an axisymmetric type region. The onset of the second region appears to be at a location where the shear layers from the short dimension of the nozzle meet. Correspondingly, the centerline velocity decay first assumes the axisymmetric character at a location where the two shear layers from the long dimension of the nozzle meet.

For a rectangular jet of aspect ratio of 16.7 with the laminar top-hat profile at the exit, the following conclusions are drawn: The three regions noted above are the potential core region, which ends at approximately 4D, the two-dimensional type region extending up to 60D, and the axisymmetric jet type region extending beyond 60D.

The profiles of U, V and $\widetilde{uv}$ in the central X,Y plane, for X greater than or equal to 30D are found to be geometrically similar. The profiles of $\tilde{u}$, $\tilde{v}$ and $\tilde{w}$ are found similar in region II but not in region III. For X less than 60D in the central X,Z plane, the profiles of U exhibit a saddle shape, while the profiles in region III approach a similarity profile of an axisymmetric jet. For X less than 40D, the profiles of W exhibit strong negative values along the Z axis. The

profiles of $\tilde{u}$, $\tilde{v}$, $\tilde{w}$ and $\widetilde{uw}$, in the central X,Z plane, do not exhibit similarity for the downstream stations measured.

For the case of a ventilated array of rectangular jets having a spacing of 8D the following observations are made. Because the individual jets act quite independently of each other near the nozzle exit, the point at which the individual jets begin to merge can be estimated from data on the growth rate of a single jet. Far downstream the flow field appears as if it is emerging from a single two-dimensional slot with the width of the slot being the long dimenison of a single lobe. The mutual interaction between the jets results in a lower turbulence level when compared to a single jet at corresponding locations.

For the case of the confined multiple jet with a separation distance between the plates of 1.5L, the following observations are made. The flow field in the central X,Y plane (plane of the array) was little effected by the presence of the plates and the mean velocity profiles look very much similar to that of the multiple free jet at corresponding locations. For X greater than 60D, the mean velocity profiles are uniform across the lobes (in the X,Y plane) as in the previous case, and in addition, the profiles are uniform across the jet in the X,Z plane. The field of turbulence for X greater than 60D was found to be uniform and isotropic in structure. From these observations one may conclude that the flow field, for the configuration under study, and for X greater than 60D, is nearly homogeneous and isotropic.

Systematic and detailed basic studies, as mentioned before, are still needed to understand clearly the physical features of the complex flow fields involved in free and confined multiple jets. The dependence

of the flows on Reynolds number, Mach number, initial velocity profiles and disturbance characteristics should be explored for given geometrical parameters of the problem. Changes brought about by variation of these parameters need to be examined. The range of experimental conditions corresponding, as far as possible, to those of practical interest should be looked into. It is important to investigate the effects of an external free stream (or equivalently those of flight) on these flows.

For given geometrical and initial flow configurations, detailed measurements and where applicable flow visualization of the mean, periodic, and random structure of the flow field (velocity and pressure fields) should be investigated. These include not only spatial and temporal variations, but also, where appropriate, spectral and correlation characteristics, and pressures (mean and fluctuating) on surfaces involved (such as the confining walls in case of confined multiple jets) are to be determined.

Concurrent with experimental investigations and utilizing their results, theoretical studies should be pursued so as to evolve some suitable analytical relations to predict the flows of interest. Such studies, although of necessity will involve initially gross features of the flow, need to address gradually the more detailed problems of turbulence structure of the flows.

REFERENCES

Aiken, N. T., "Advanced Augmentor Wing Research," NASA TMX-62250, October 1972.

Aiken, N. T., "Aerodynamic and Noise Measurements on a Quasi-Two-Dimensional Augmentor Wing Model with Lobe Type Nozzles," NASA TMX-62237, September 1973.

Bevilaqua, P. M., "Evaluation of Hypermixing for Thrust Augmenting Ejectors," Journal of Aircraft, Vol. 11, No. 6, June 1974, pp. 368-354.

Bhat, V. W., "Acoustic Characteristics of Two Parallel Flow Jets," AIAA Paper No. 77-1290, 1977.

Borchers, V. I., and Goethert, H. B., "An Experimental Study of the Noise Radiation of Interfering Jets," AIAA Paper No. 77-1285, 1977.

Bradbury, L.J.S., "The Structure of a Self-Preserving Turbulent Plane Jet," Journal of Fluid Mechanics, Vol. 23, 1965, pp. 31-64.

Bradshaw, P., "The Effect of Initial Conditions on the Development of a Free Shear Layer," Journal of Fluid Mechanics, Vol. 26, Part 2, 1966, pp. 225-236.

Bradshaw, P., "Effects of External Disturbances on the Spreading Rate of a Plane Turbulent Jet," Journal of Fluid Mechanics, Vol. 80, Part 4, 1977, pp. 795-797.

Brown, G. L., and Roshko, A., "On Density Effects and Large Structure in Turbulent Mixing Layers," Journal of Fluid Mechanics, Vol. 64, 1974.

Chandrasuda, C., Mehta, D. R., Weir, D. A., and Bradshaw, P., "Effects of Free Stream Turbulence on Large Structure in Turbulent Mixing Layers," Journal of Fluid Mechanics, Vol. 85, Part 4, 1978, pp. 693-704.

Cook, M. A., and Aiken, N. T., "Low Speed Aerodynamics Characteristics of a Large Scale STOL Transport Model with an Augmented Jet Flap," NASA TMX-62017, March 1971.

Corrisin, S., "Investigation of the Behavior of Parallel Two-Dimensional Air Jets," NACA W-90, 1944.

Dejoode, D. A., and Patankar, V. S., "Prediction of Three-Dimensional Turbulent Mixing in an Ejector," AIAA Paper No. 77-706, 1977.

Duplessis, P. M., Want, L. R., and Kahawita, R., "Investigation of the Near Region of a Square Jet," Journal of Fluids Engineering, Vol. 96, Series I, No. 3, 1974, pp. 246-251.

Everett, W. K., and Robins, G. A., "The Development and Structure of Plane Jets," Journal of Fluid Mechanics, Vol. 88, Part 3, pp. 563-584.

Falarski, D. M., Aiken, N. T., Aoyagi, K., and Koenig, G. D., "Comparison of the Acoustic Characteristics of Large Scale Models of Several Propulsive Lift Concepts," Journal of Aircraft, Vol. 12, No. 7, 1975.

Falarski, D. M., Wilby, F. J., and Aiken, N. T., "Augmentor Wing Propulsive Lift Concept Acoustic Characteristics," Journal of Aircraft, Vol. 13, No. 12, 1976.

Fancher, M., Krothapalli, A., Baganoff, D., "Progress Reports of Joint Institute of Aeronautics and Acoustics," 1976, 1977.

Fiedler, H., Structure and Mechanisms of Turbulence, Parts I and II, Vol. 75, Springer-Verlag, 1977.

Foss, F. J., and Jones, B. J., "Secondary Flow Effects in a Bounded Rectangular Jet," ASME Paper 68-FE-17, 1968.

Gutmark, E., and Wygnanski, I., "The Planar Turbulent Jet," Journal of Fluid Mechanics, Vol. 73, Part 3, 1976, pp. 465-495.

Hill, G. P., "Turbulent Jets in Ducted Streams," Journal of Fluid Mechanics, Vol. 22, Part 1, 1965, pp. 161-186.

Hill, G. W., Jenkins, C. J., and Gilbert, B. L., "Effects of Initial Boundary Layer State on Turbulent Mixing," AIAA Journal, Vol. 14, No. 11, 1976, pp. 1513-1514.

Hill, G. W., Jenkins, C. J., Gilbert, B. L., "Effects of Initial Boundary Layer Conditions on Jet Mixing," Gruman Aerospace Corporation RE-508, September 1975.

Hinze, J. O., Turbulence, Second Edition, McGraw Hill, New York, 1976.

Knystautas, R., "The Turbulent Jet from a Series of Holes in Line," The Aeronautical Quarterly, Vol. XV, February 1964.

Kotsovinos, E. N., "A Note on the Spreading Rate and Virtual Origin of a Plane Turbulent Jet," Journal of Fluid Mechanics, Vol. 77, Part 2, 1976, pp. 305-311.

Laurence, C. J., and Bennighoff, M. J., "Turbulence Measurements in Multiple Interfering Air Jets," NASA TN 4029, 1957.

Laurence, C. J., "Turbulence Studies of a Rectangular Slotted Noise Suppressor Nozzle," NASA TN D-296, 1960.

Liepmann, W. H., and Laufer, J., "Investigation of a Free Turbulent Mixing," NACA TN 1257, 1947.

Marsters, F. G., "Interaction of Two Plane Parallel Jets," AIAA Journal, Vol. 15, December 1977, pp. 1756-1762.

Marsters, F. G., "Measurements in the Flow Field of a Linear Array of Rectangular Nozzles," AIAA Paper No. 79-0350, 1979.

Marsters, F. G., Private Communication, 1979.

McGuirk, J. J., and Rodi, W., "The Calculation of Three-Dimensional Turbulent Shear Flows," First Symposium on Turbulent Shear Flows, Pennsylvania State University, University Park, Pennsylvania, April 1977.

Miller, R. D., and Cummings, W. E., "Force Momentum Fields in a Dual Jet Flow," Journal of Fluid Mechanics, Vol 7, No. 2, 1960, pp. 237-255.

Pai, I. S., and Hsieh, Y. T., "Linearized Theory of Three-Dimensional Jet Mixing with and Without Walls," Journal of Basic Engineering, March 1970, pp. 93-100.

Quinn, B., "Compact Ejector Thrust Augmentation," Journal of Aircraft, Vol. 10, No. 8, 1973.

Quinn, B., "Ejector Performance at High Temperatures and Pressures," Journal of Aircraft, Vol. 12, No. 12, 1976.

Rajaratnam, N., Turbulent Jets, Elsevier, New York, 1976.

Reichardt, H., "On a New Theory of Turbulence," Journal of Royal Aeronautical Society, Vol. 47, June 1943.

Salter, R. G., "Mass Entrainment by Hypermixing Jets," ARL 75-0132, June 1975.

Sato, H., "The Stability and Transition of a Two-Dimensional Jet," Journal of Fluid Mechanics, Vol. 7, 1960, pp. 53-55.

Schlichting, H., Boundary Layer Theory, McGraw-Hill, New York, 6th Edition, 1968.

Seiler, R. M., and Schum, P. E., "An Analytical and Experimental Investigation of Diffusers for VTOL Thrust Augmenting Ejectors," AIAA Paper No. 78-1509, 1978.

Sfeir, A. A., "The Velocity and Temperature Fields of Rectangular Jets," International Journal of Heat and Mass Transfer, Vol. 19, 1976, pp. 1289-1297.

Sfeir, A., "Investigation of Three-Dimensional Turbulent Rectangular Jets," AIAA Paper No. 78-1185, 1978.

Sforza, M. P., Steiger, H. M., and Trentacoste, N., "Studies on Three-Dimensional Viscous Jets," AIAA Journal, Vol. 4, 1966, pp. 800-806.

Sforza, M. P., "A Quasi-Axisymmetric Approximation for Turbulent Three-Dimensional Jets and Wakes," AIAA Journal, Vol. 7, No. 7, 1969.

Sforza, M. P., Stasi, W., "Heated Three-Dimensional Turbulent Jets," ASME Publication, 77-WA/HT27, 1977.

Tanaka, E., "The Interference of Two-Dimensional Parallel Jets," Bulletin of the JSME, Vol. 13, No. 56, 1970.

Tai, C. T., "Optimization of Axisymmetric Thrust Augmenting Ejectors," AIAA Paper No. 77-707, June 1977.

Tollmien, W., "Calculation of Turbulent Expansion Processes," NACA TM 1085, 1945.

Townsend, A. A., The Structure of Turbulent Shear Flow, Cambridge University Press, 1976.

Trentacoste, N., and Sforza, M. P., "Further Experimental Results for Three-Dimensional Free Jets," AIAA Journal, Vol. 5, No. 2, May 1967.

Trentacoste, N., Sforza, M. P., "Some Remarks on Three-Dimensional Wakes and Jets," AIAA Journal, Vol. 6, No. 12, 1968, pp. 2454-2456.

Van Der Hegge, Zijen, G. B., "Measurements of the Velocity Distribution in a Plane Turbulent Jet of Air," Applied Scientific Research, Vol. 7, Section A, 1958, pp. 256-292.

Weinstein, S. A., Osterle, F. J., and Forstall, W., "Momentum and Diffusion from Slot Jet into a Moving Secondary," Tran. A.S.M.E. Journal of Applied Mechanics, Vol. 23, 1956, pp. 437-443.

Weir, D. A., and Bradshaw, P., "The Interaction of Two Parallel Free Shear Layers," First International Symposium on Turbulent Shear Flows," Pennsylvania State University, University Park, Pennsylvania, April 1977.

Wygnanski, I., "Two-Dimensional Turbulent Jet in a Uniform Parallel Stream," AIAA Journal, Vol. 7, No. 1, 1969.

Wygnanski, I., and Fiedler, H., "Some Measurements in the Self-Preserving Jet," Journal of Fluid Mechanics, Vol. 38, 1969, pp. 517-612.

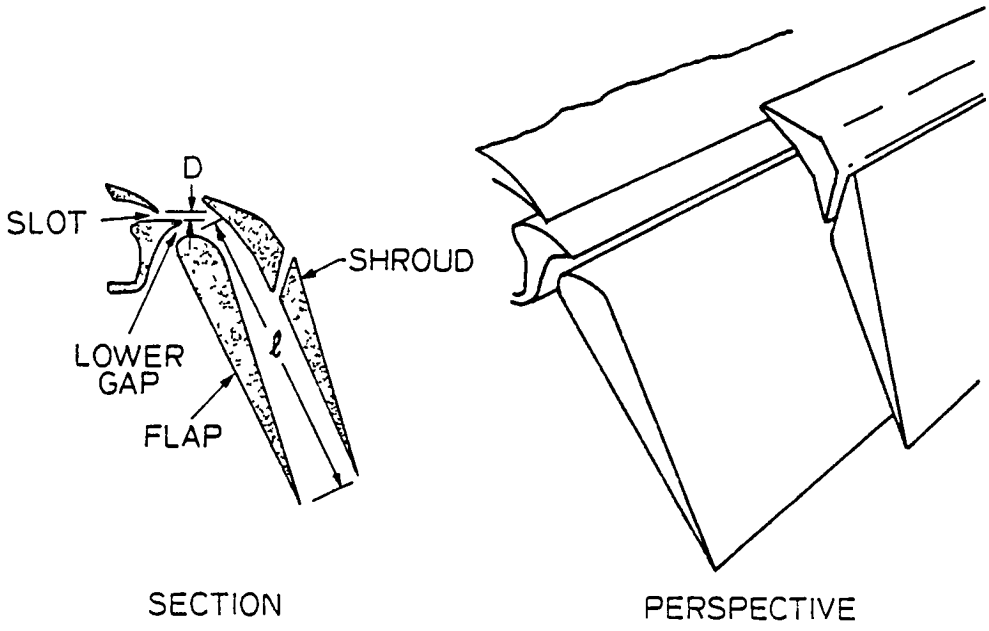

Figure 1.1 Views of slot nozzle augmentor wing

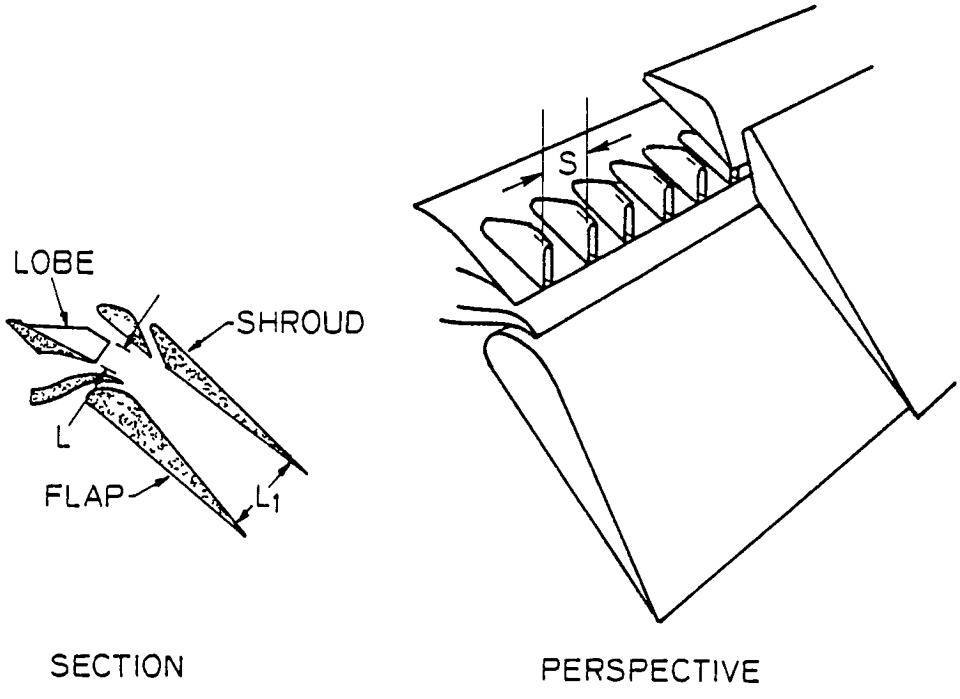

Figure 1.2 Views of lobe nozzle augmentor wing

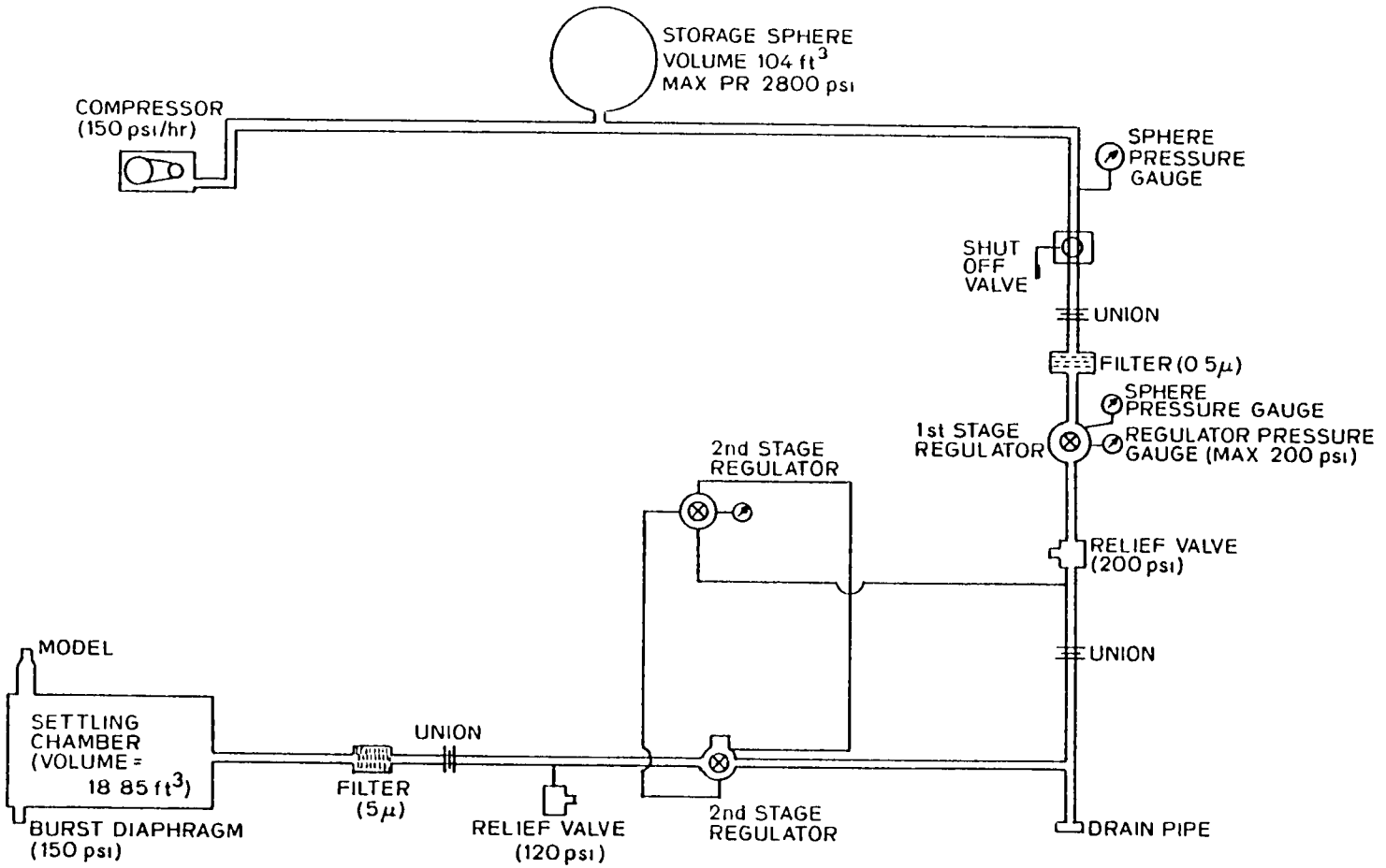

Figure 3.1 A schematic of the air supply system

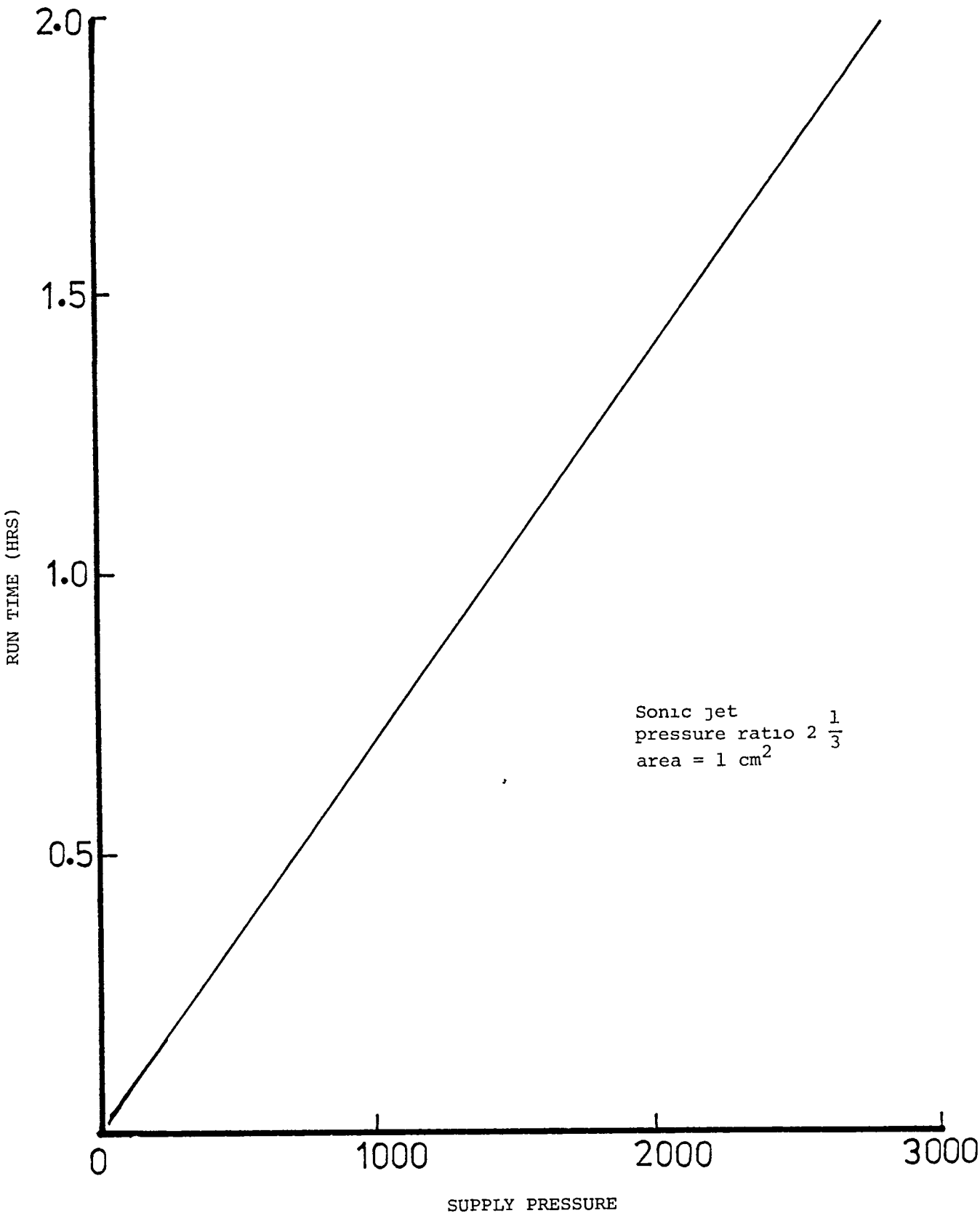

Figure 3.2 Run time for a system supply pressure

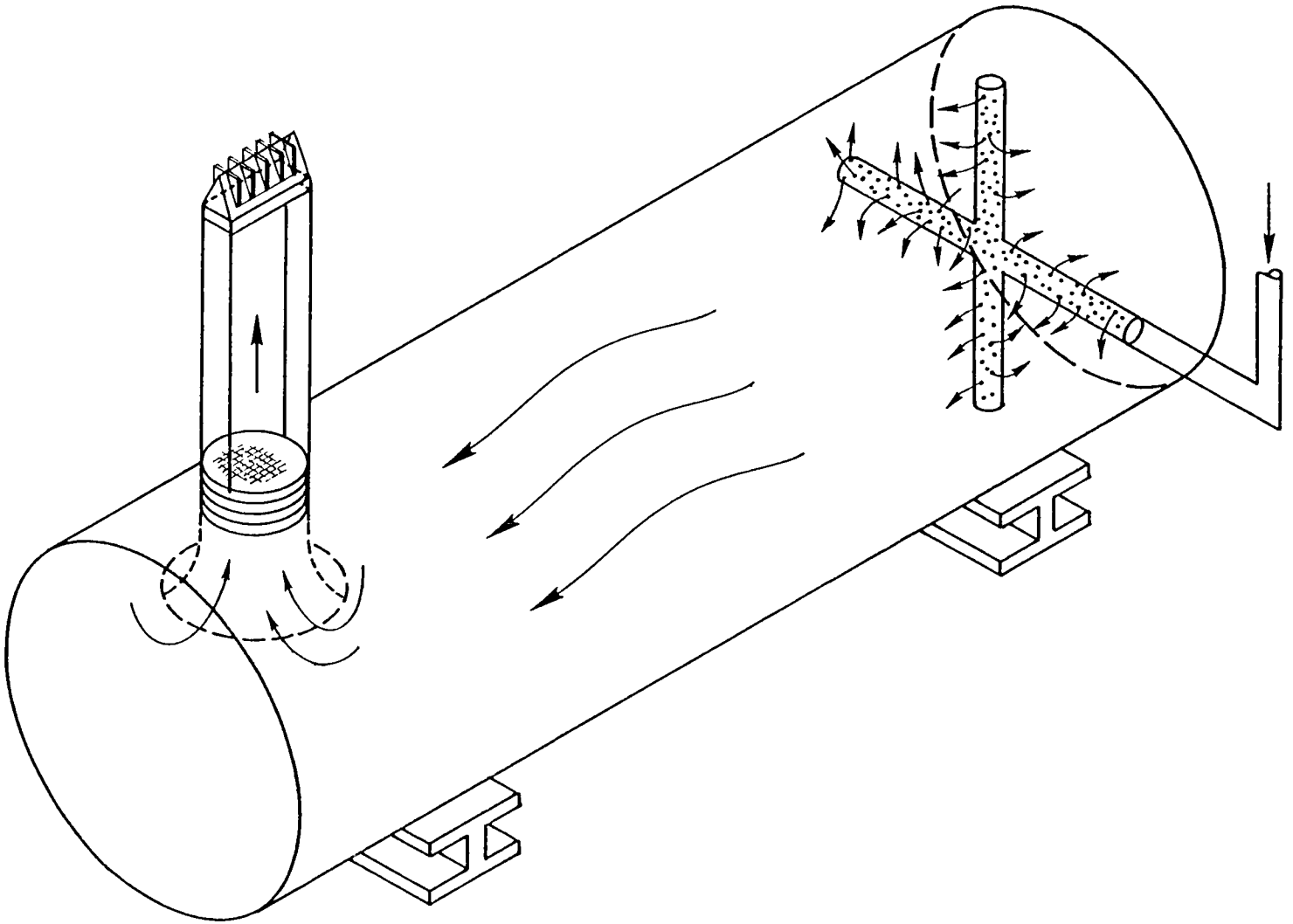

Figure 3.3 A Schematic of the settling chamber

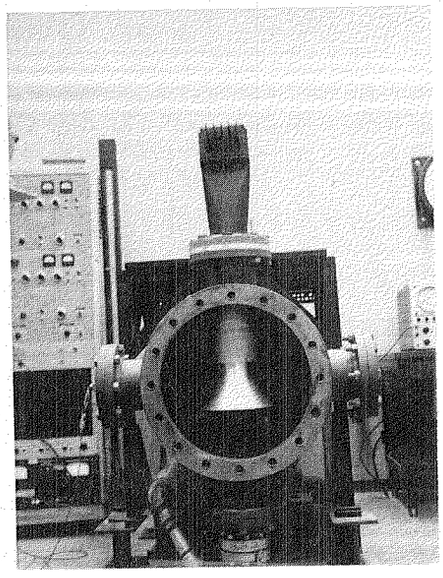

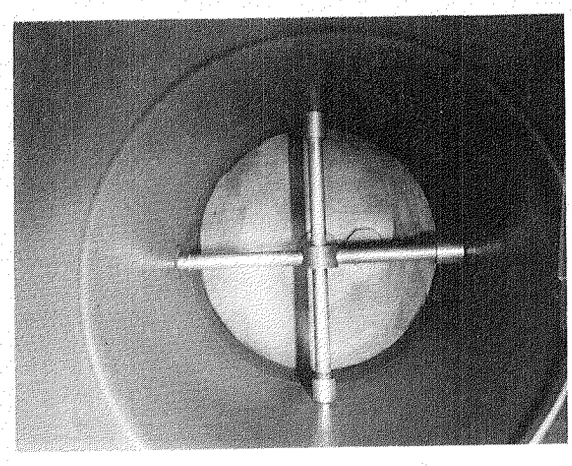

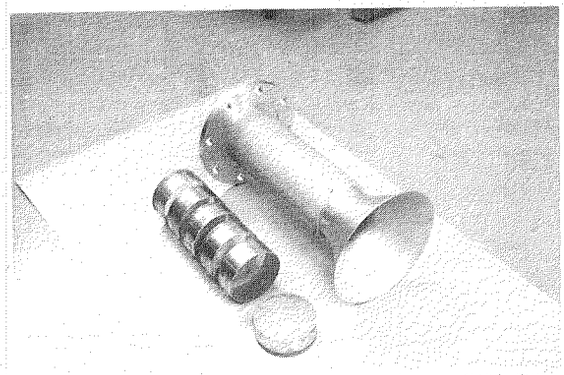

Figure 3.4 Front view of the settling chamber with end plate removed, showing inlet bell, and ames model in place, spray bar at rear of the settling chamber, inlet bell and turbulence screens

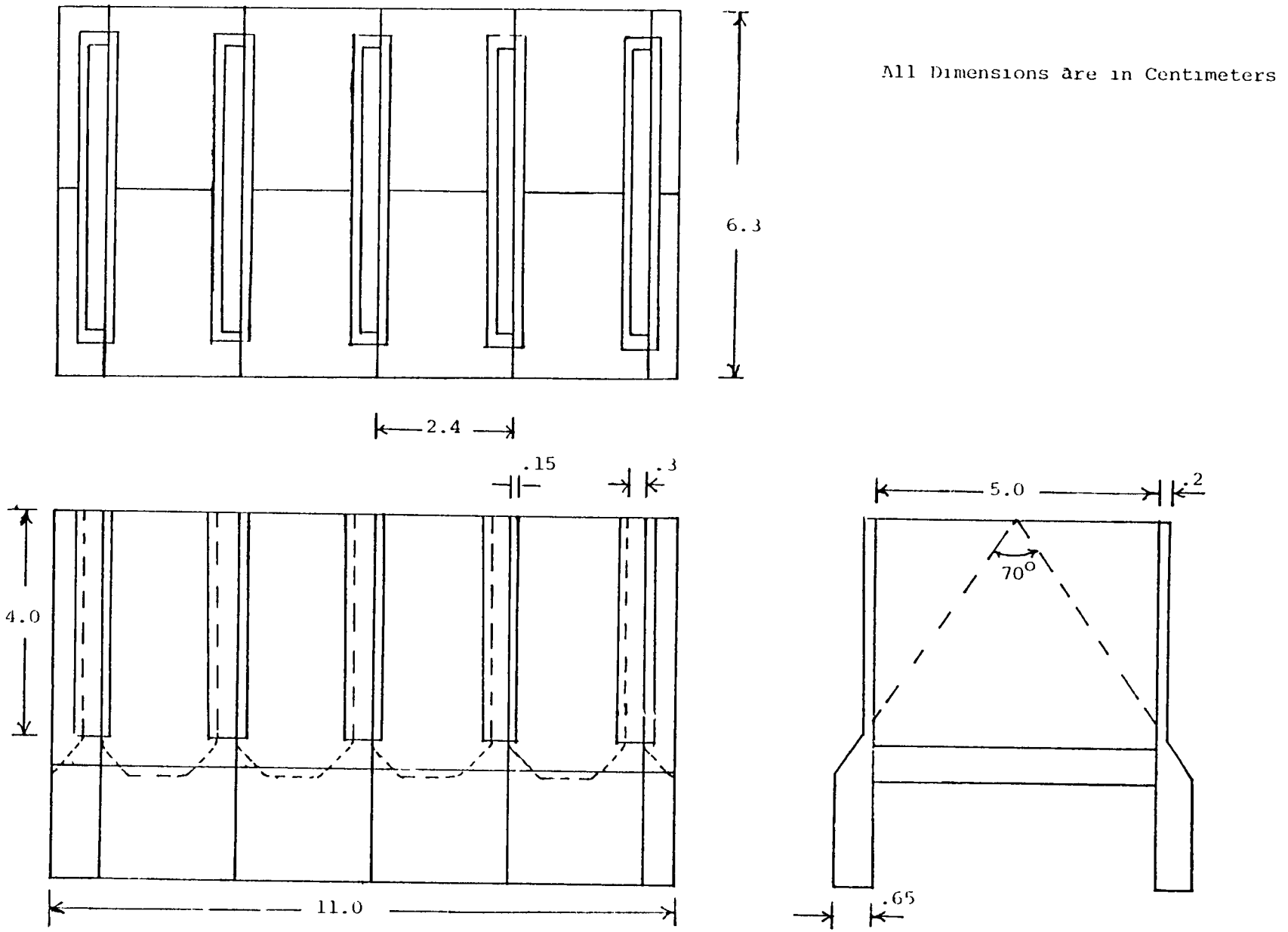

Figure 3.5 Design drawing of the research model

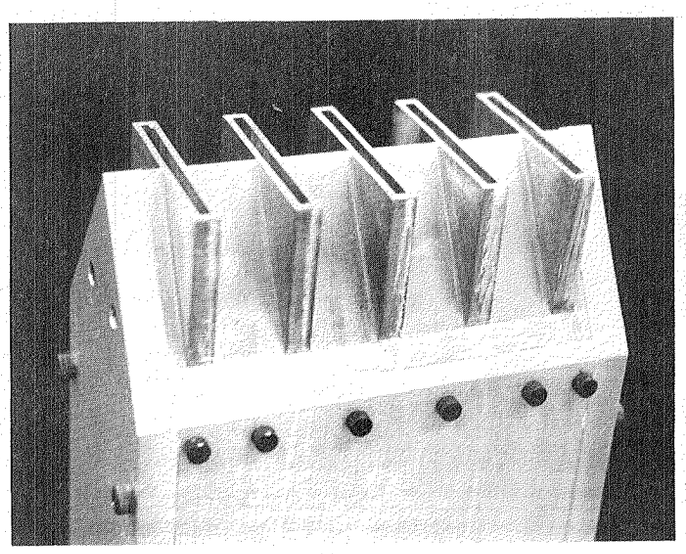

a

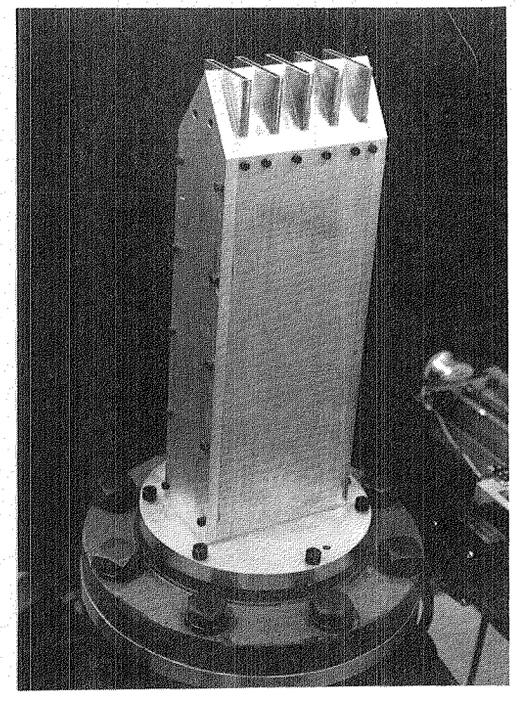

b

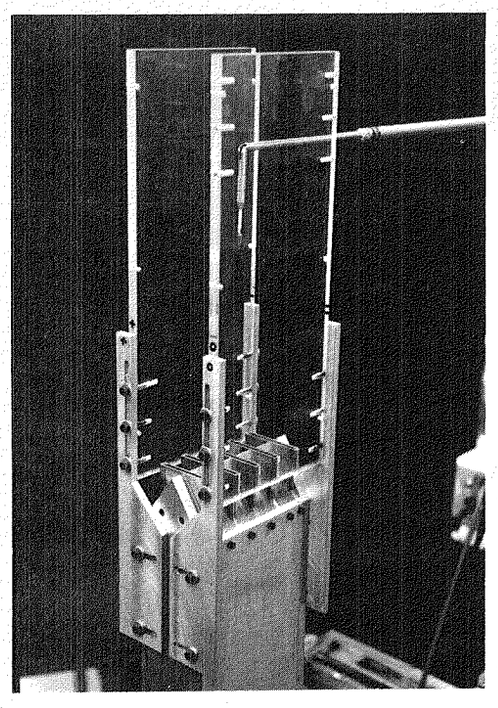

c

Figure 3.6 a) Close view of the model, b) Model with the adapter, c) Model in an ejector configuration

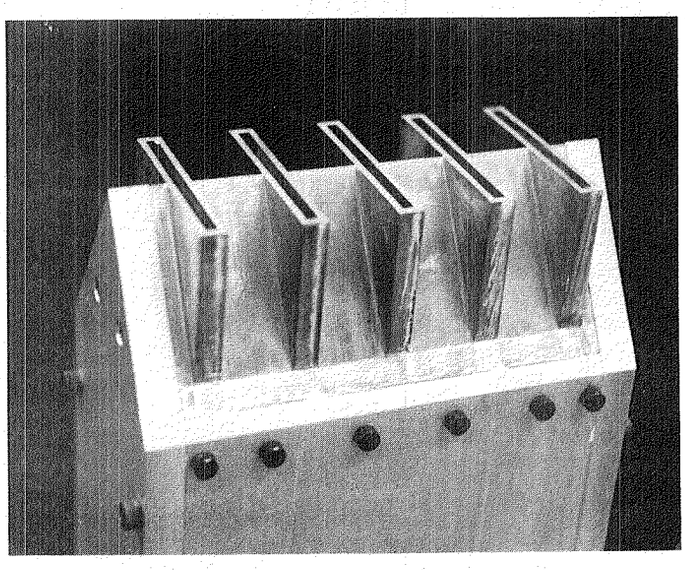

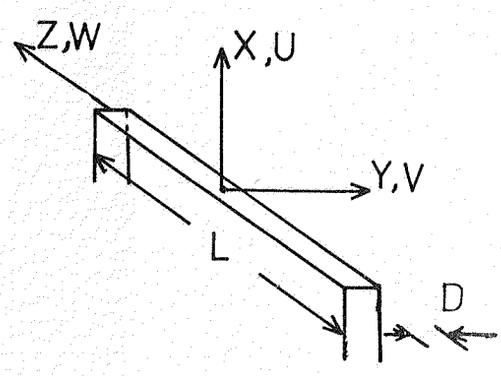

$L = 50\,mm$

$D = 3\,mm$

$AR = 16.7$

$S = 24\,mm$

$U_o = 60\,m/s$

$Re_D = 1.2 \times 10^4$

Exit Conditions: Tophat profile with laminar boundary layers.

$$\frac{\sqrt{\overline{u^2}}}{U_o} = 0.003$$

$$\tau_t = \begin{pmatrix} \overline{u^2} & \overline{uv} & \overline{uw} \\ \overline{uv} & \overline{v^2} & \overline{vw} \\ \overline{uw} & \overline{vw} & \overline{w^2} \end{pmatrix}$$

Figure 3.7 Definition Sketch

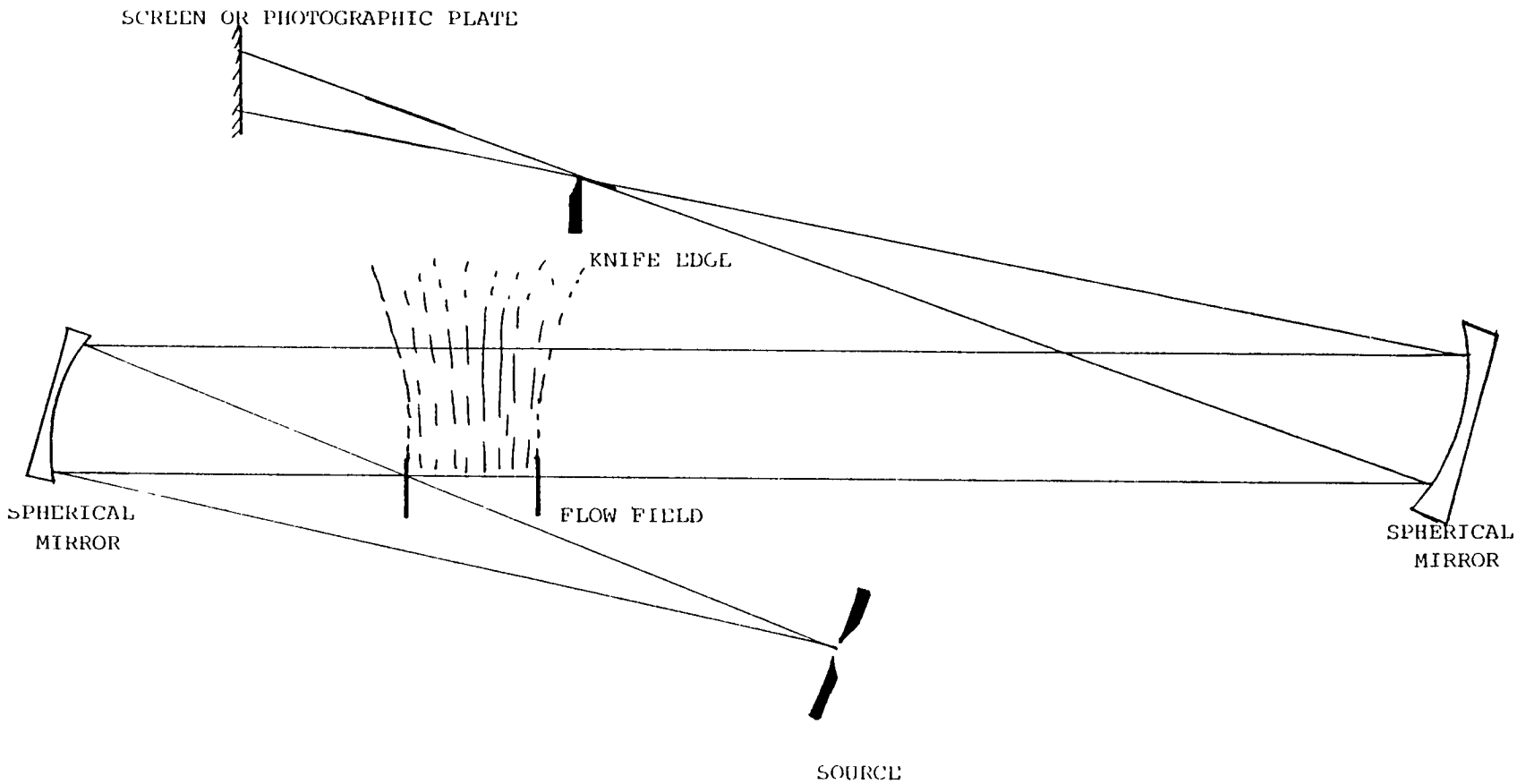

Figure 3.8a Schematic of a schlieren system

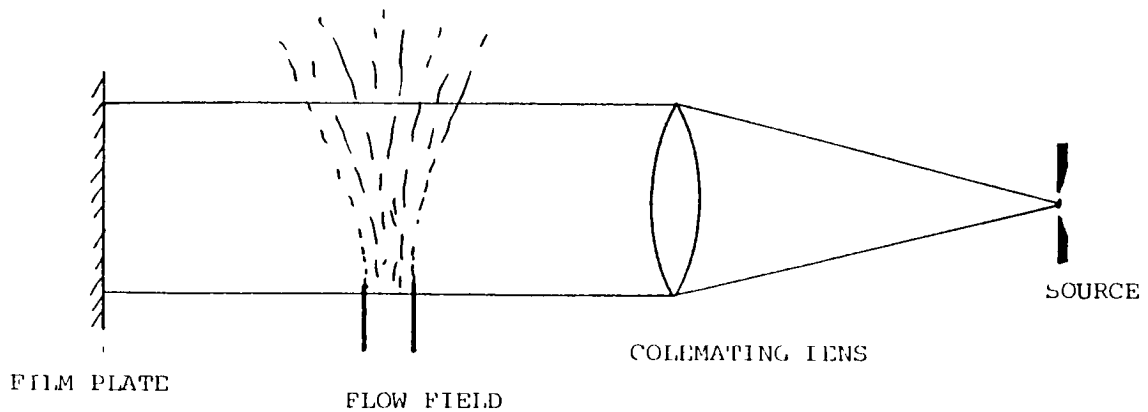

Figure 3.8b Schematic of a shadowgraph system

a

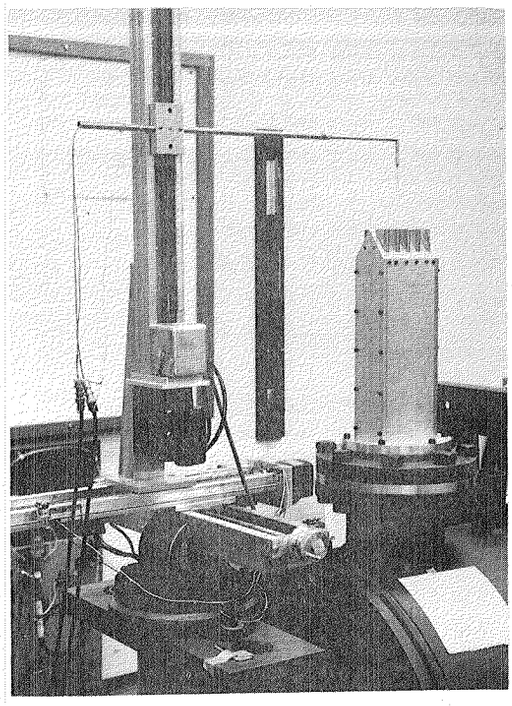

b

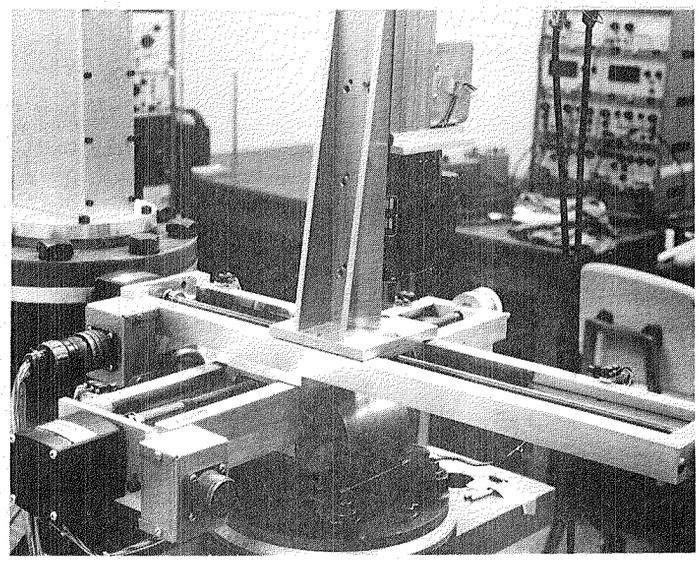

Figure 3.9 a) Traversing mechanism with the probe in position
b) Close view of the base of the mechanism

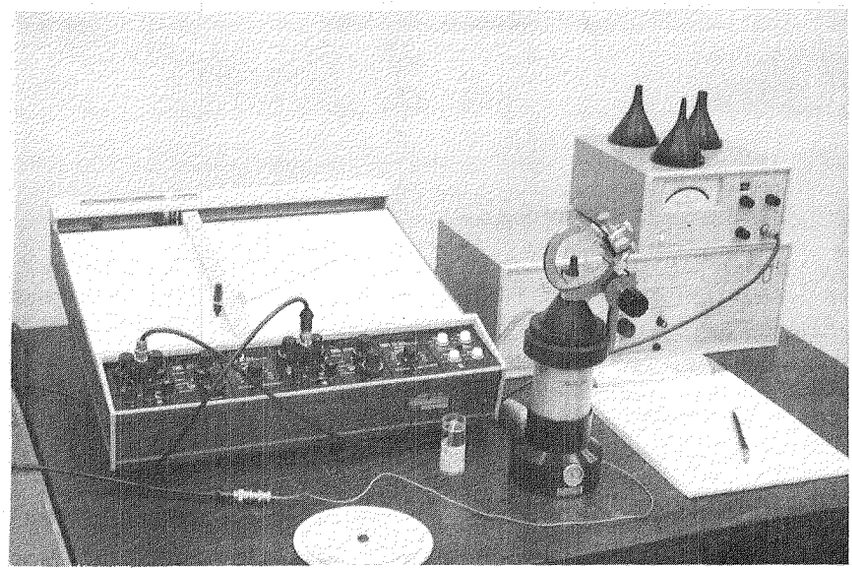

Figure 3.10 Hotwire calibration equipment

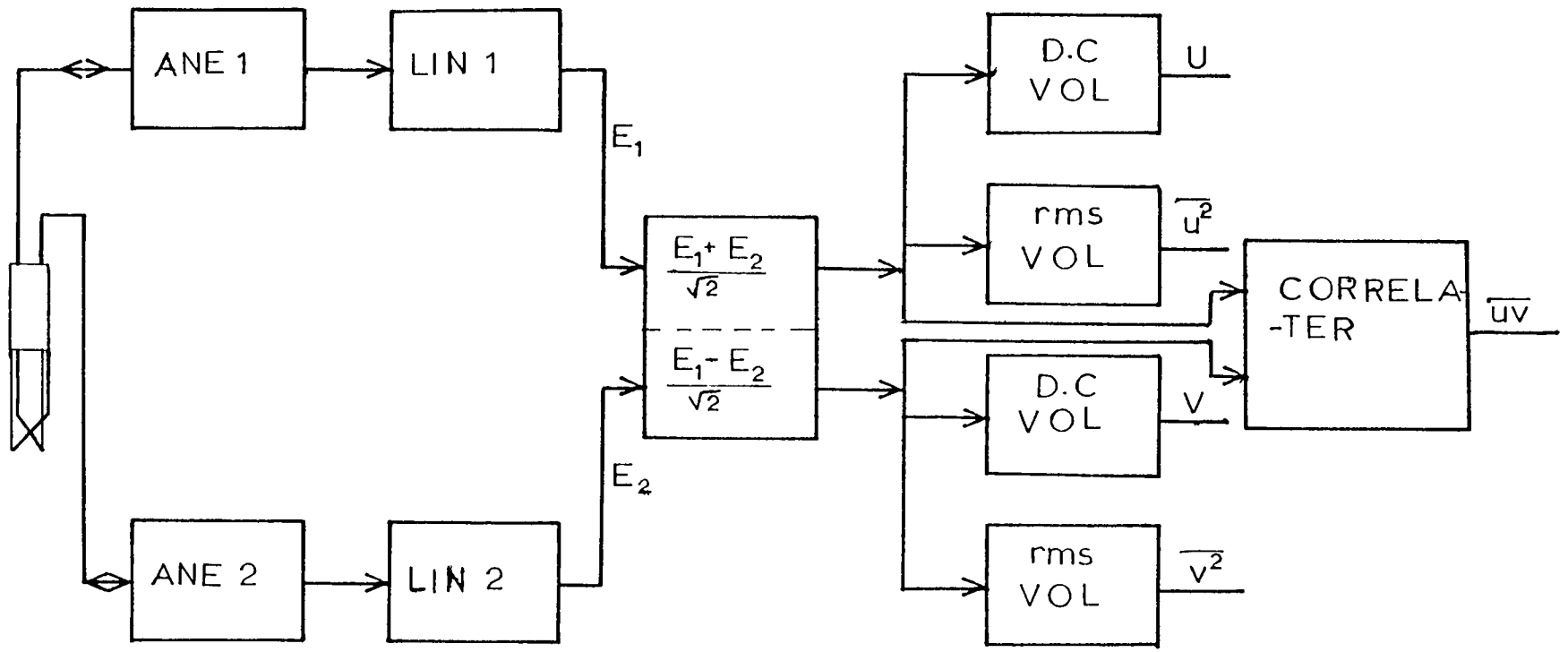

Figure 3.11 Arrangement of various signal processing instrumentation

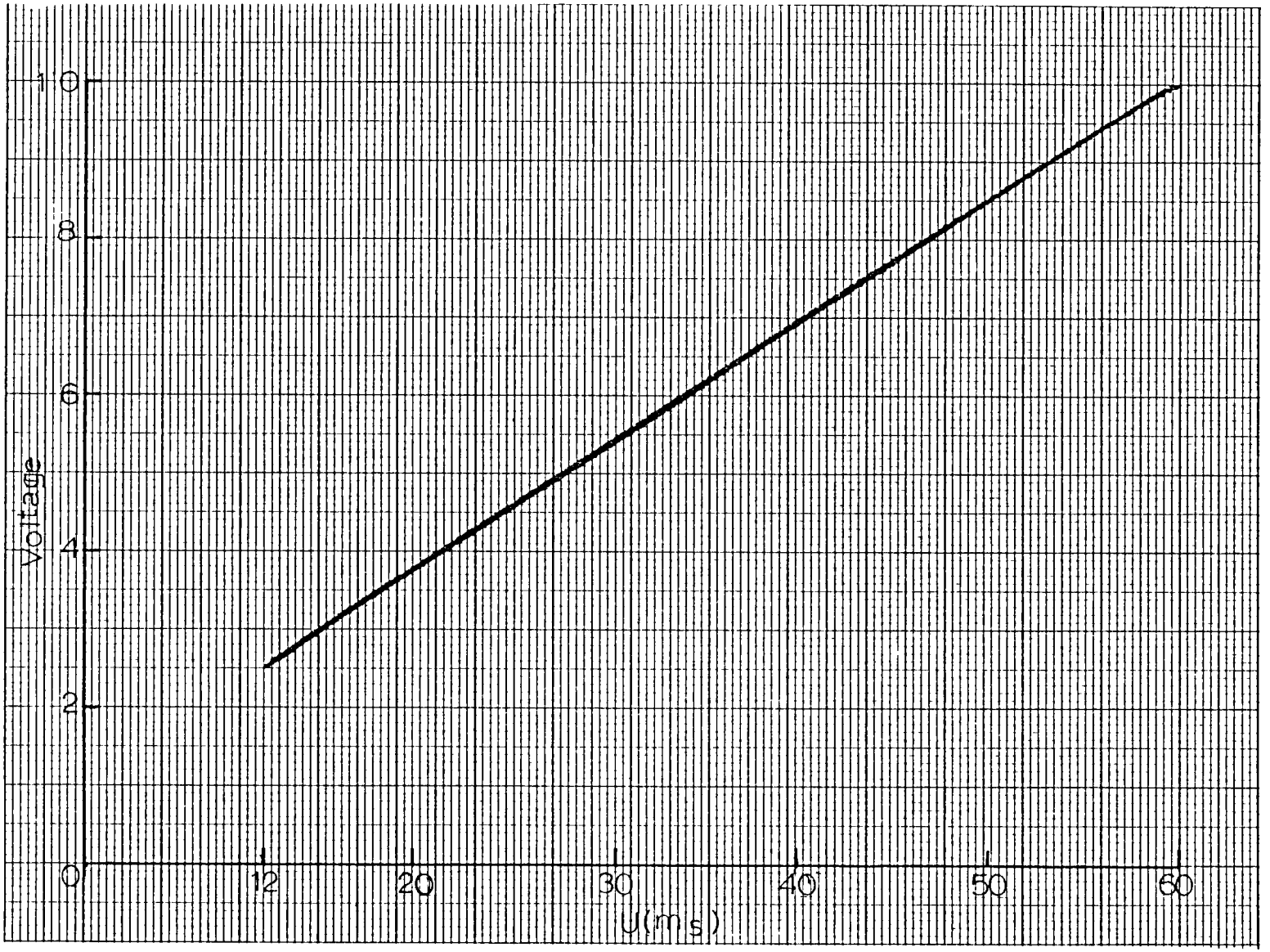

Figure 3.13 Calibration curve for the x-wire

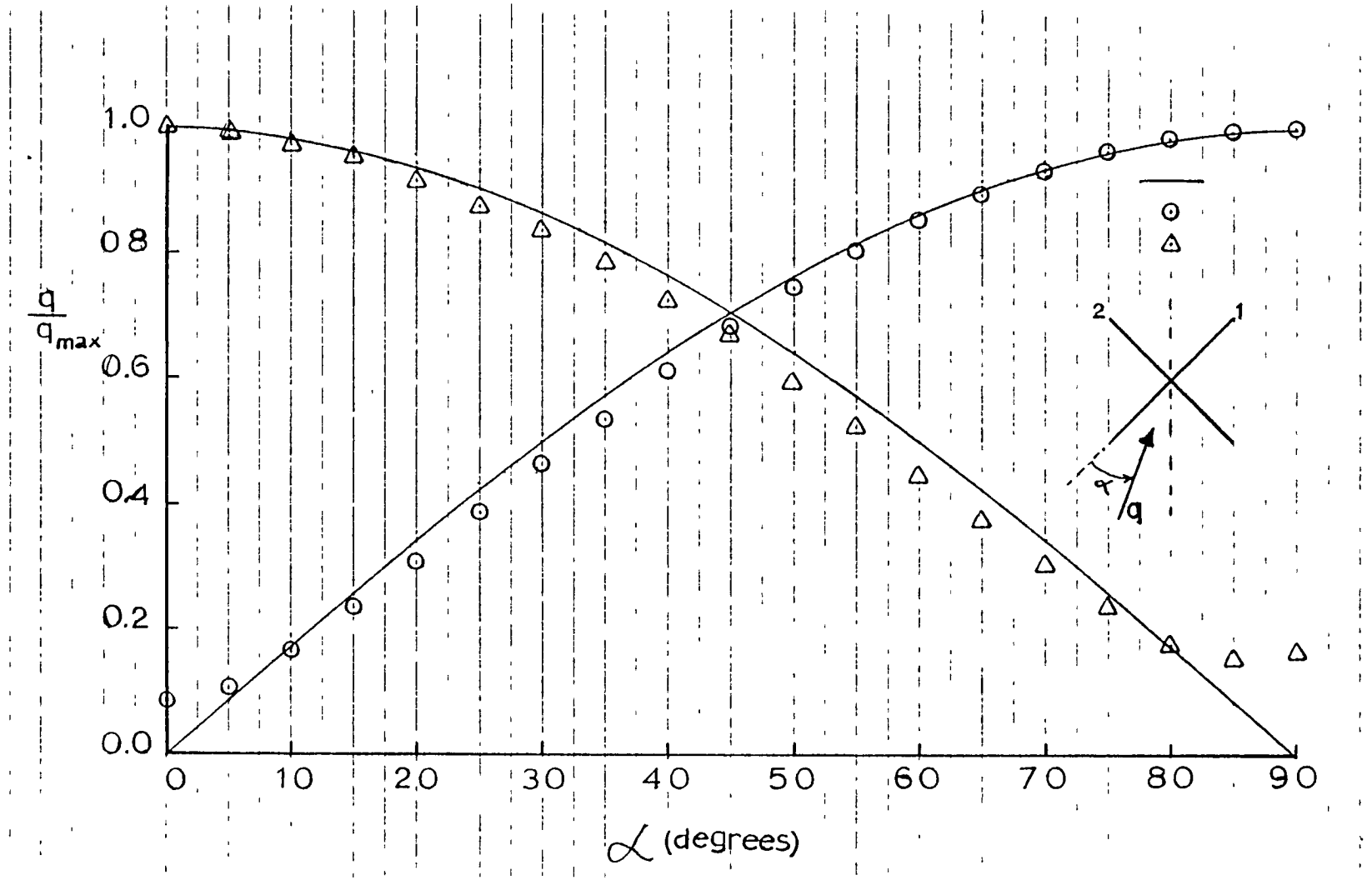

Figure 3.14 Angular calibration of the x-wire

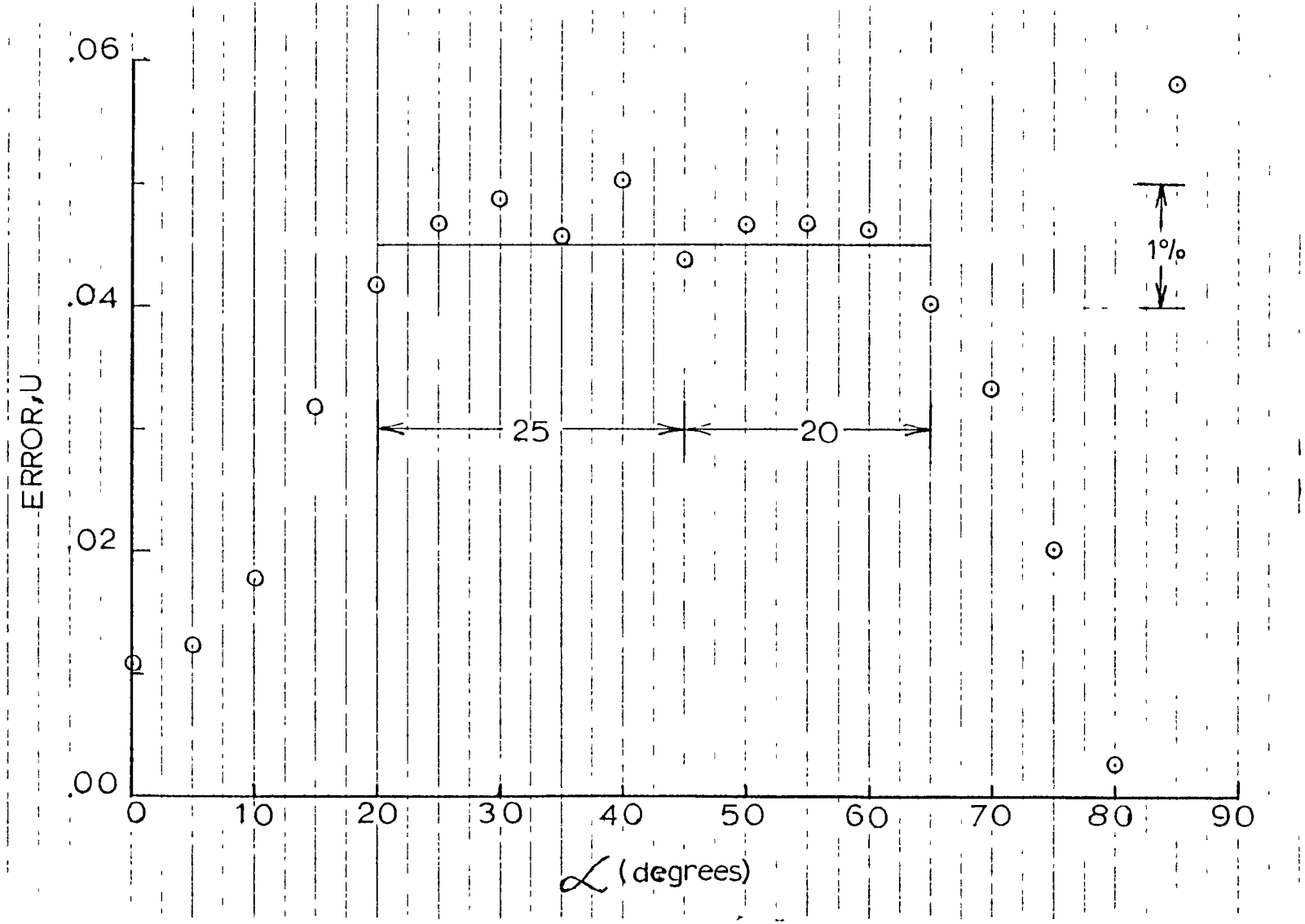

Figure 3.15 Estimated error for the U component of the velocity

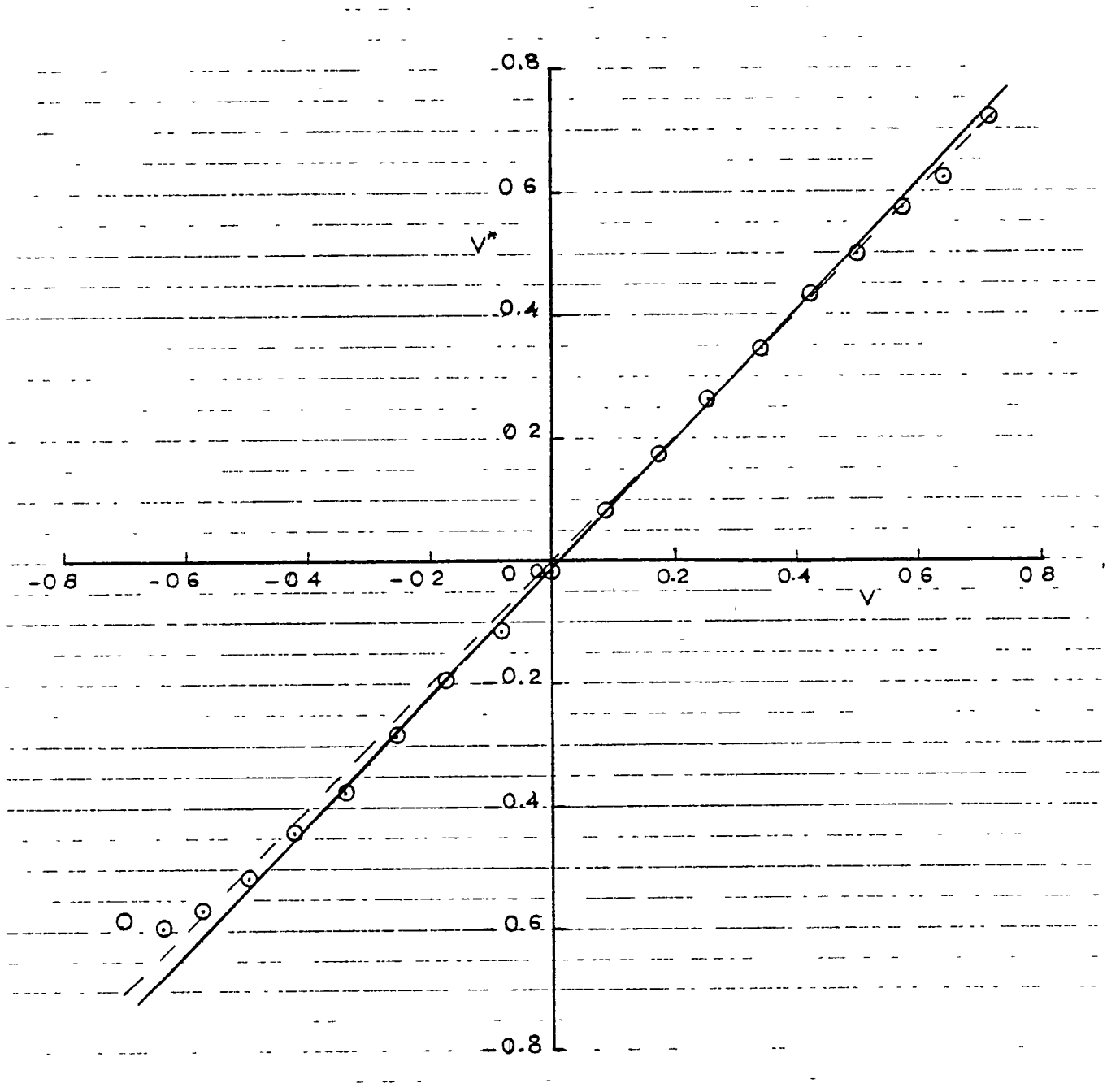

Figure 3.16 Estimated error for the V component of the velocity

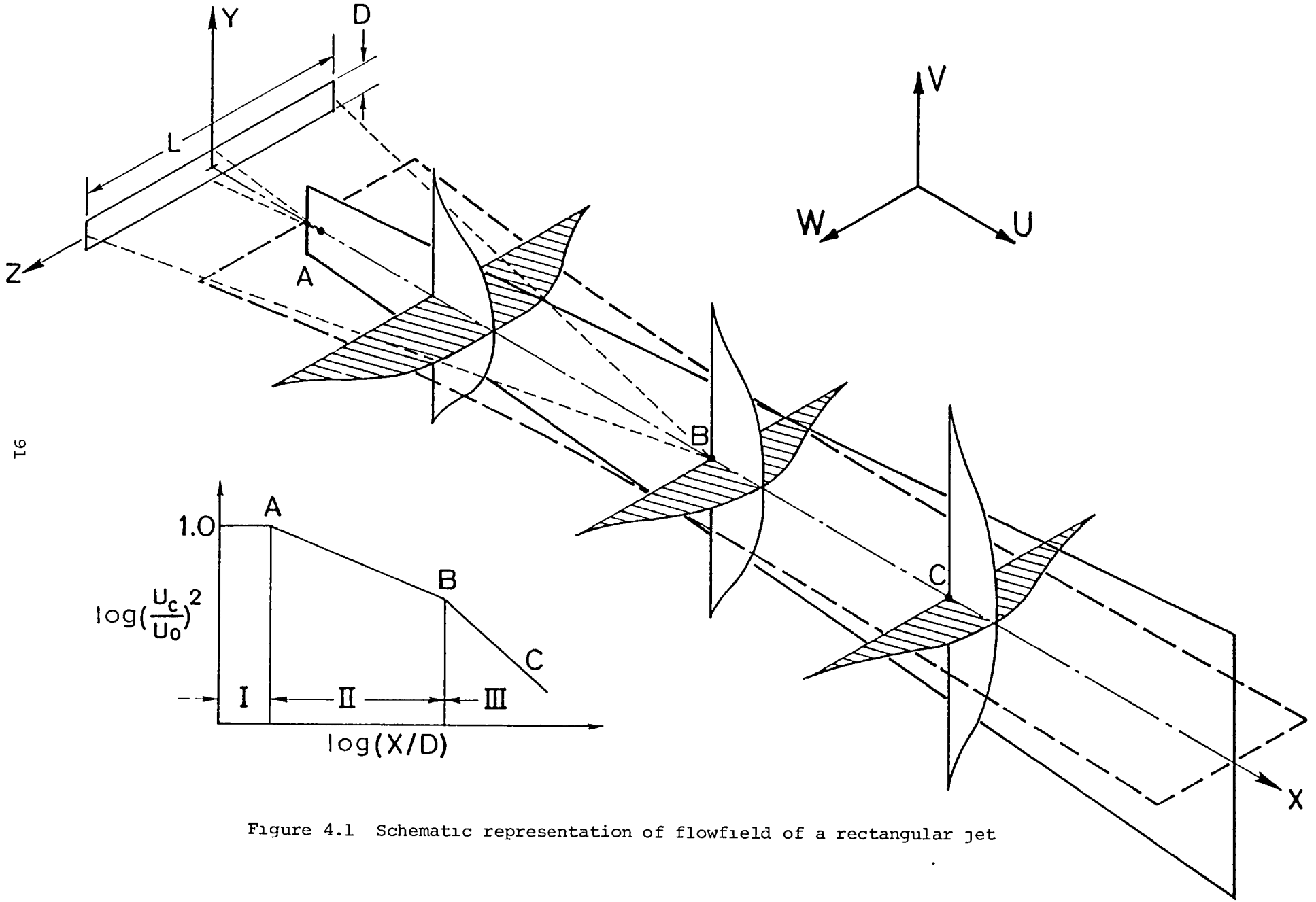

Figure 4.1 Schematic representation of flowfield of a rectangular jet

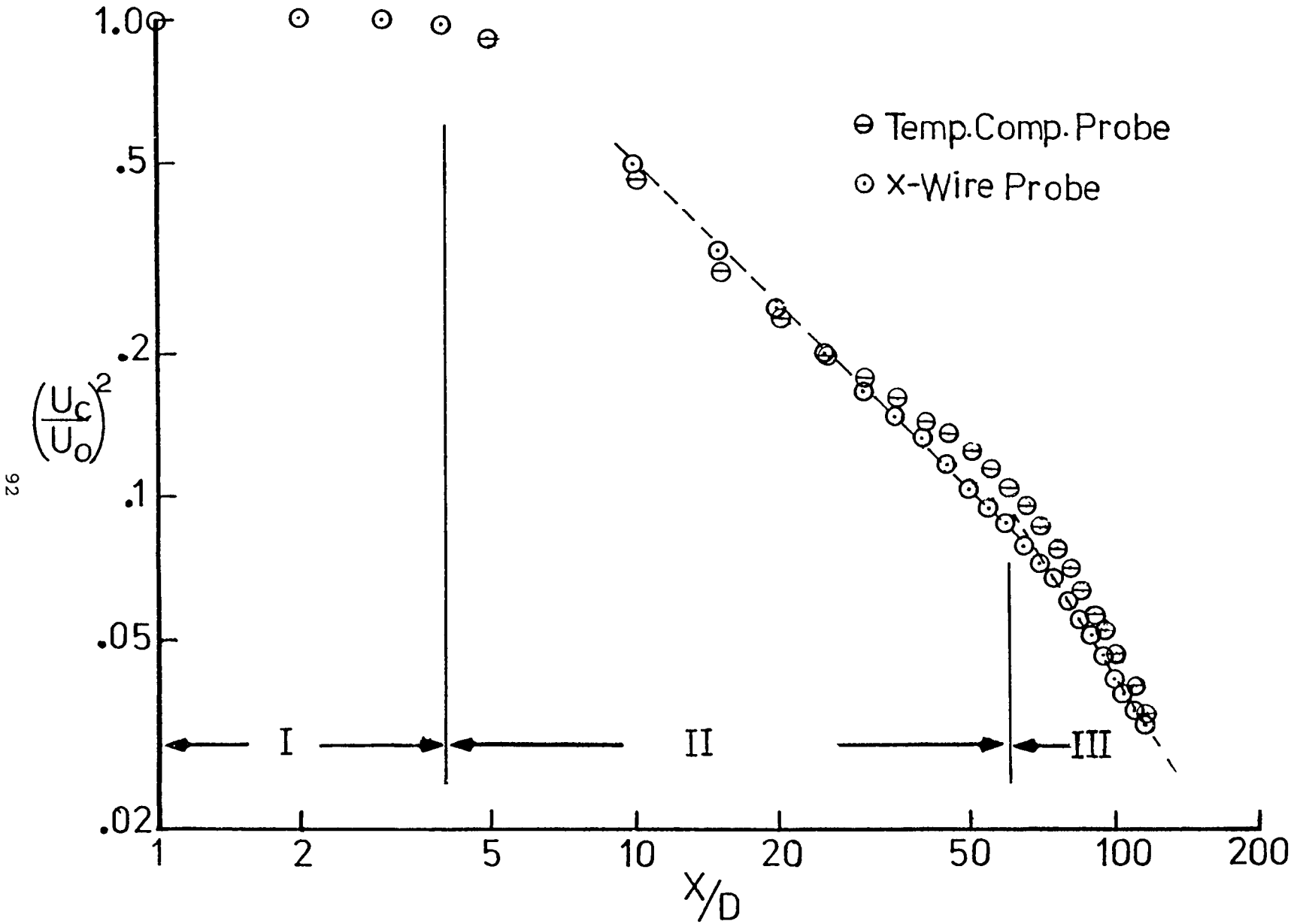

Figure 4.2a The decay of the axial mean velocity along the centerline of the jet

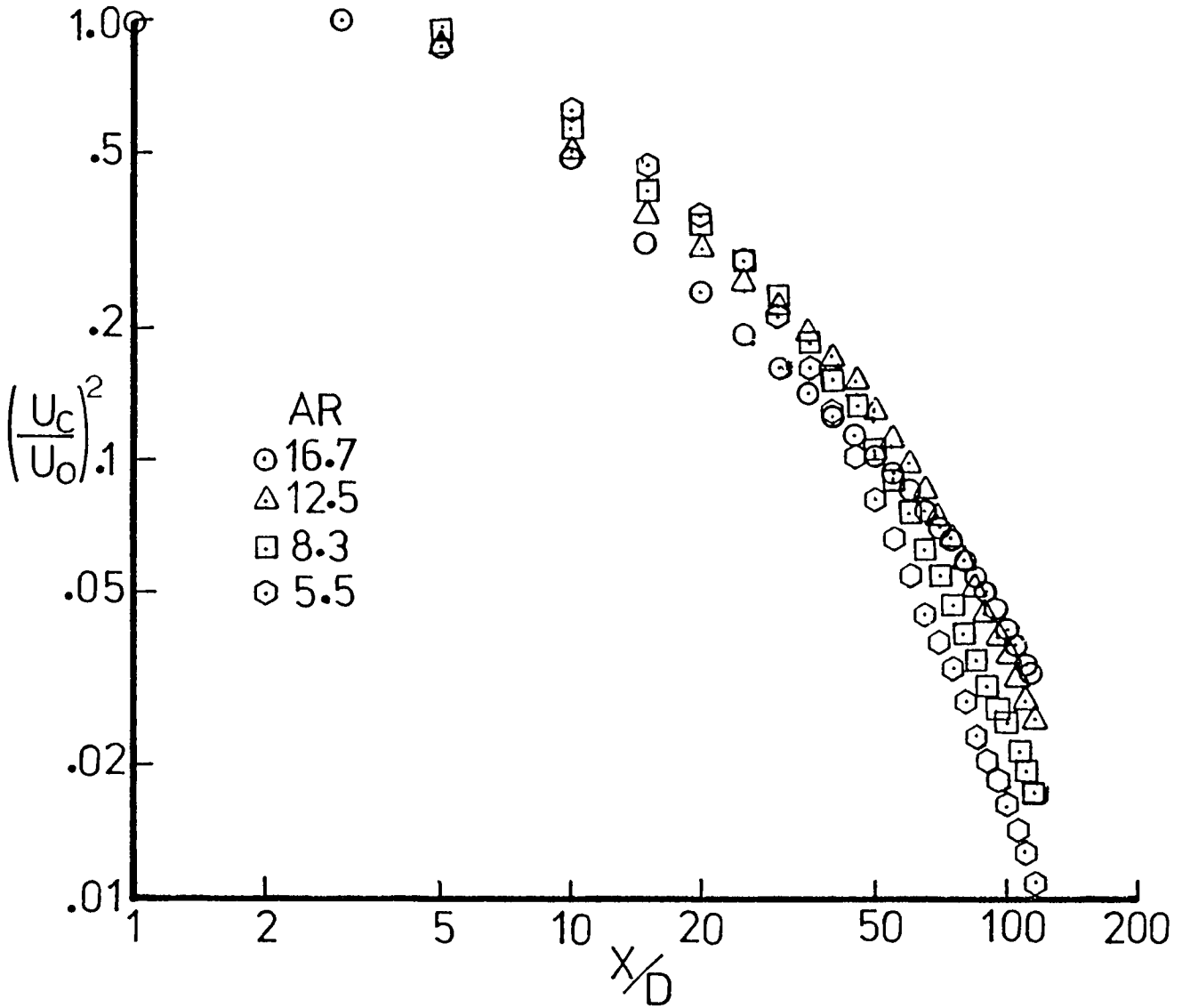

Figure 4.2b The decay of the axial mean velocity along the centerline of the jet

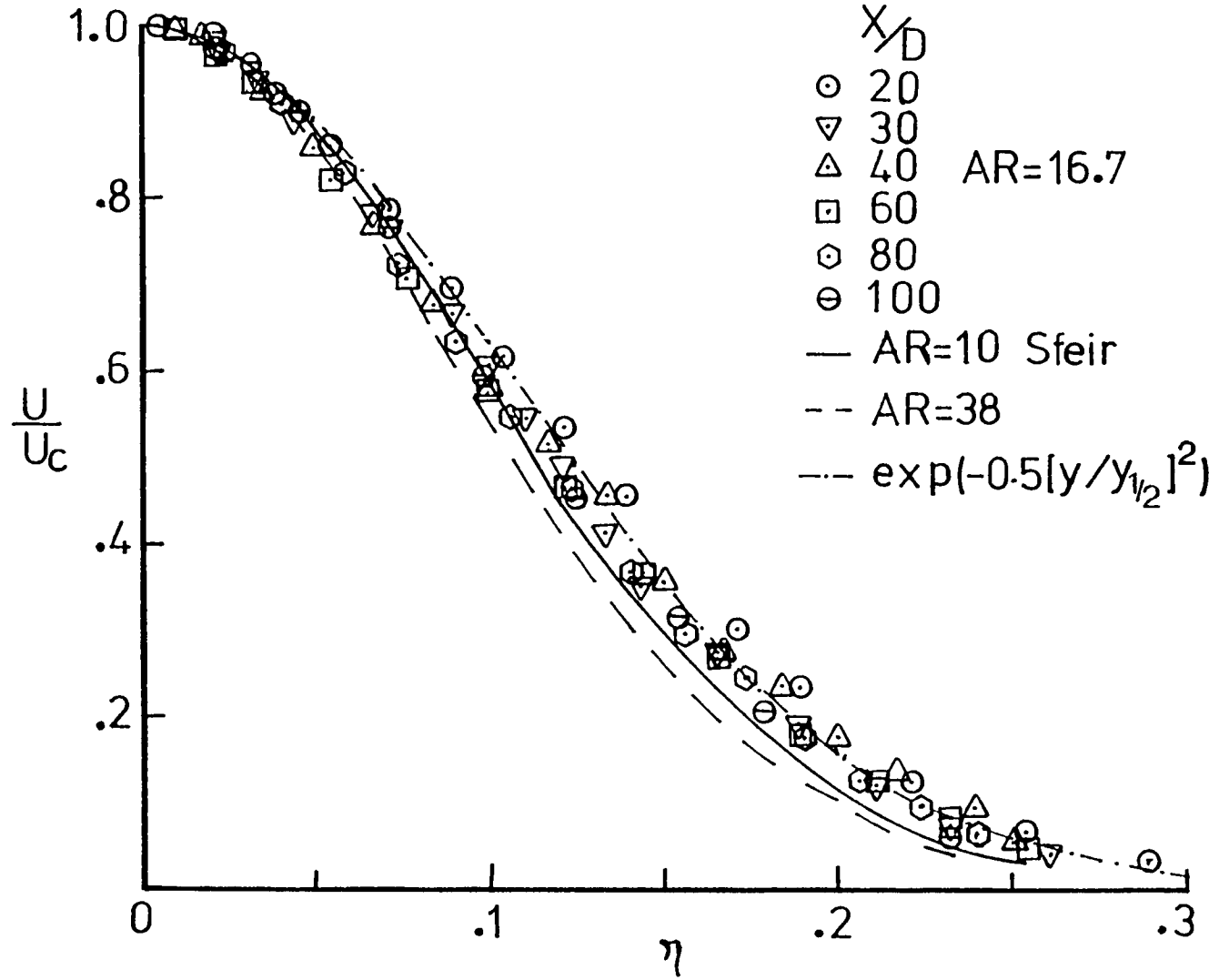

Figure 4.3 Axial mean velocity profiles in the x,y plane

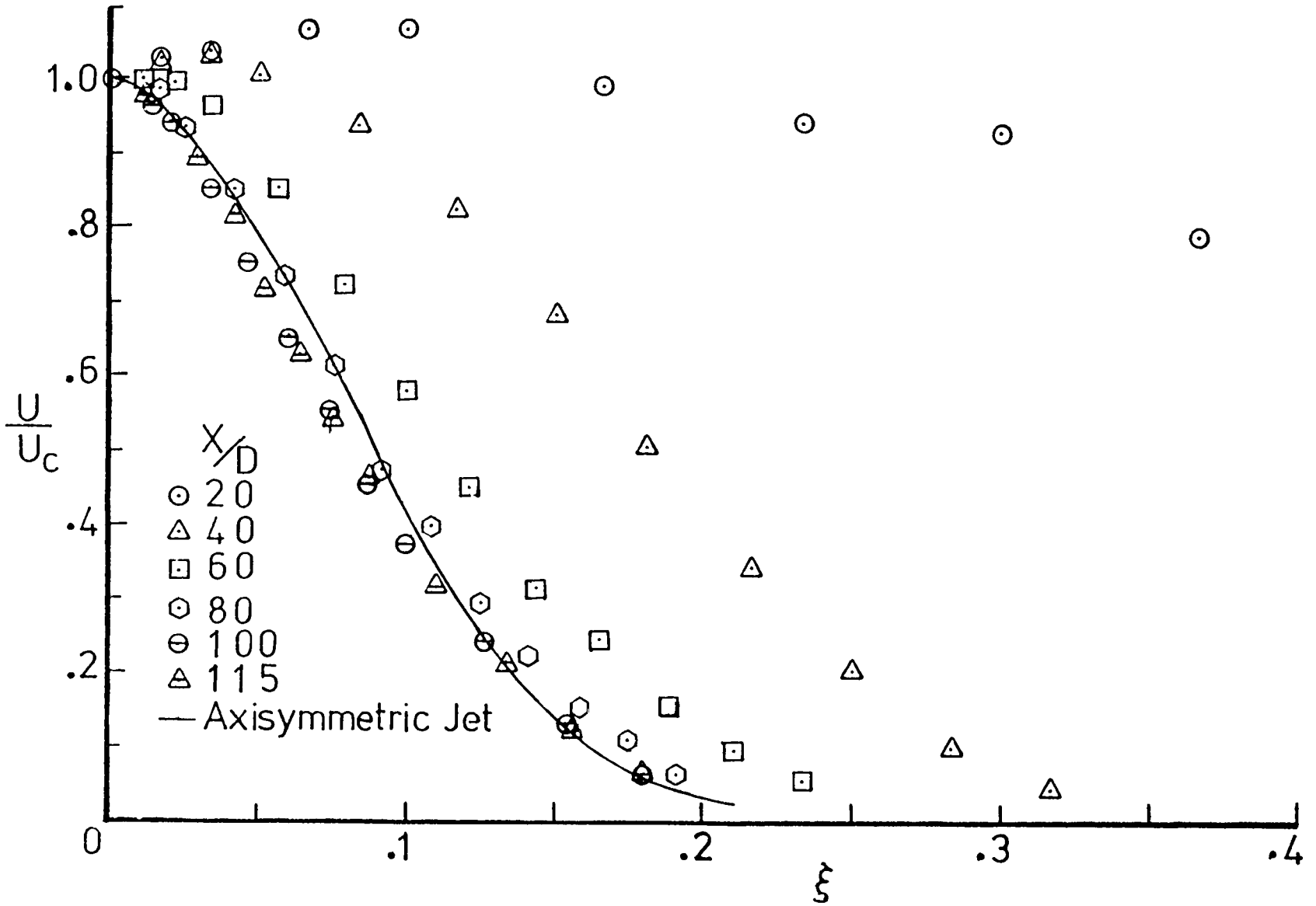

Figure 4.4 Axial mean velocity profiles in the x,z plane

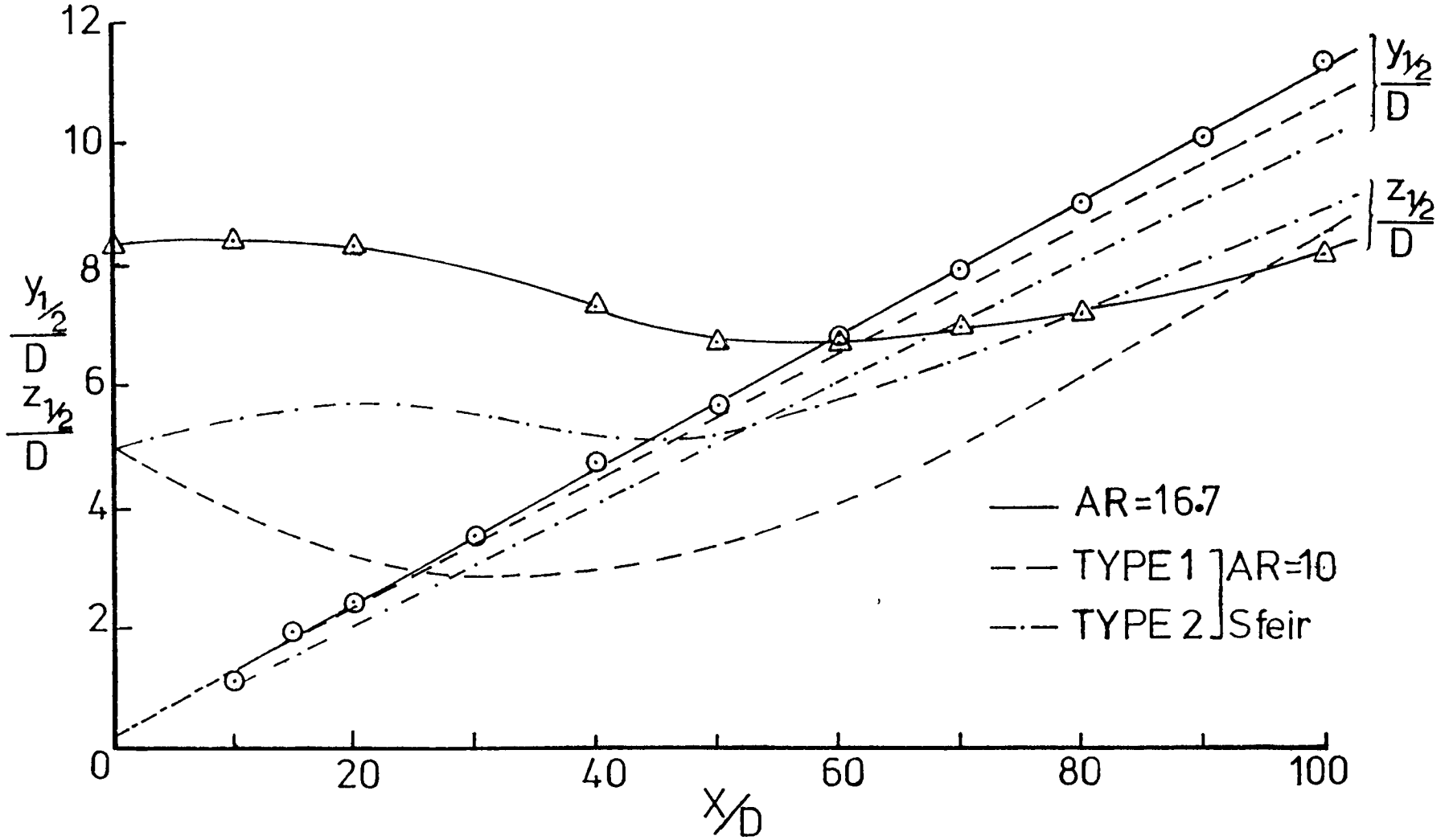

Figure 4.5a The growth of the jet with downstream distance

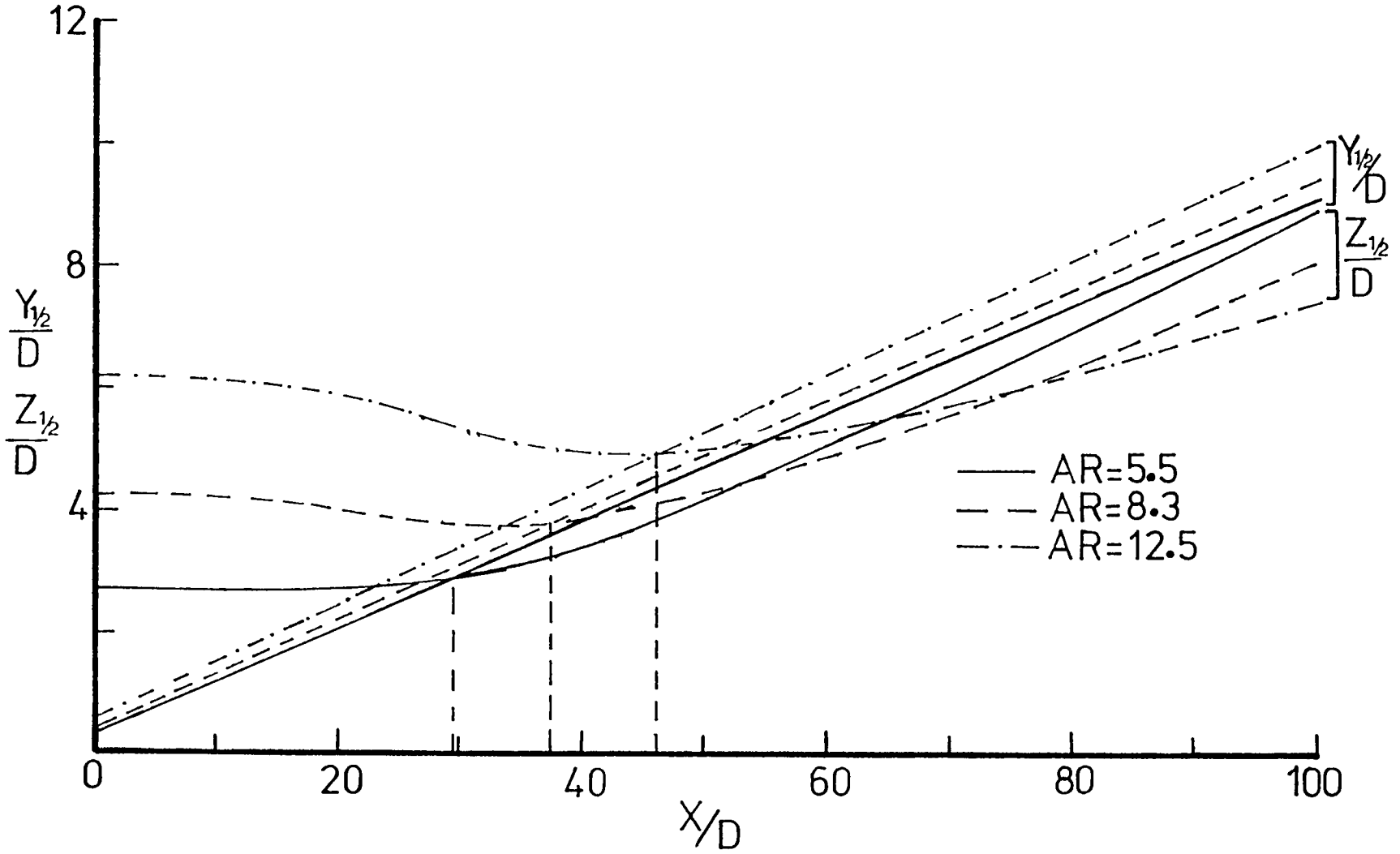

Figure 4.5b The growth of the jet with downstream distance

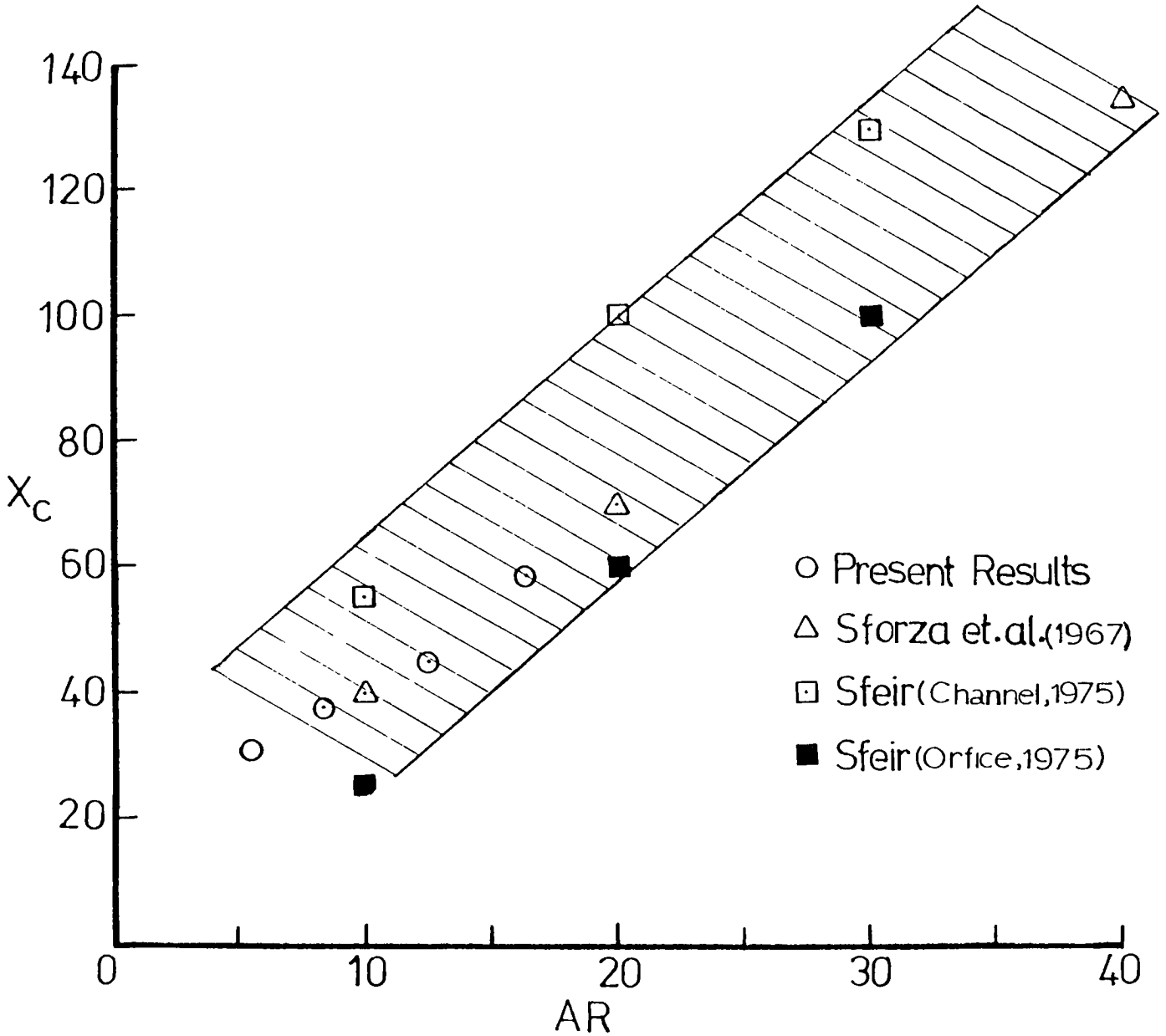

Figure 4.6 Variation of the crossover point with aspect ratio

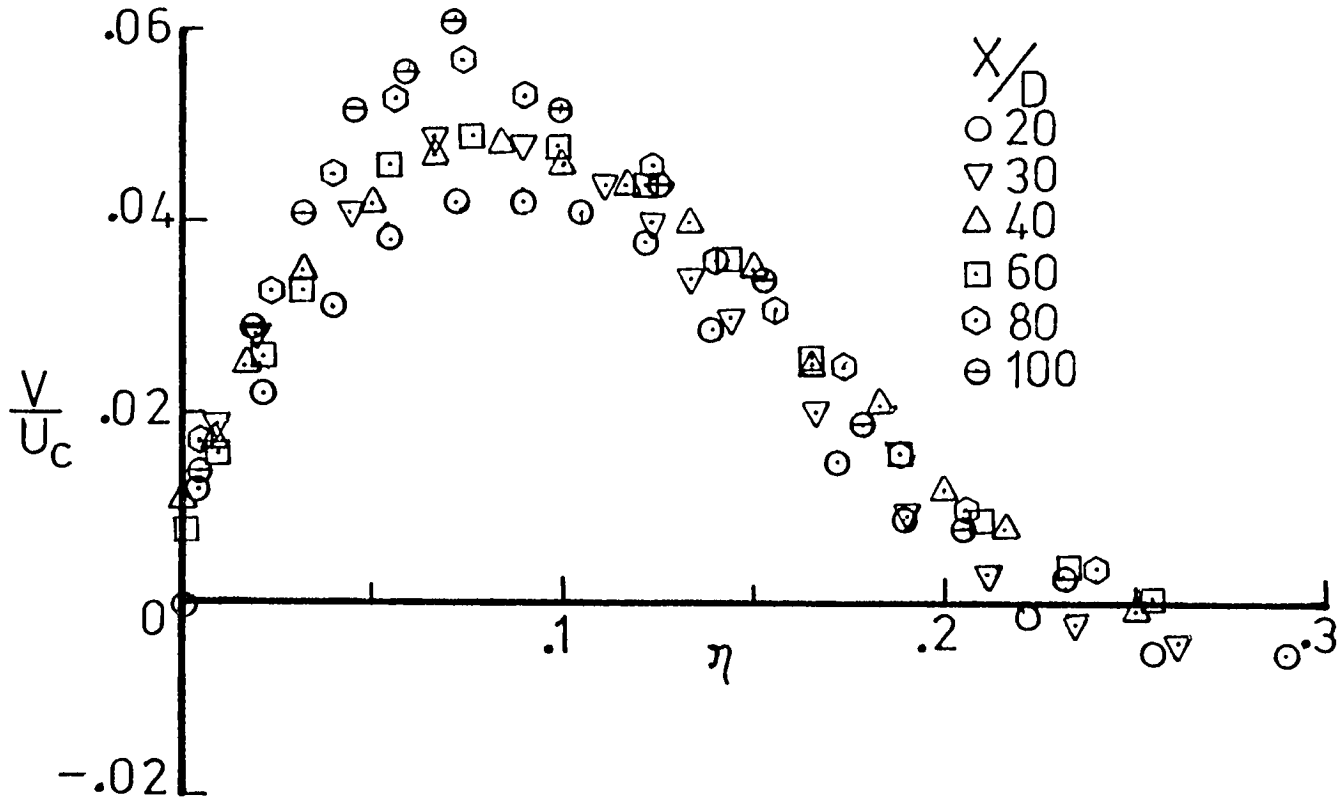

Figure 4.7 Lateral mean velocity profiles in the x,y plane

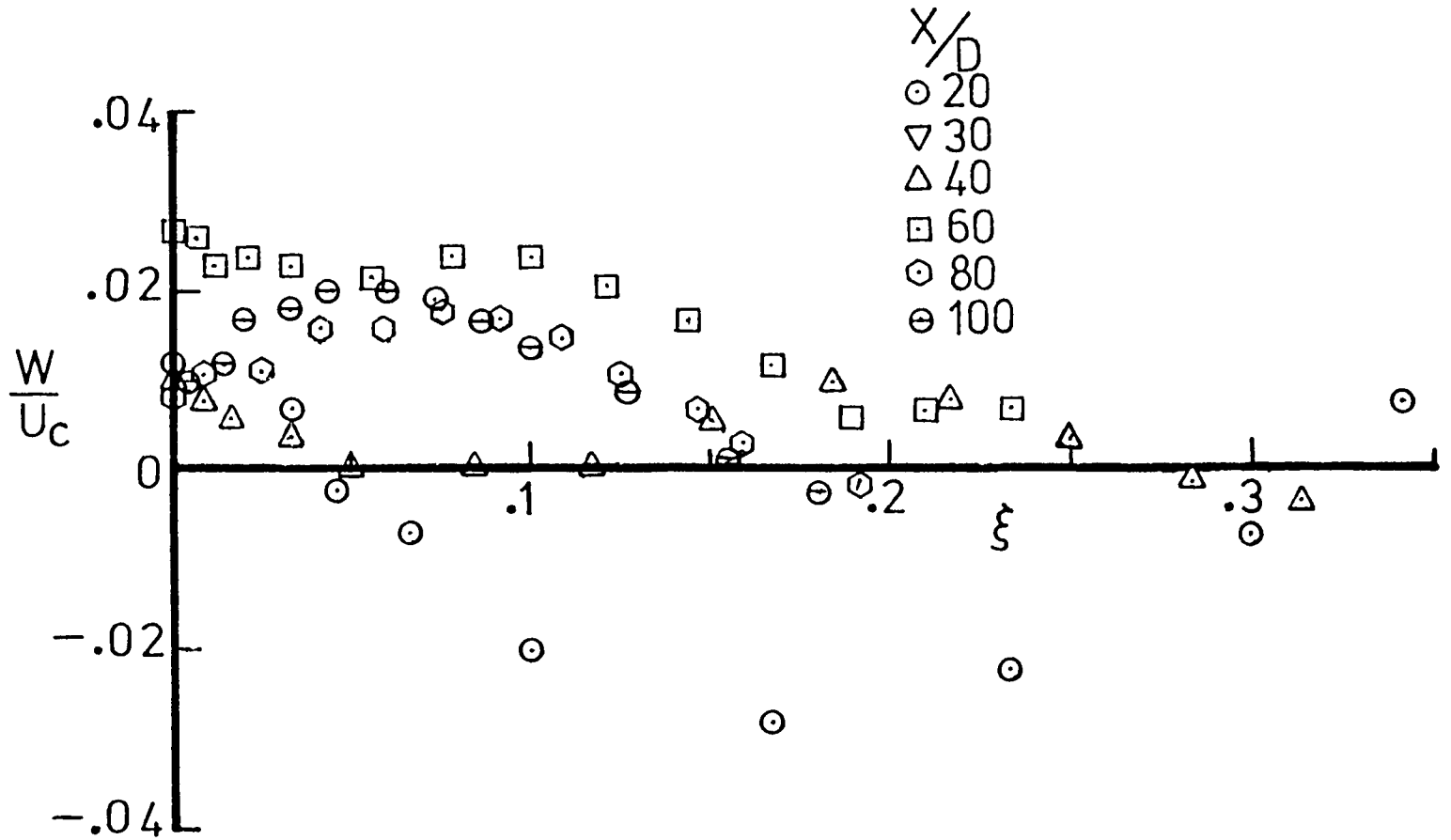

Figure 4.8 Transverse mean velocity profiles in the x,z plane

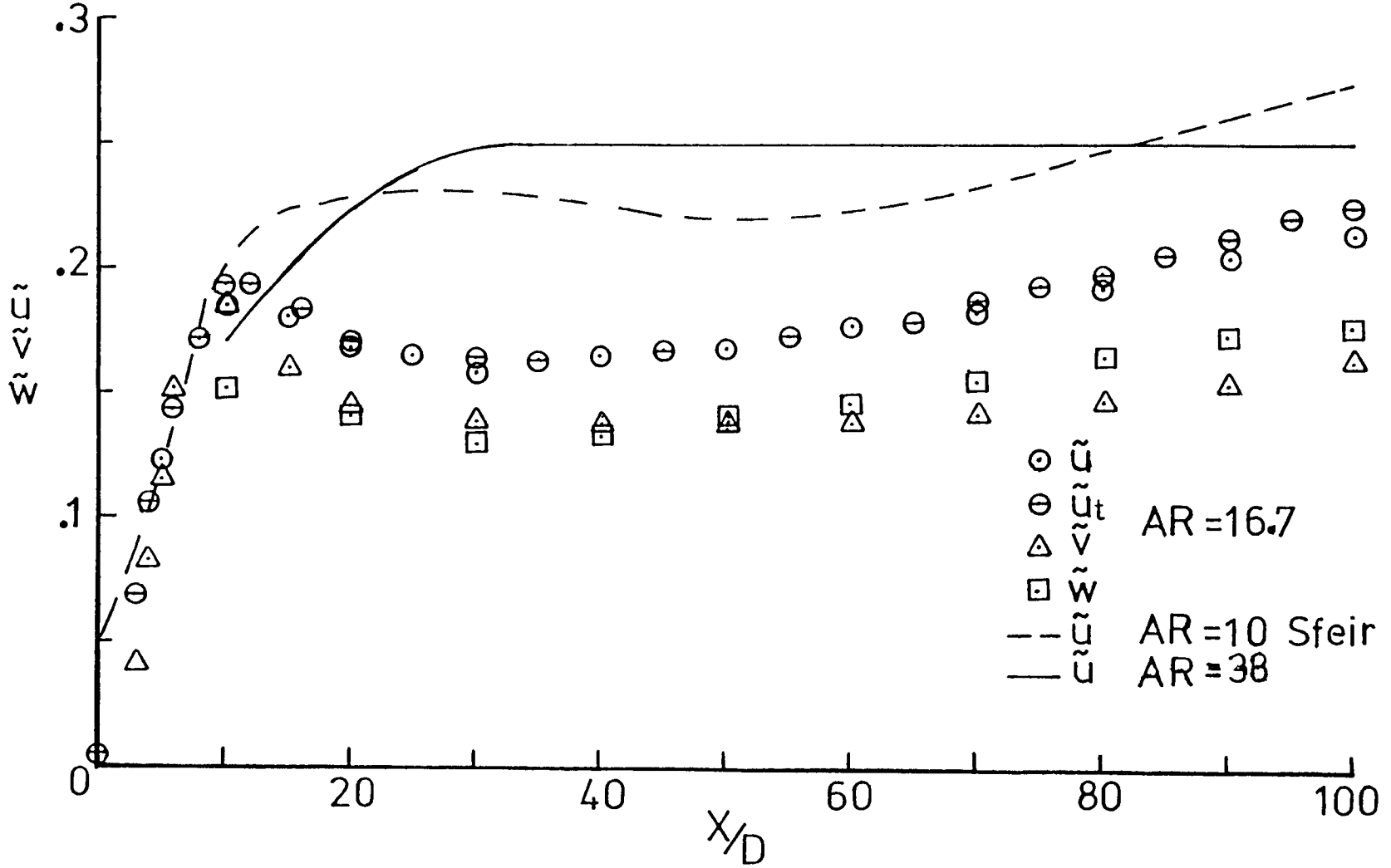

Figure 4.9 Variation of turbulent intensities along the centerline of the jet

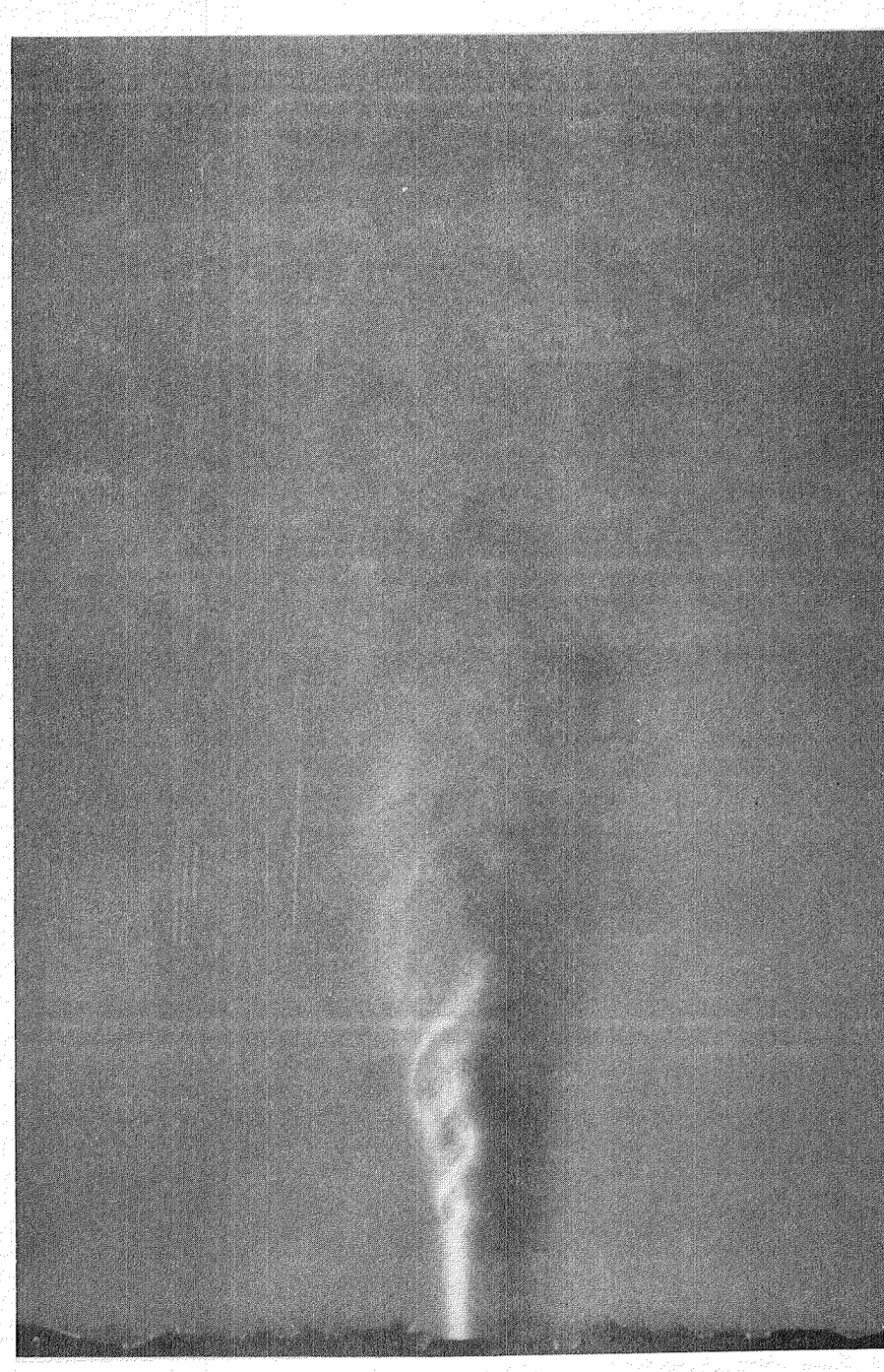

Figure 4.10 Schlieren picture of the jet in the x,y plane

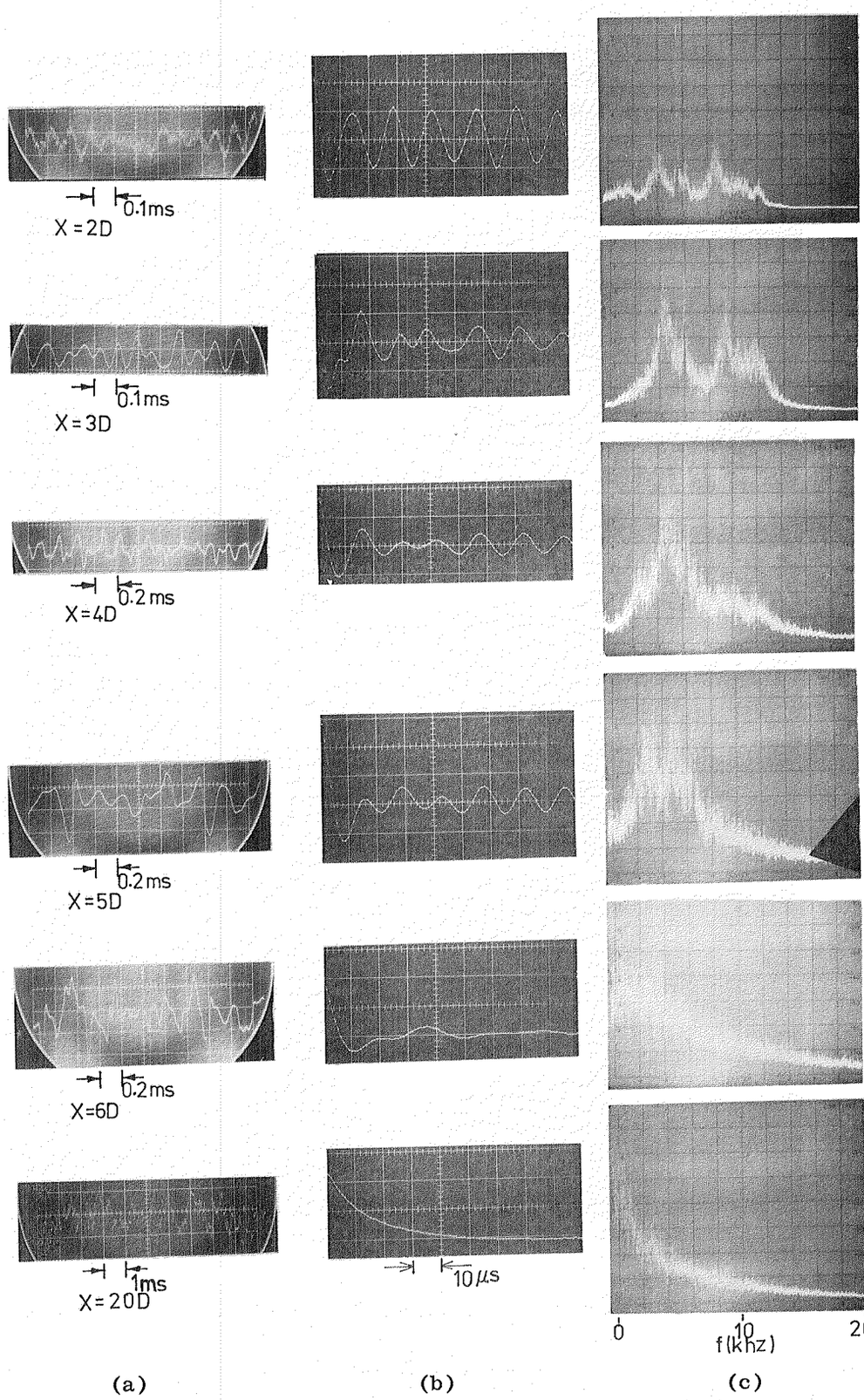

Figure 4.11 Signal, autocorrelation, spectrum, of u fluctuations along the centerline of the jet

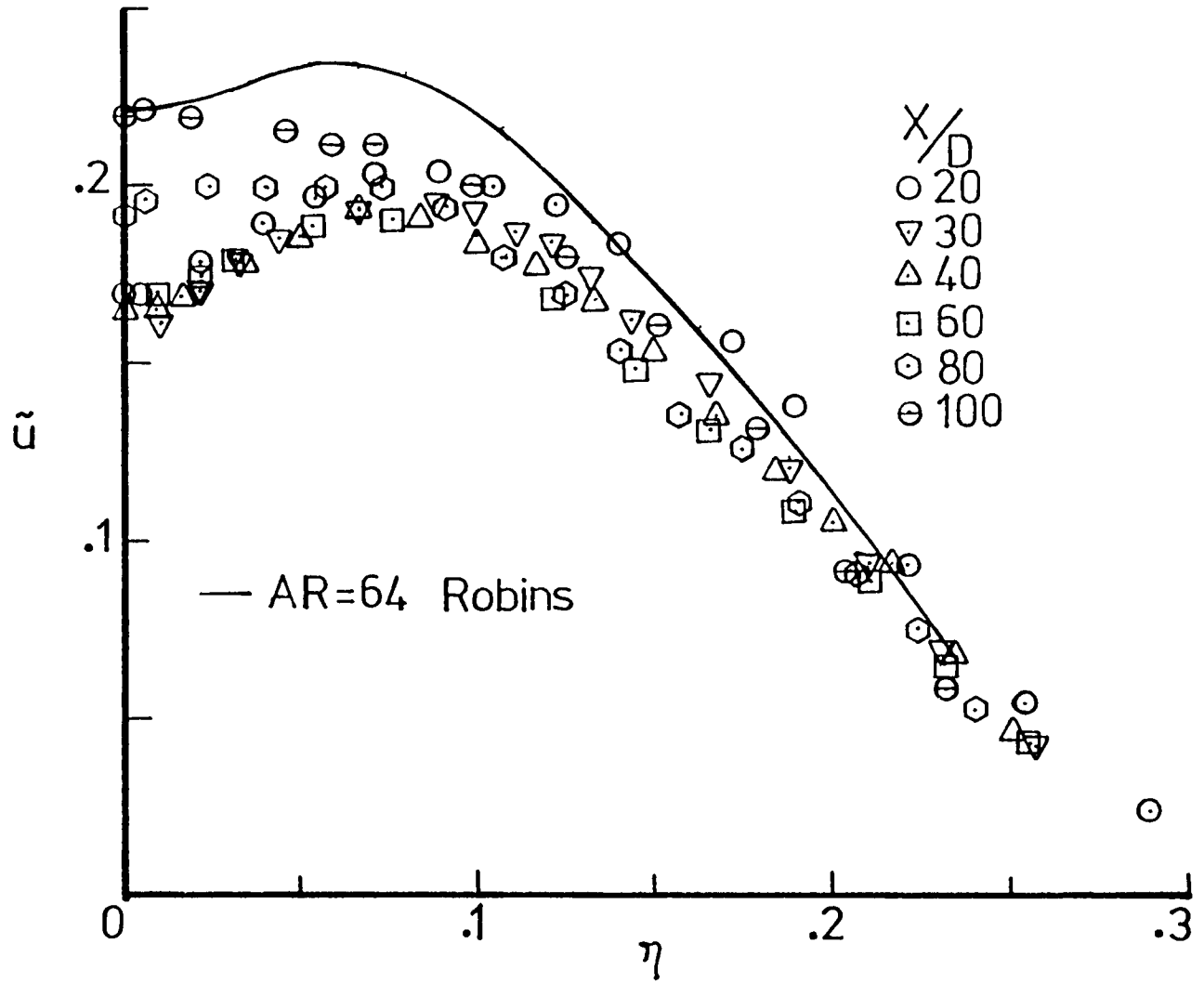

Figure 4.12 The distribution of the axial velocity fluctuations in the x,y plane

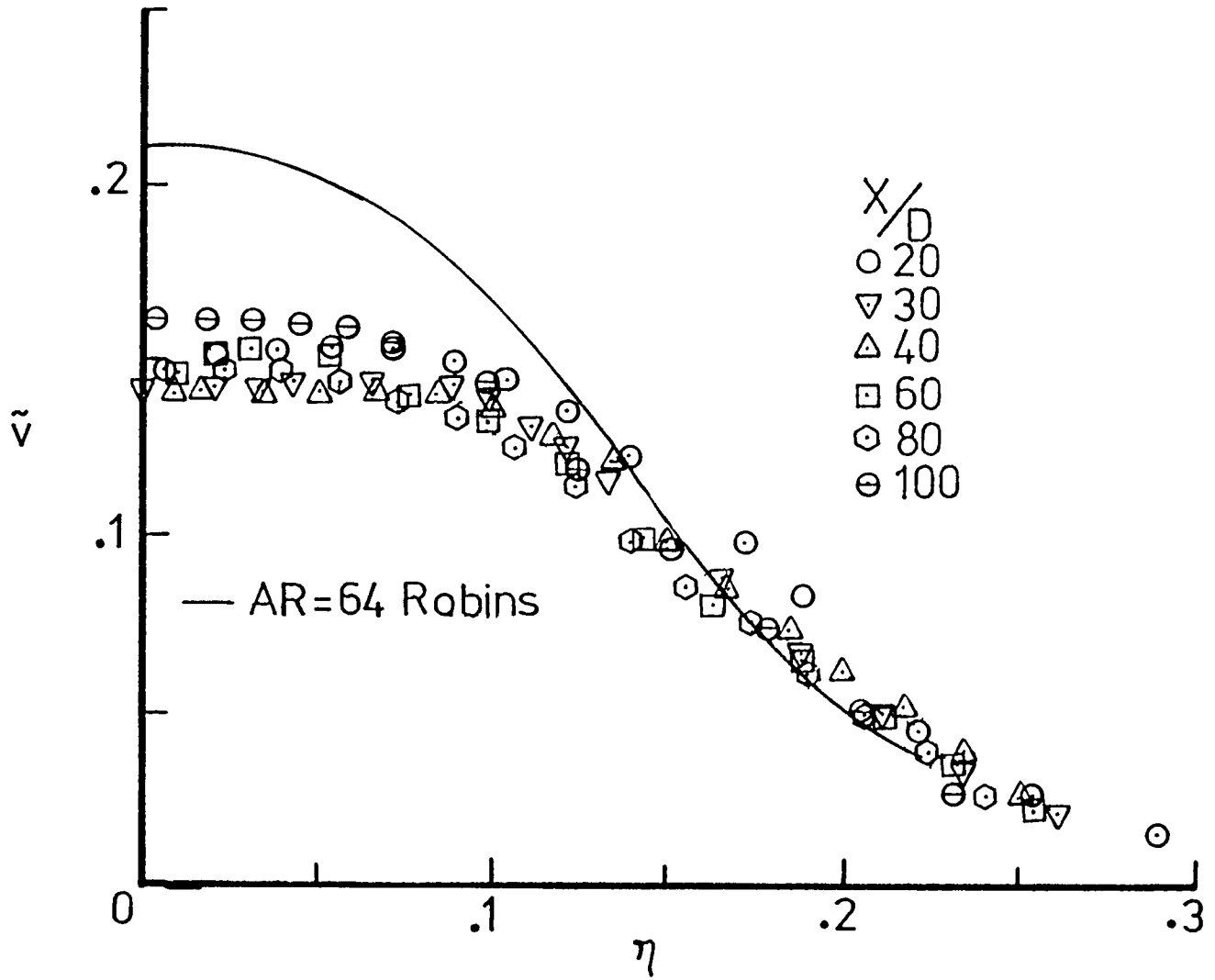

Figure 4.13 The distribution of the lateral velocity fluctuations in the x,y plane

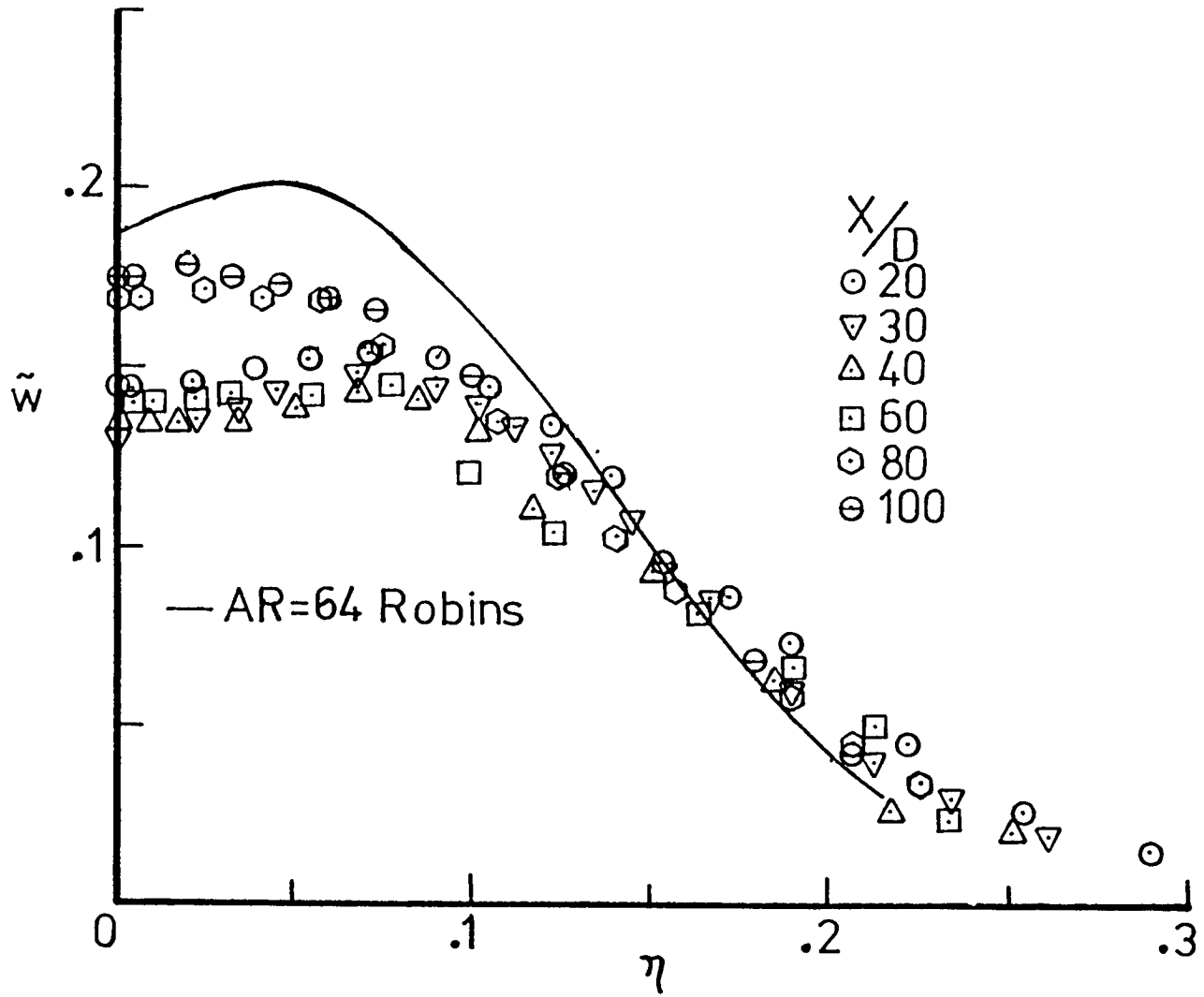

Figure 4.14 The distribution of the transverse velocity fluctuations in the x,y plane

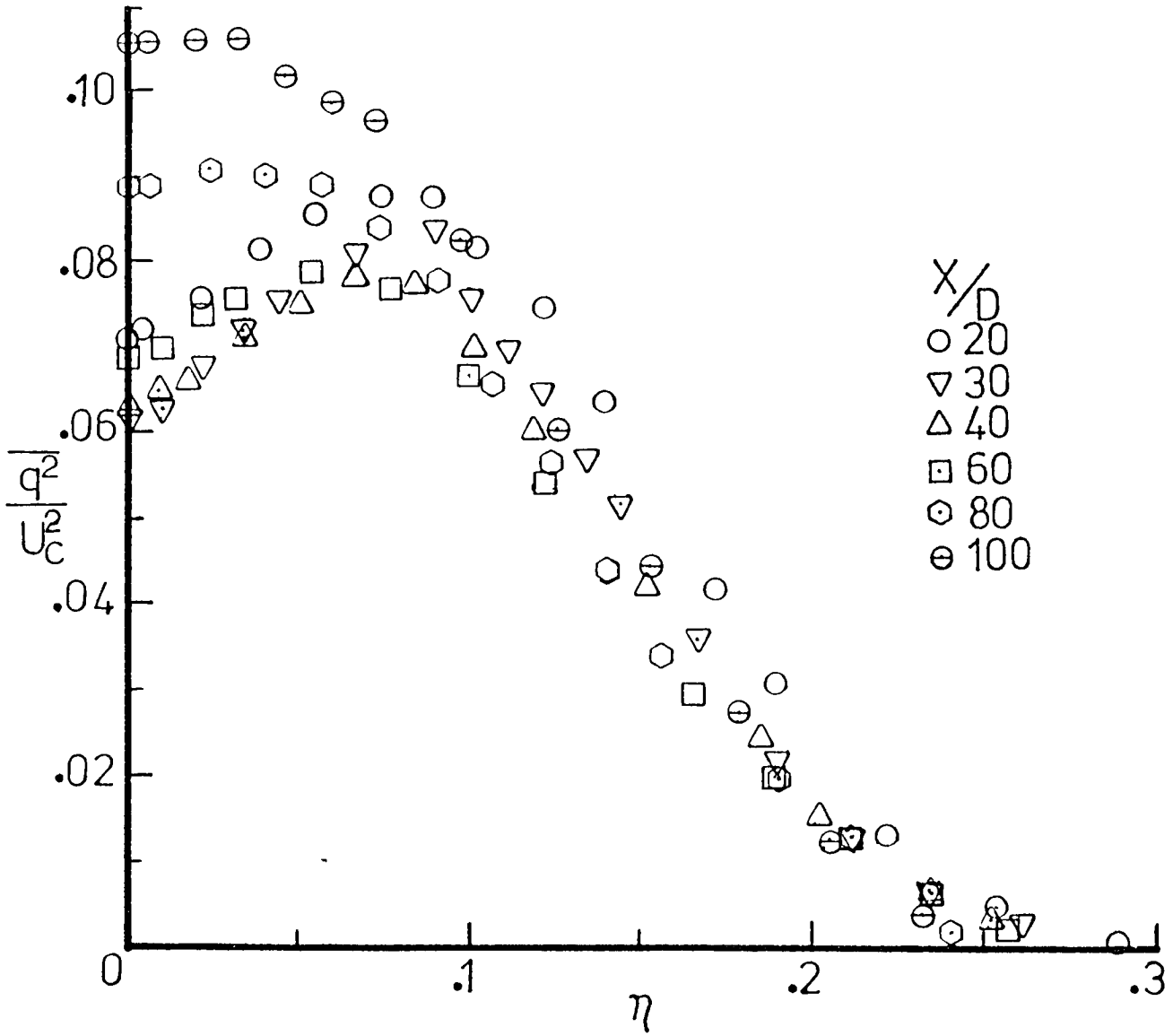

Figure 4.15 The distribution of the turbulent kinetic energy in the x,y plane

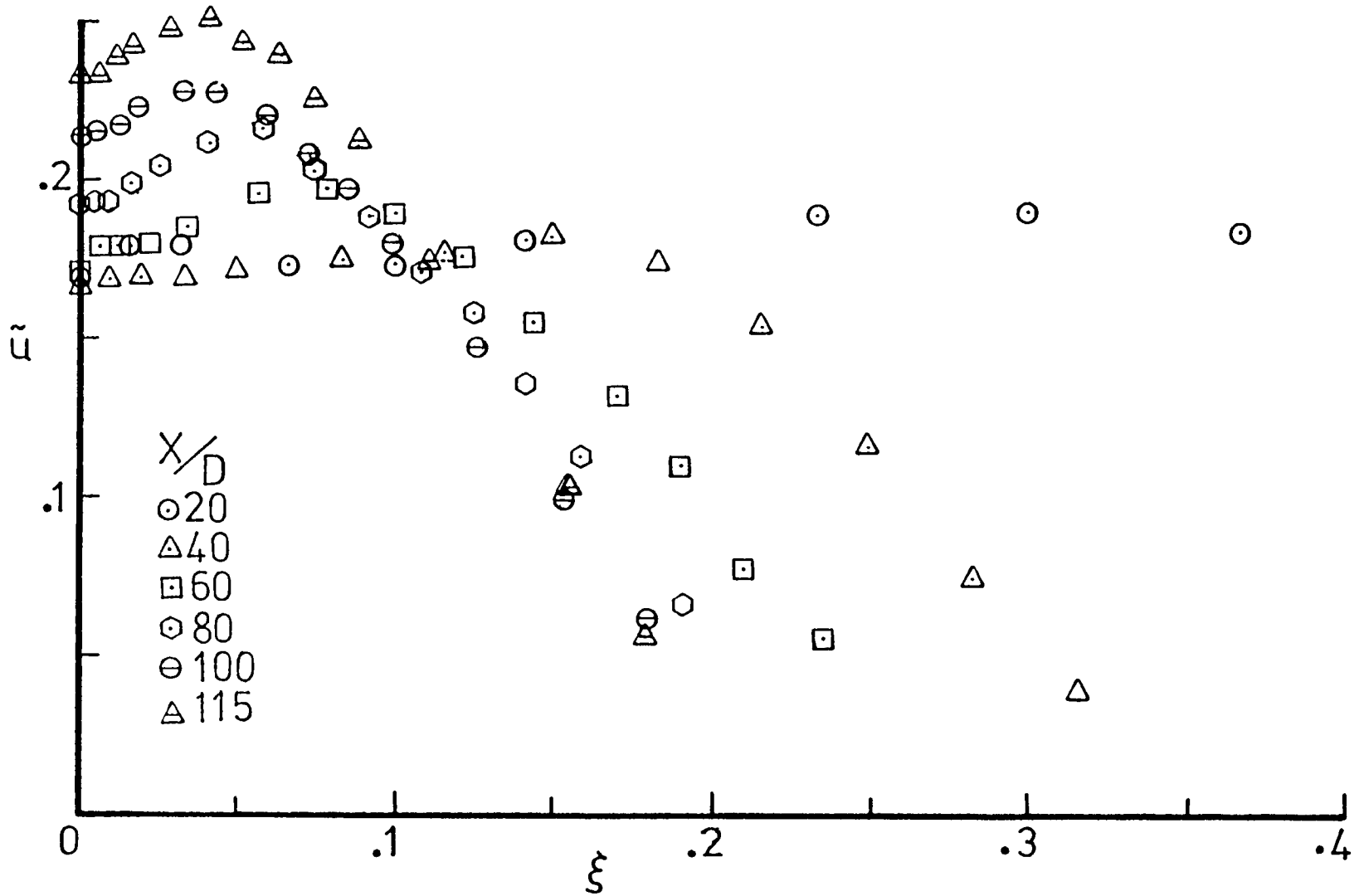

Figure 4.16 The distribution of the axial velocity fluctuations in the x,z plane

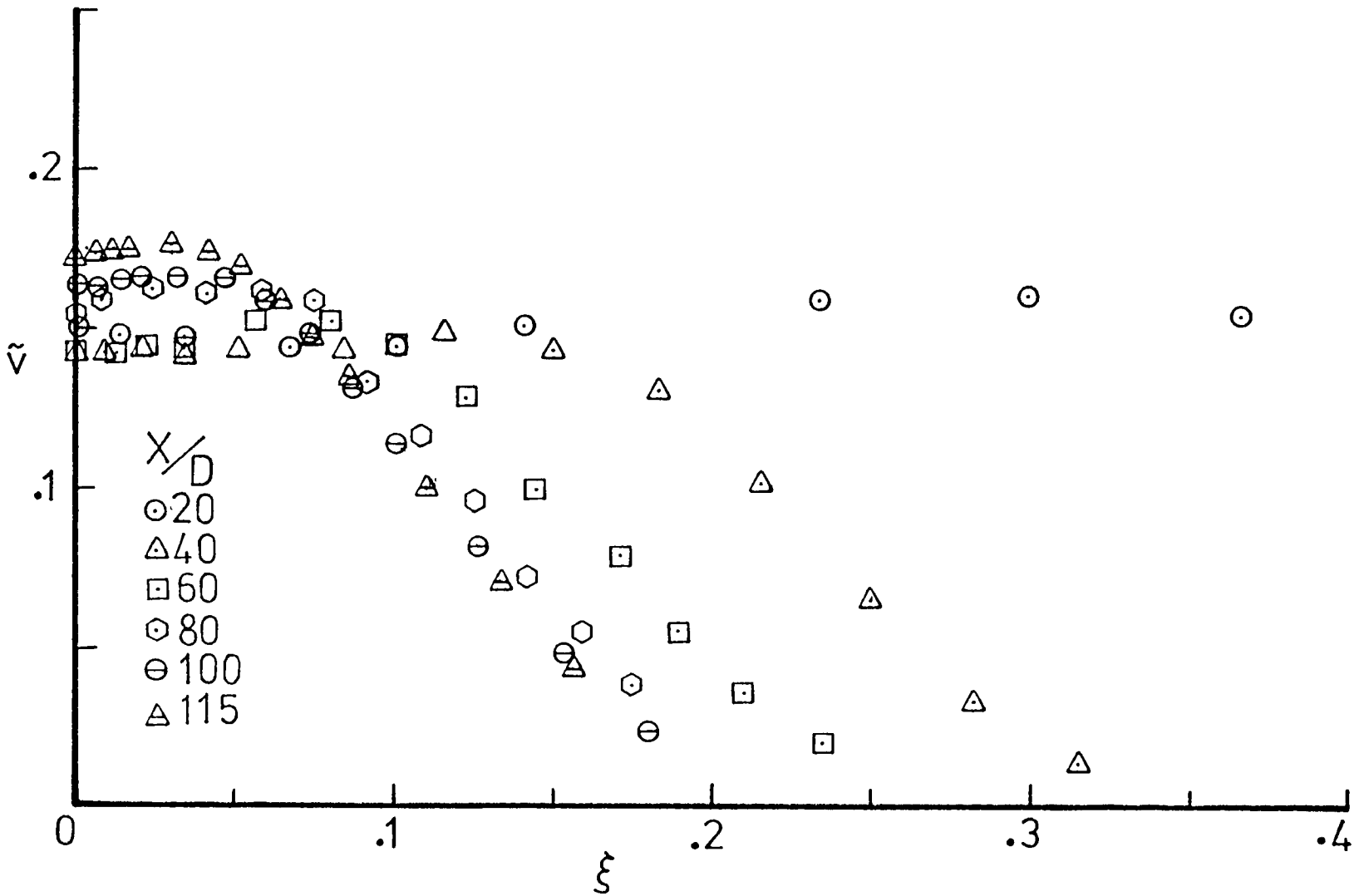

Figure 4.17 The distribution of the lateral velocity fluctuations in the x,z plane

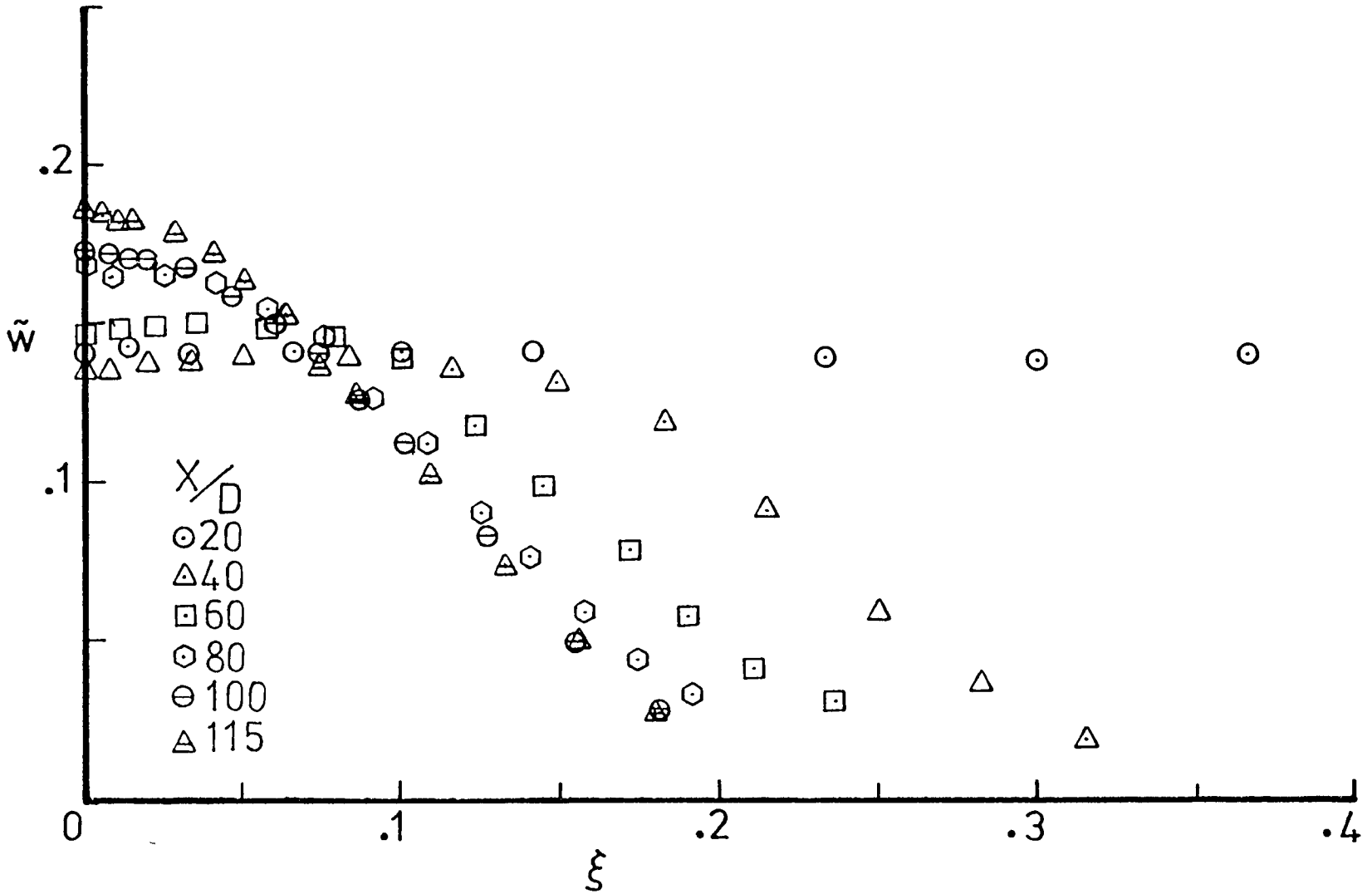

Figure 4.18 The distribution of the transverse velocity fluctuations in the x,z plane

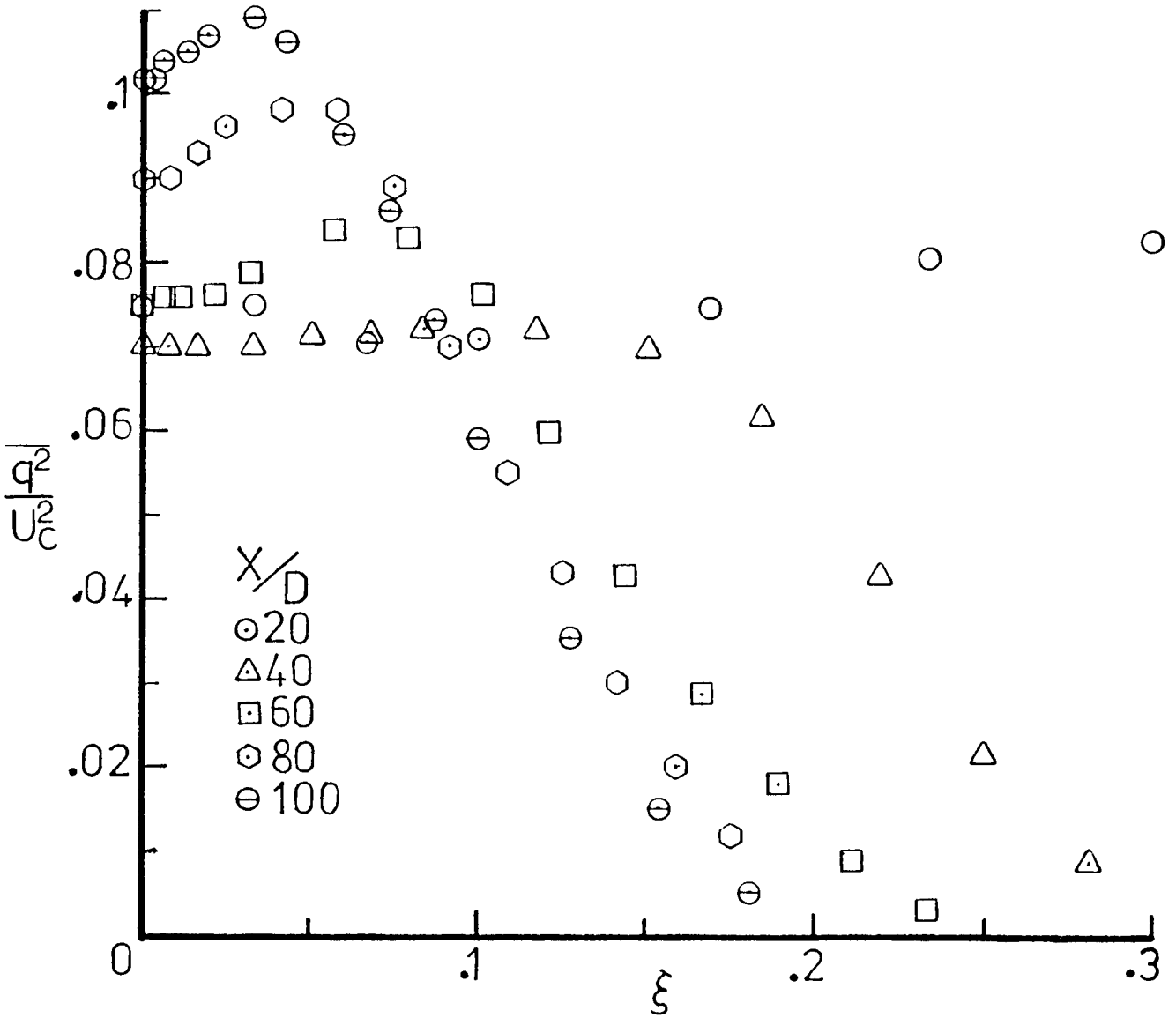

Figure 4.19 The distribution of the turbulent kinetic energy in the x,z plane

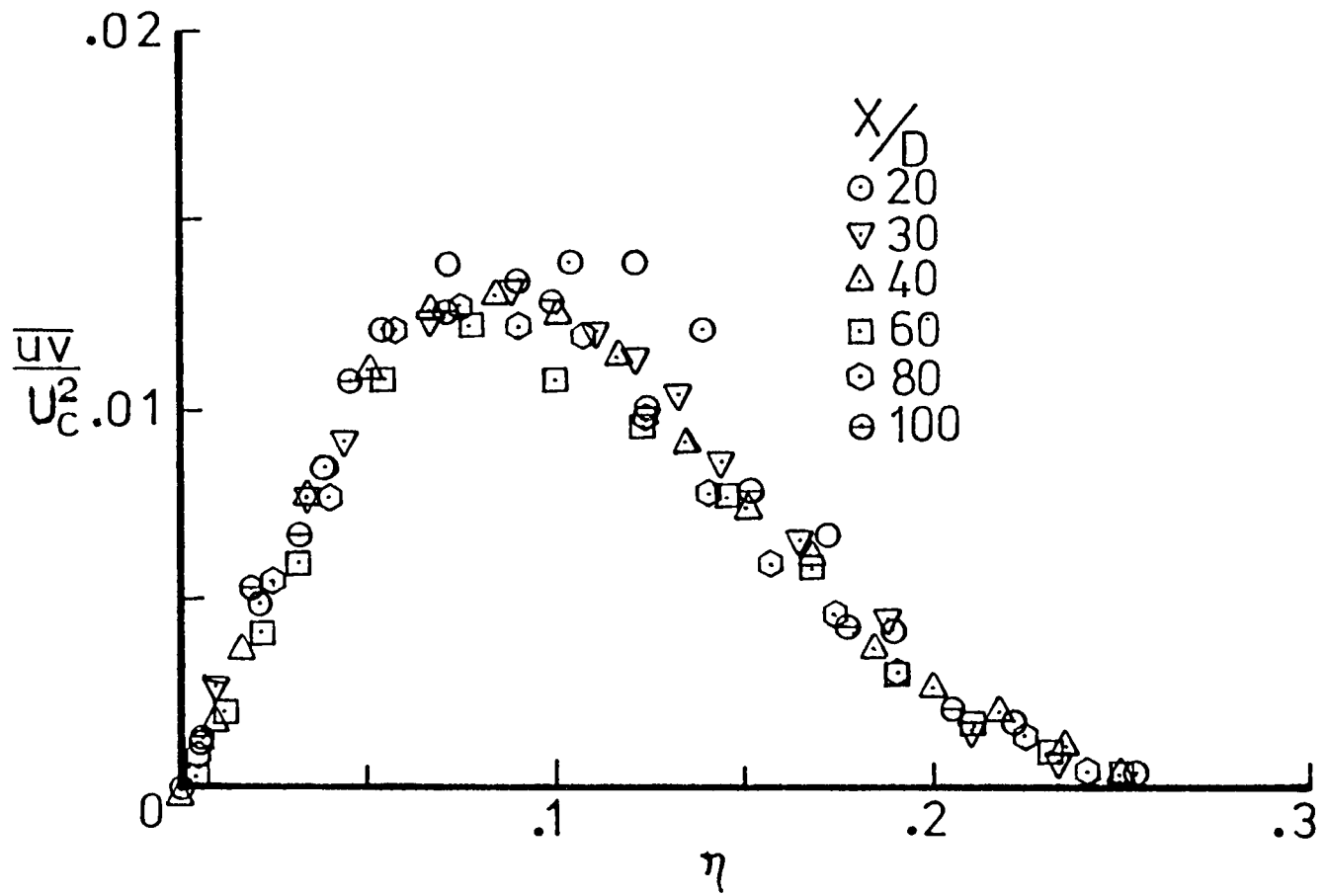

Figure 4.20 The distribution of the turbulent shear stress in the x,y plane

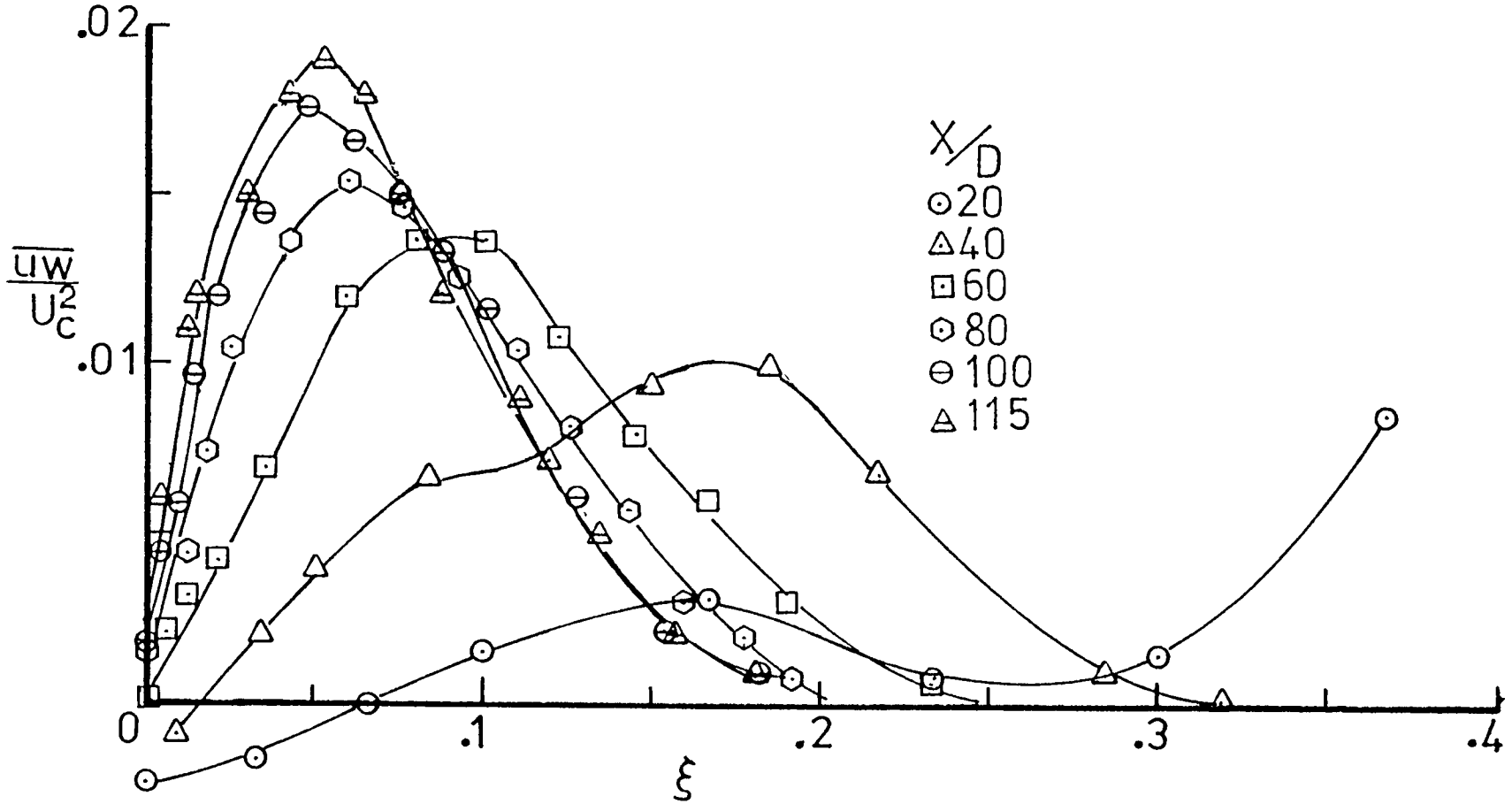

Figure 4.21 The distribution of the turbulent shear stress in the x,z plane

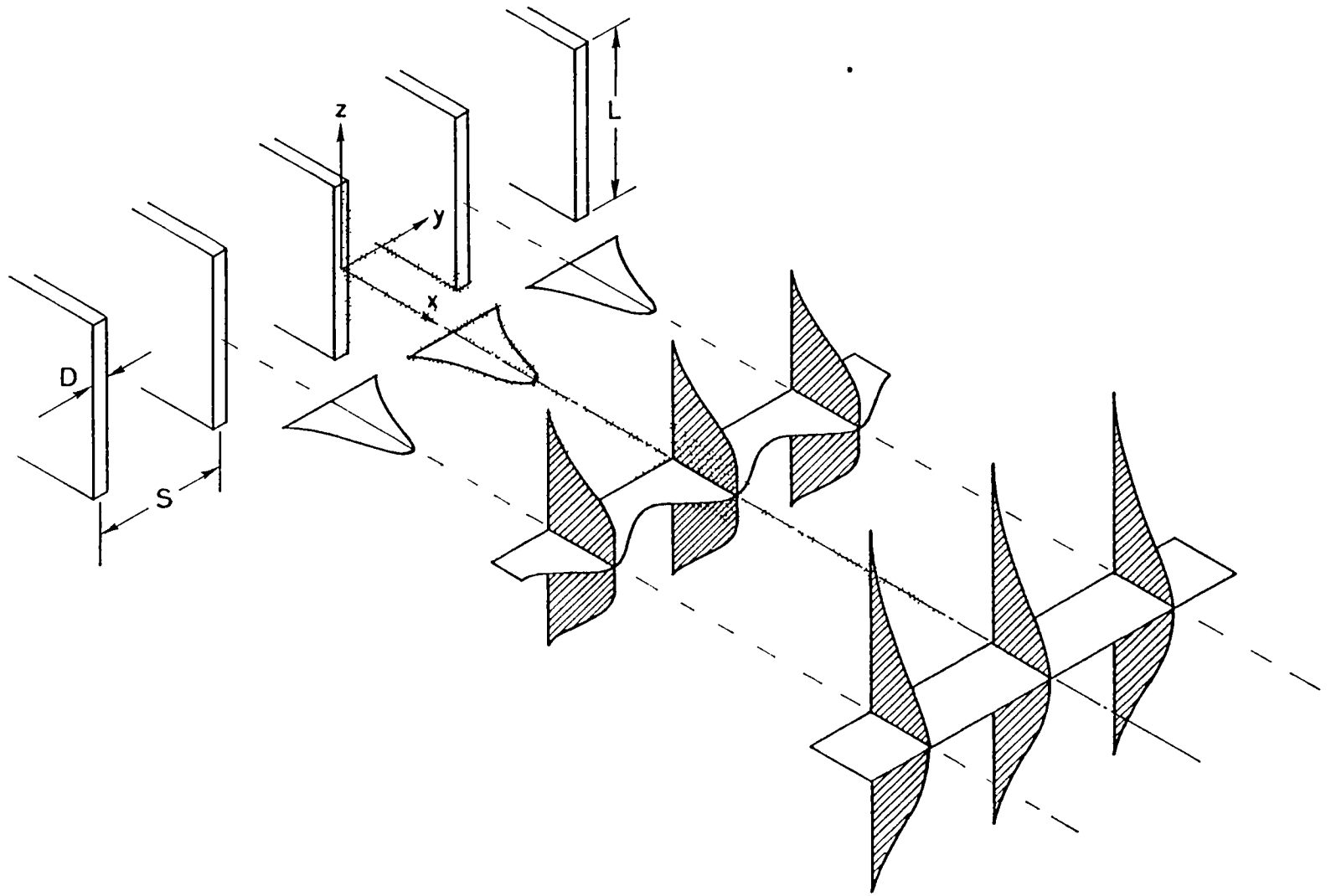

Figure 4.22 A schematic of the flow field of multiple free jets

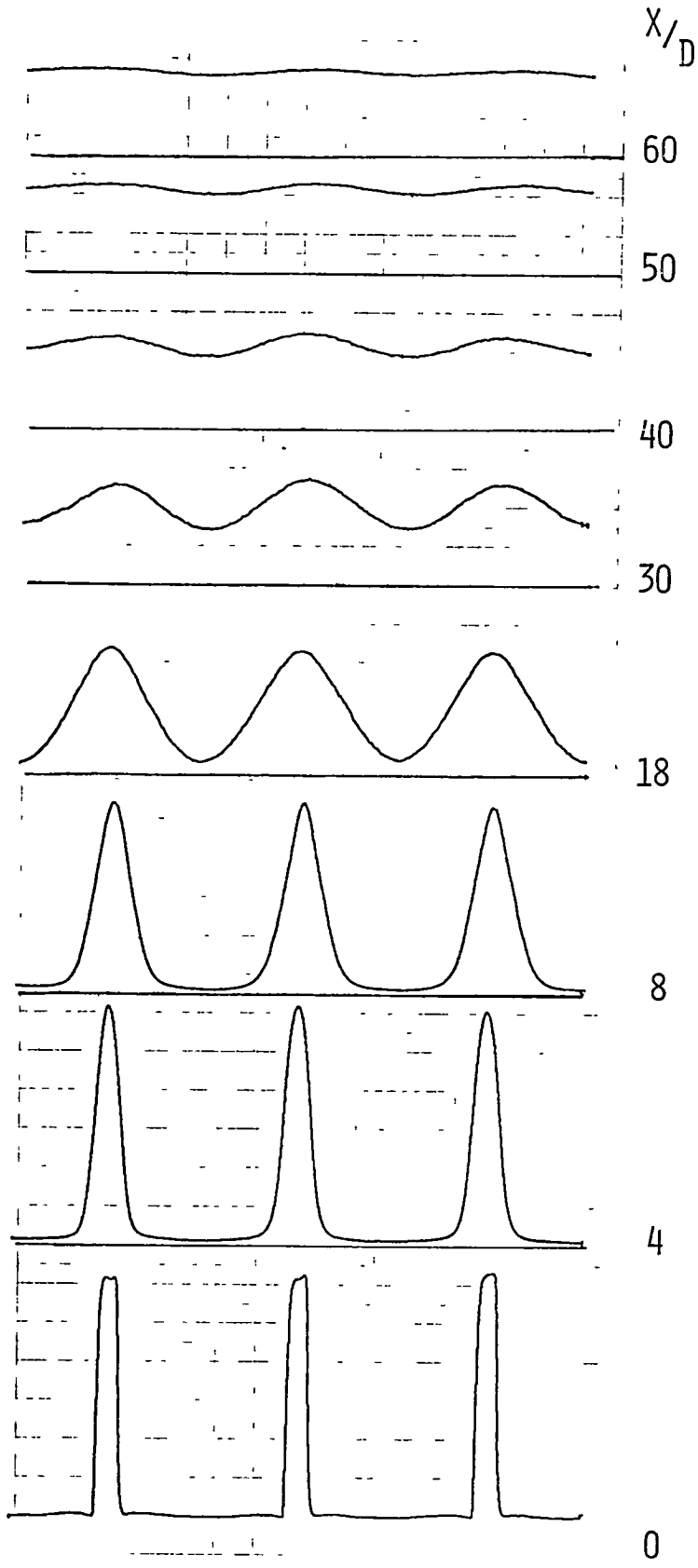

Figure 4.23 Axial mean velocity profiles across center three jets

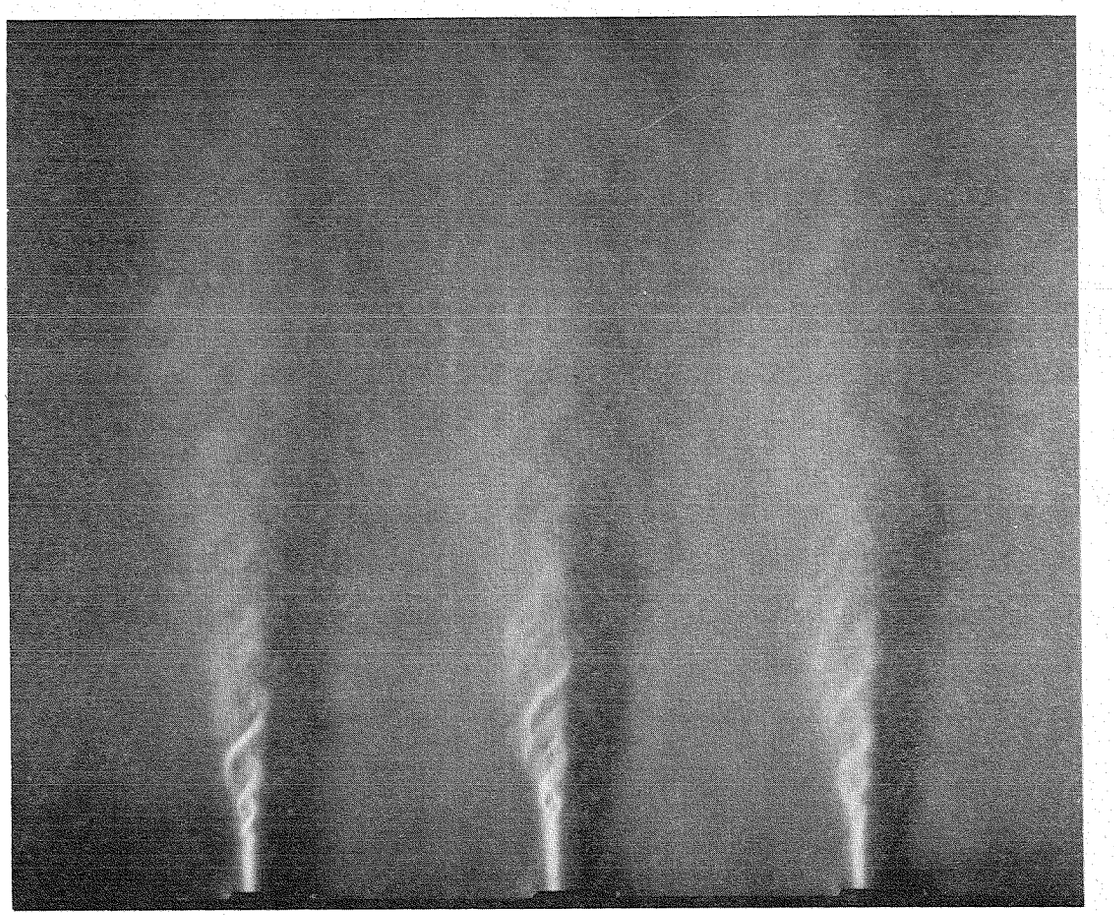

Figure 4.24 Schlieren picture of multiple jet flow field

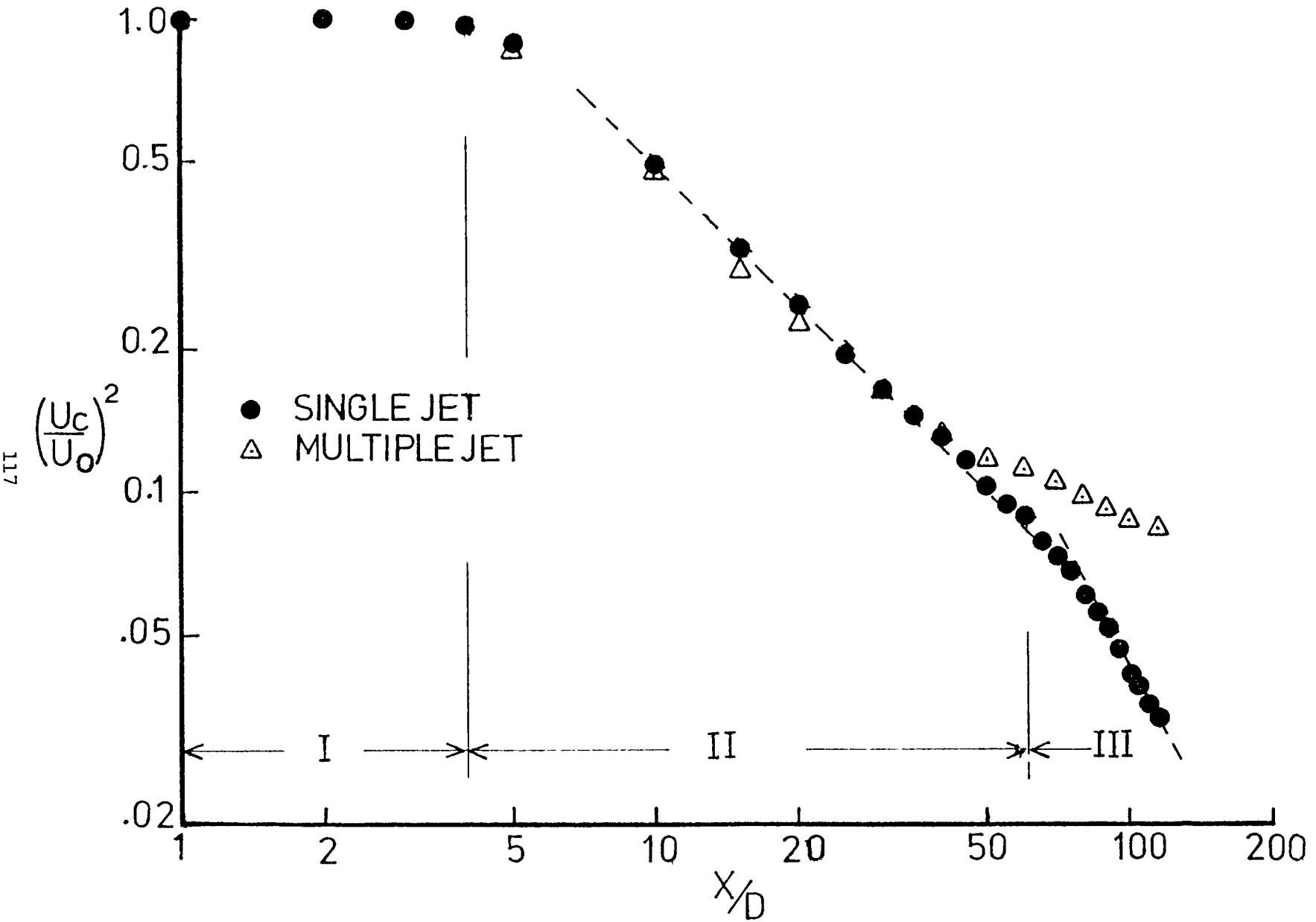

Figure 4.25 The decay of the axial mean velocity along the centerline of the jet

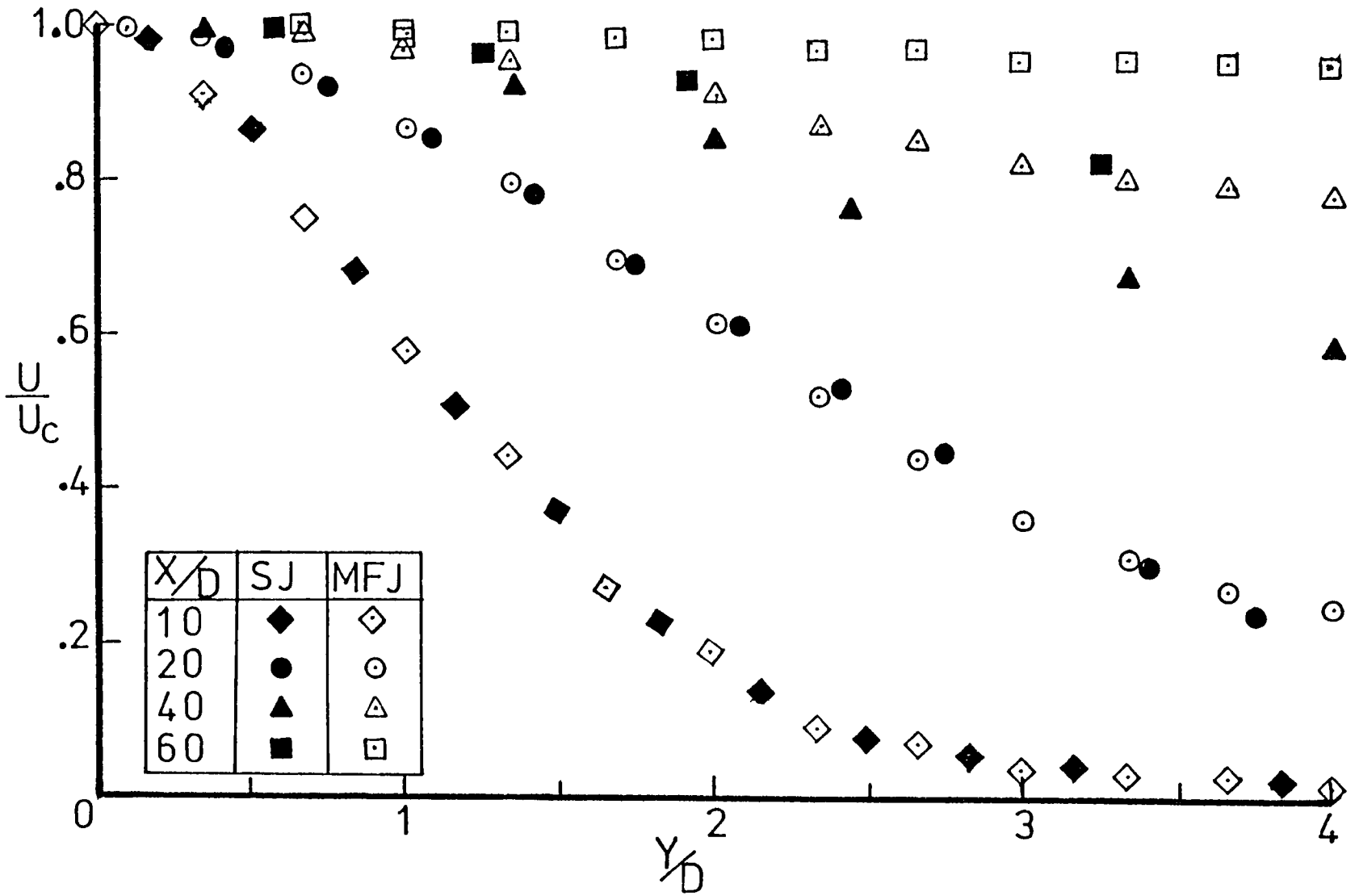

Figure 4.26 Axial mean velocity profiles in the x,y plane

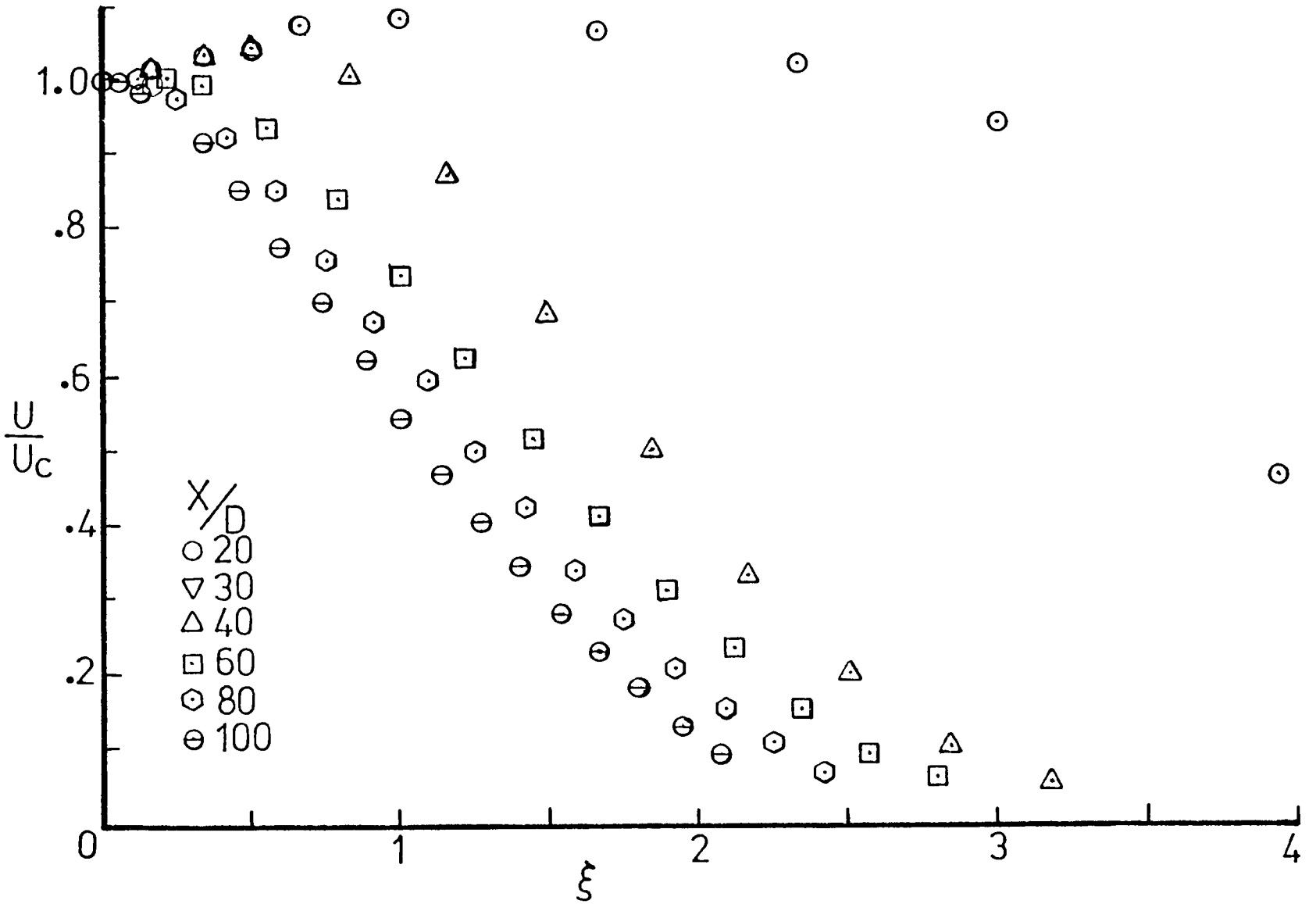

Figure 4.27 Axial mean velocity profiles in the x,z plane

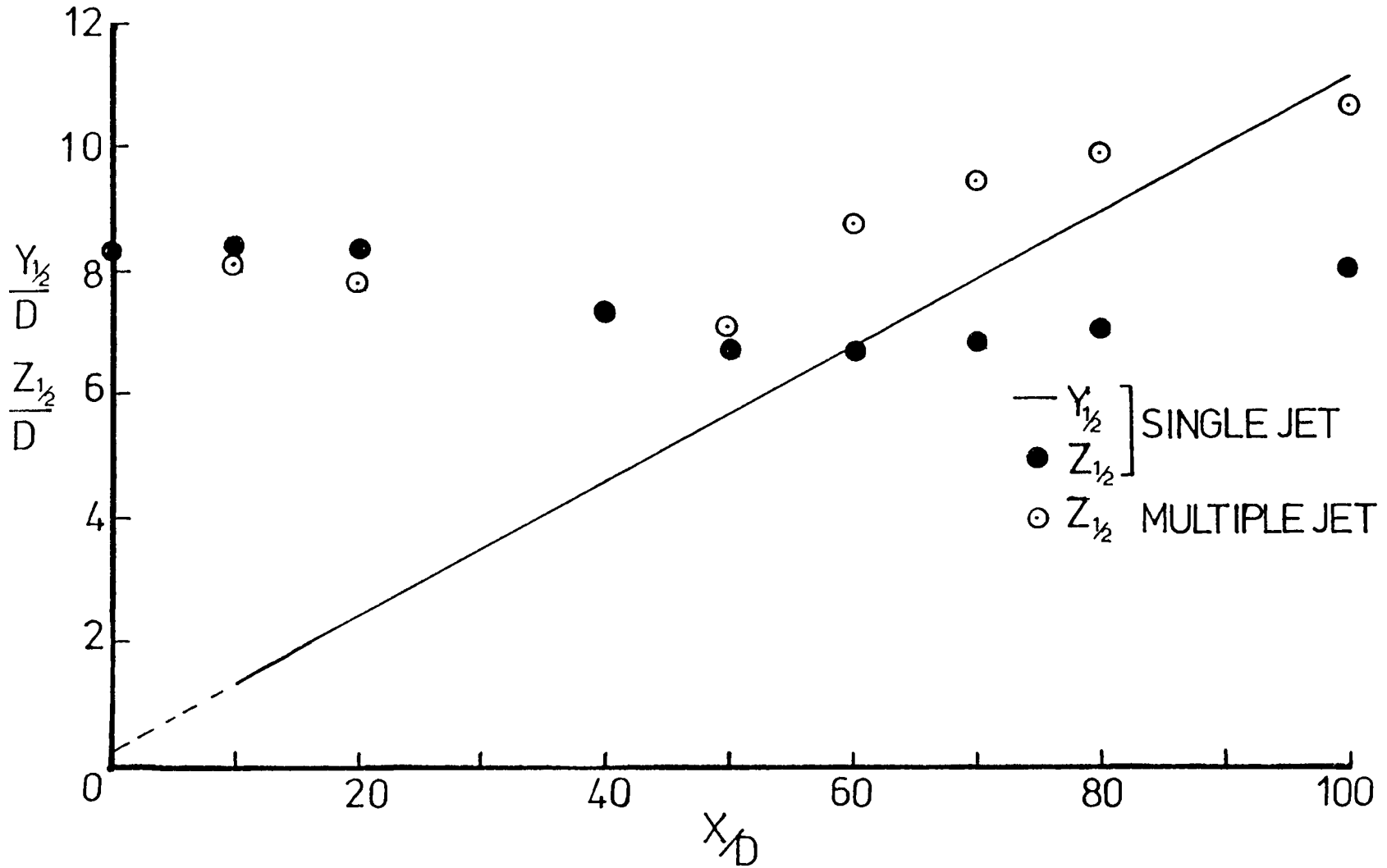

Figure 4.28 The growth of the jet with downstream distance

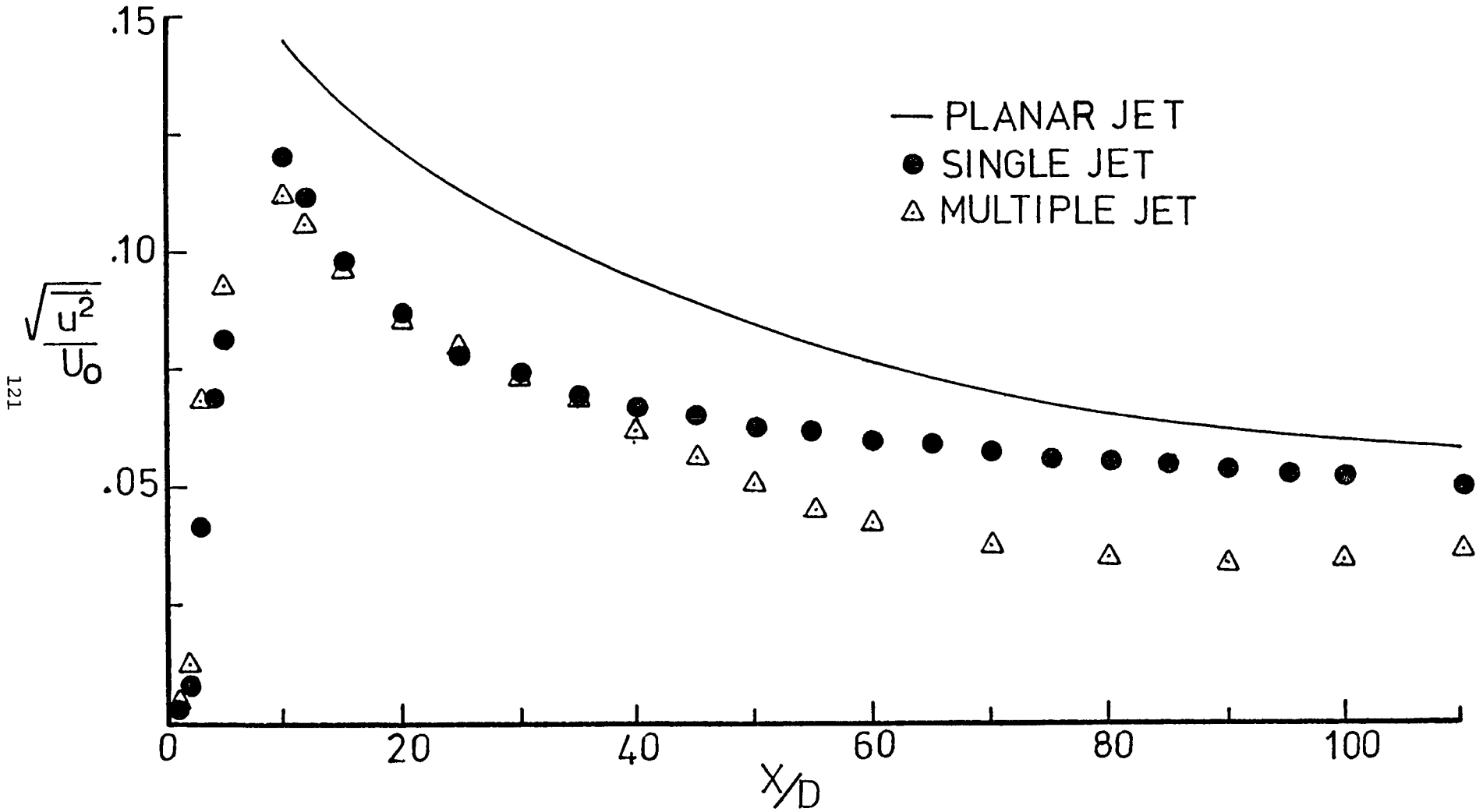

Figure 4.29 The variation of the rms value of the axial component of velocity along the centerline of the jet

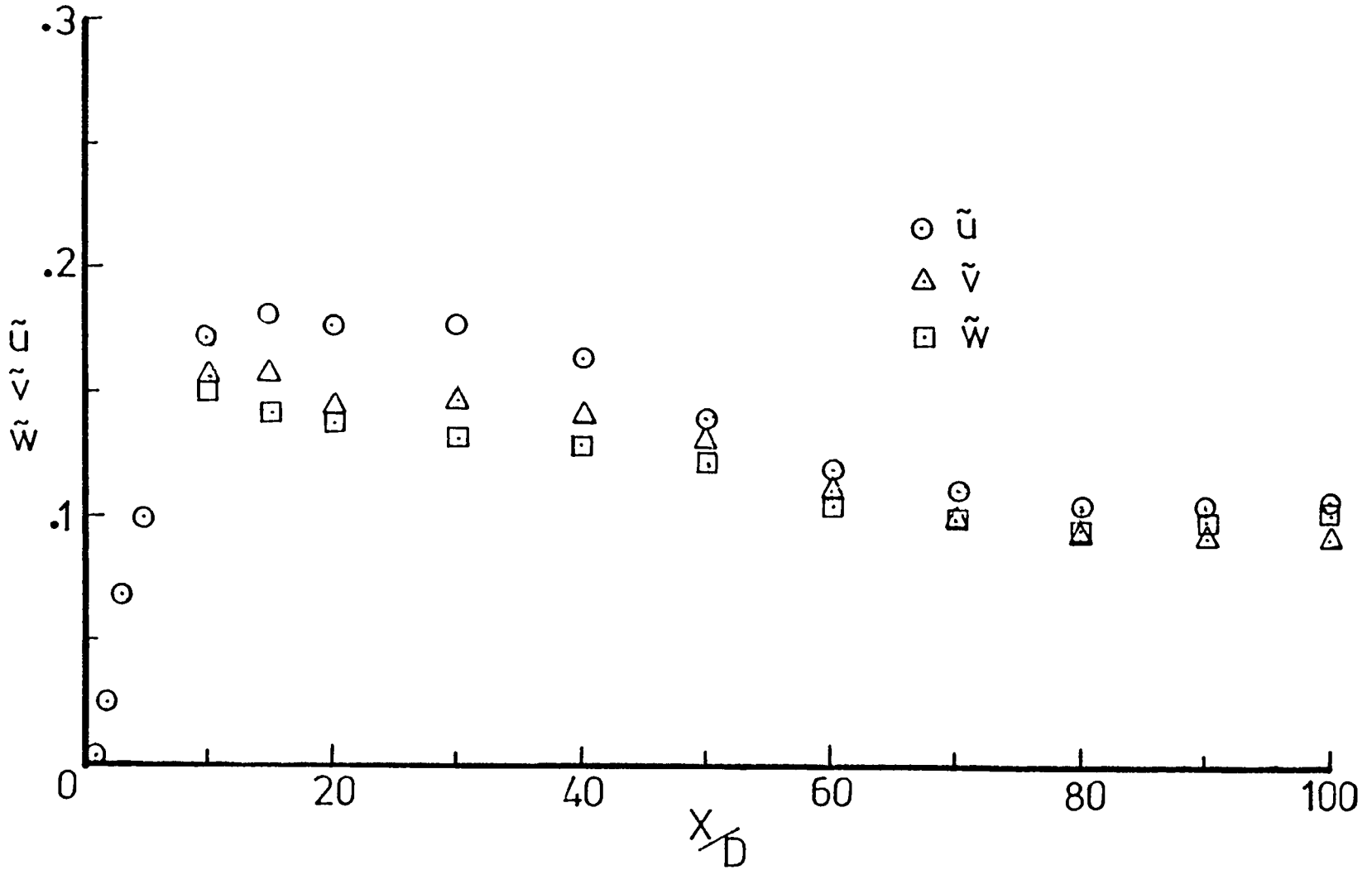

Figure 4.30 Variation of turbulent intensities along the centerline of the jet

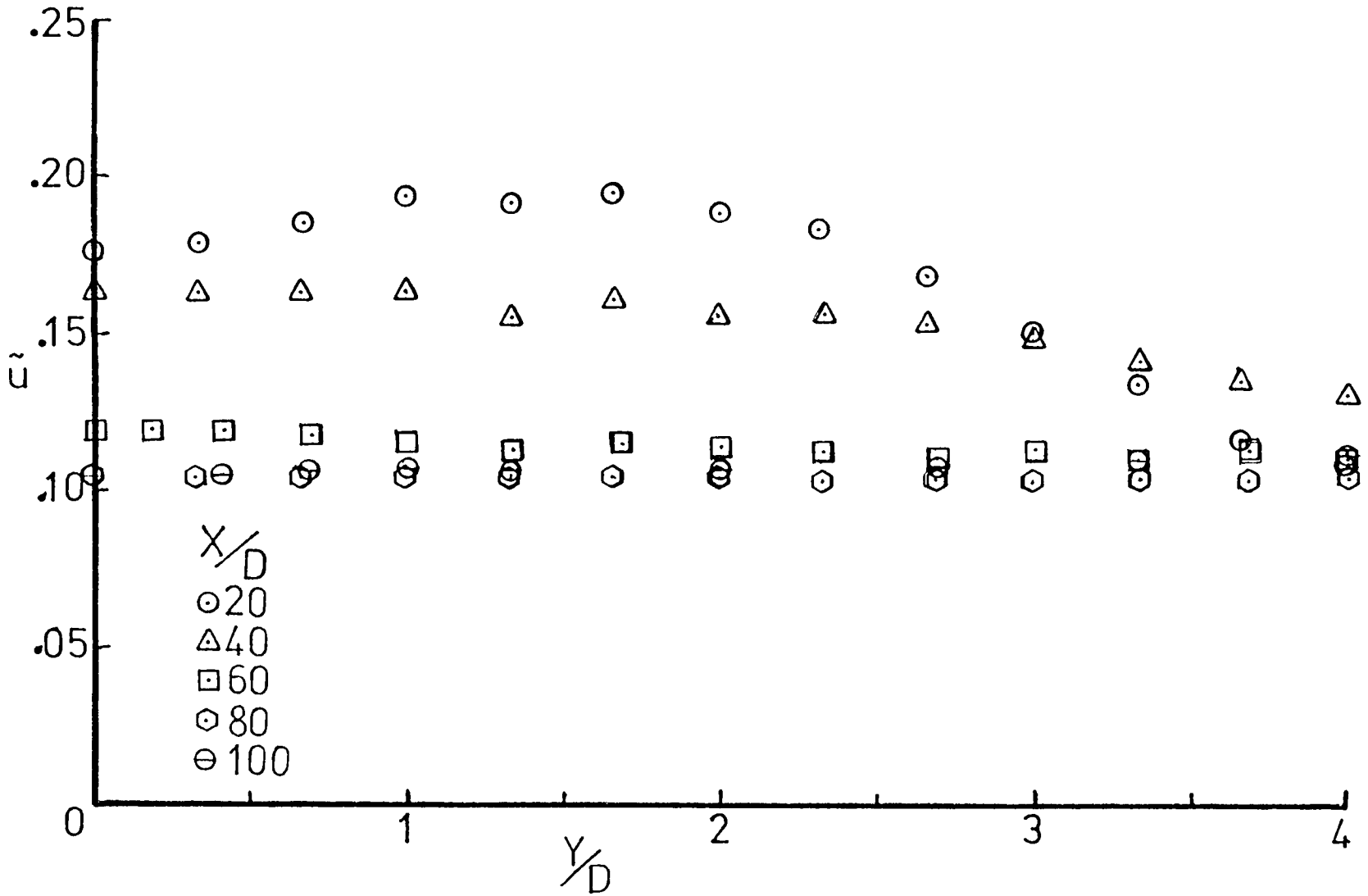

Figure 4.31 The distribution of the axial velocity fluctuations in the x,y plane

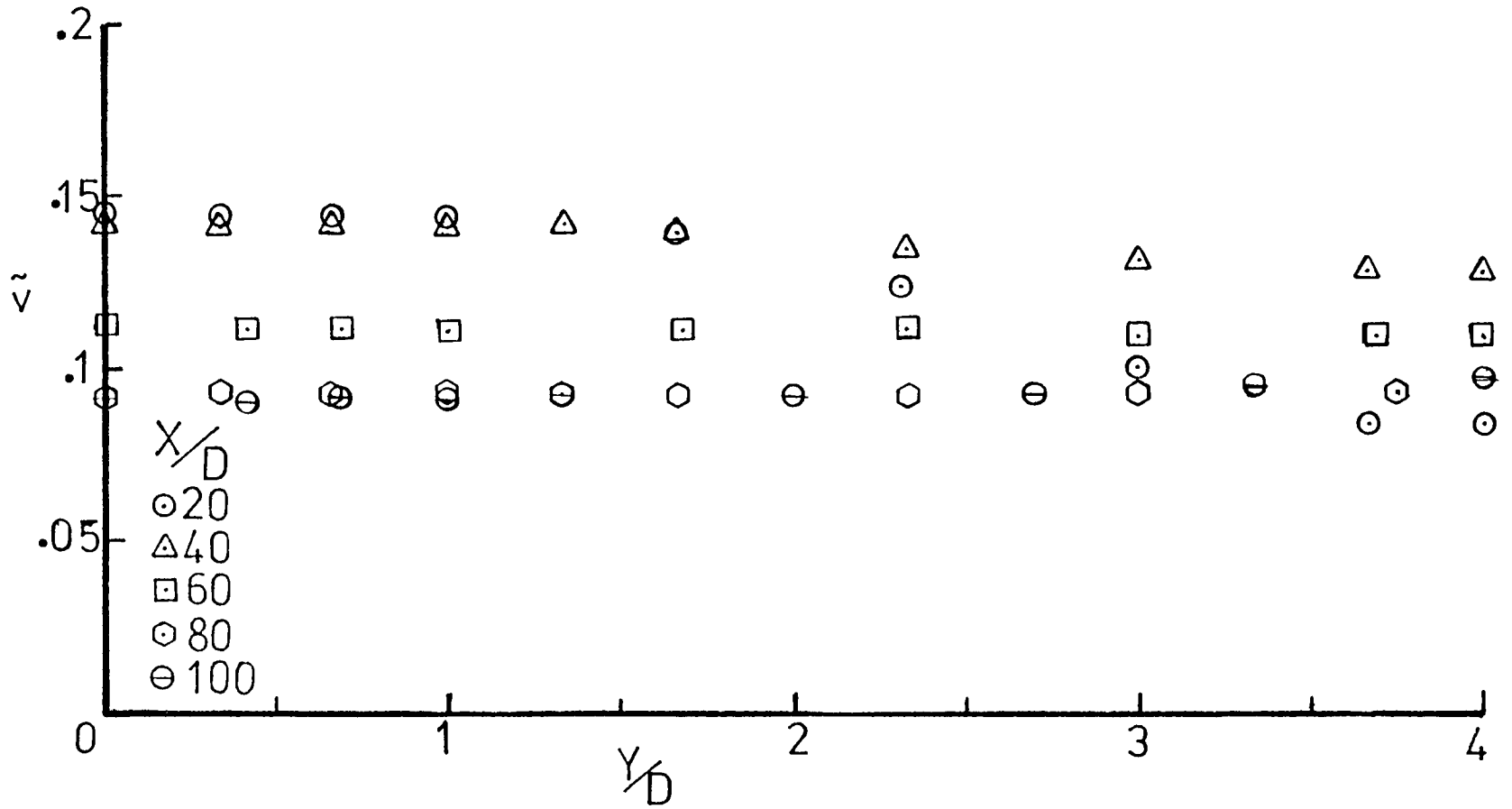

Figure 4.32 The distribution of the lateral velocity fluctuations in the x,y plane

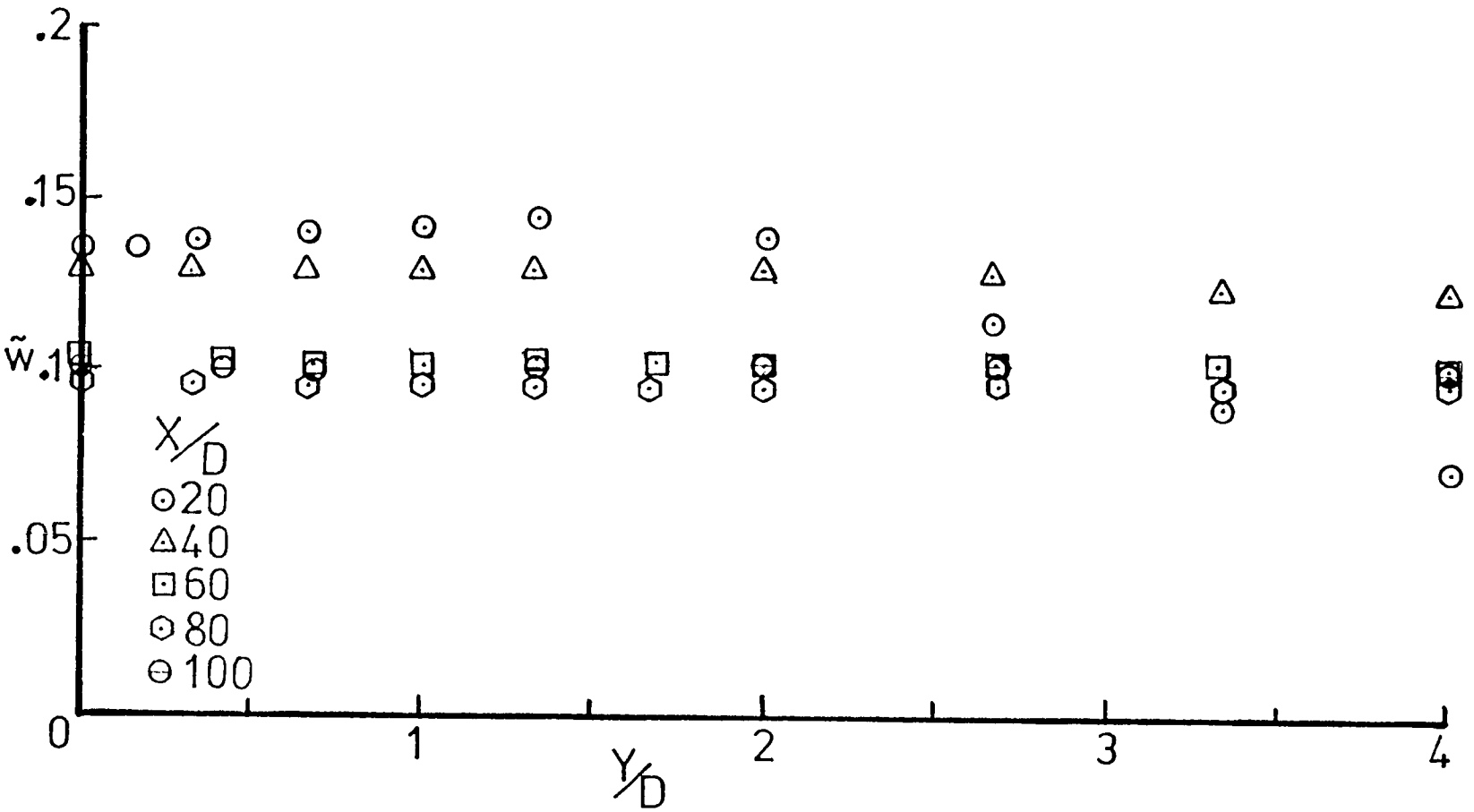

Figure 4.33 The distribution of the transverse velocity fluctuations in the x,y plane

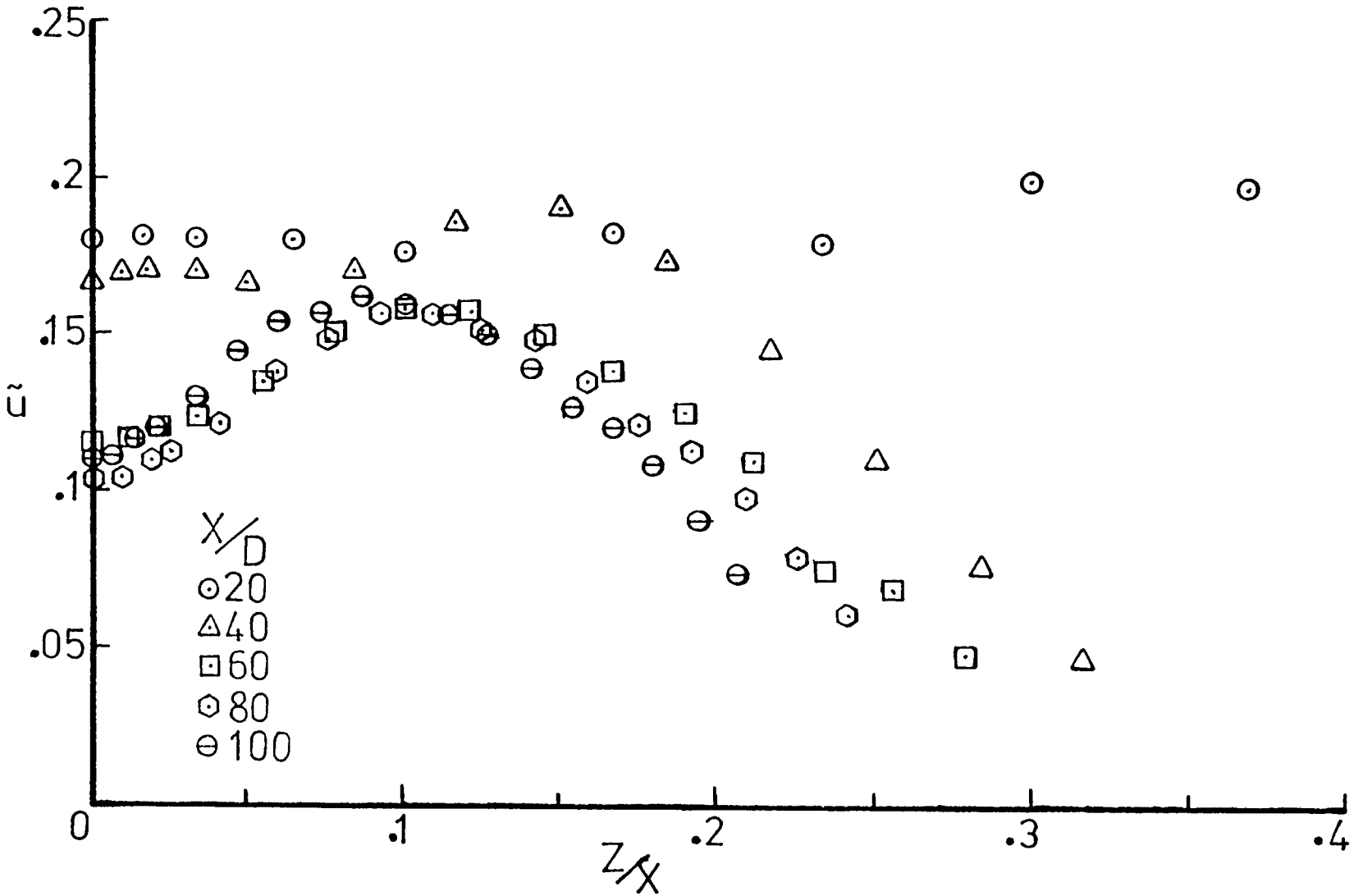

Figure 4.34 The distribution of the axial velocity fluctuations in the x,z plane

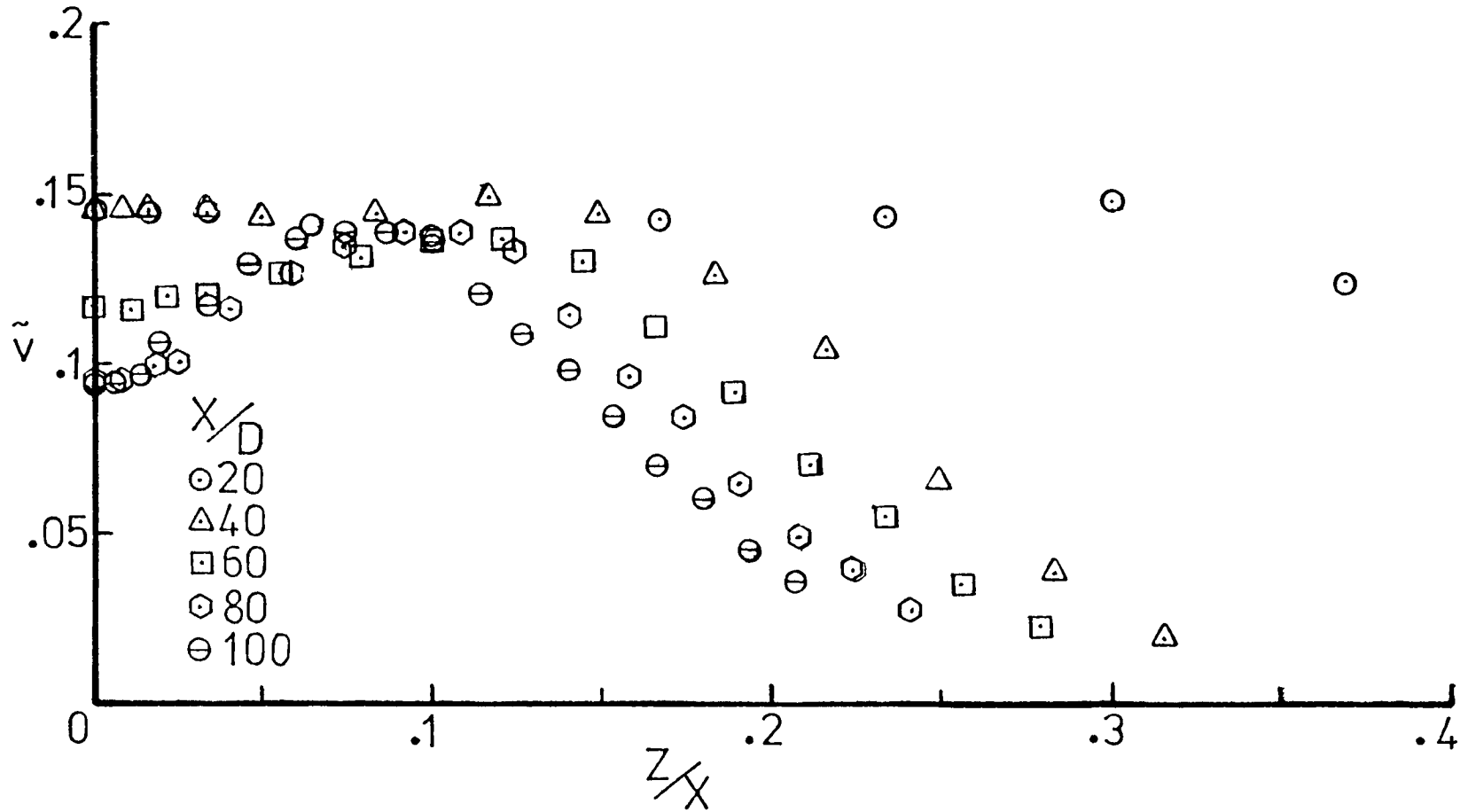

Figure 4.35 The distribution of the lateral velocity fluctuations in the x,z plane

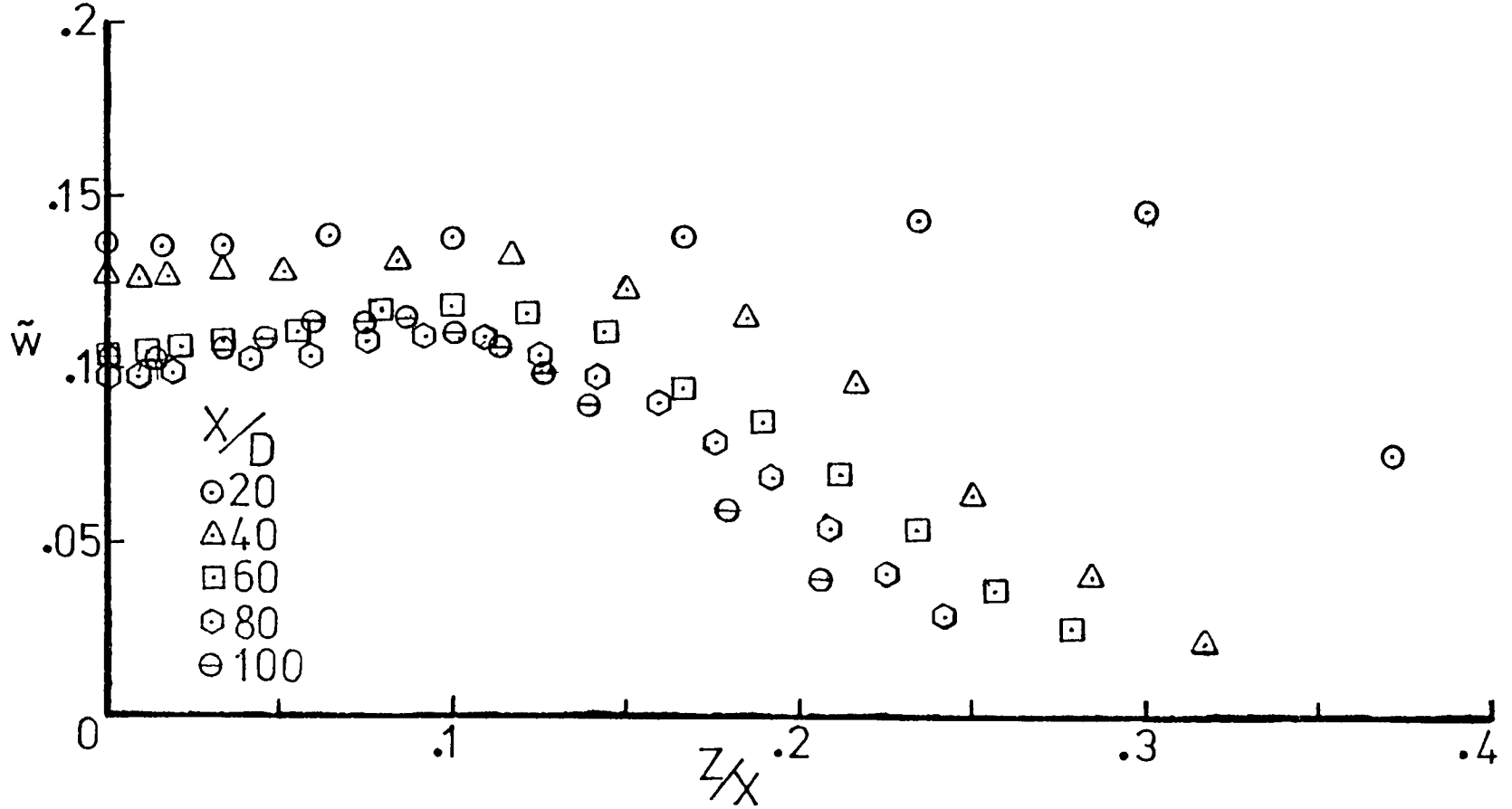

Figure 4.36 The distribution of the transverse velocity fluctuations in the x,z plane

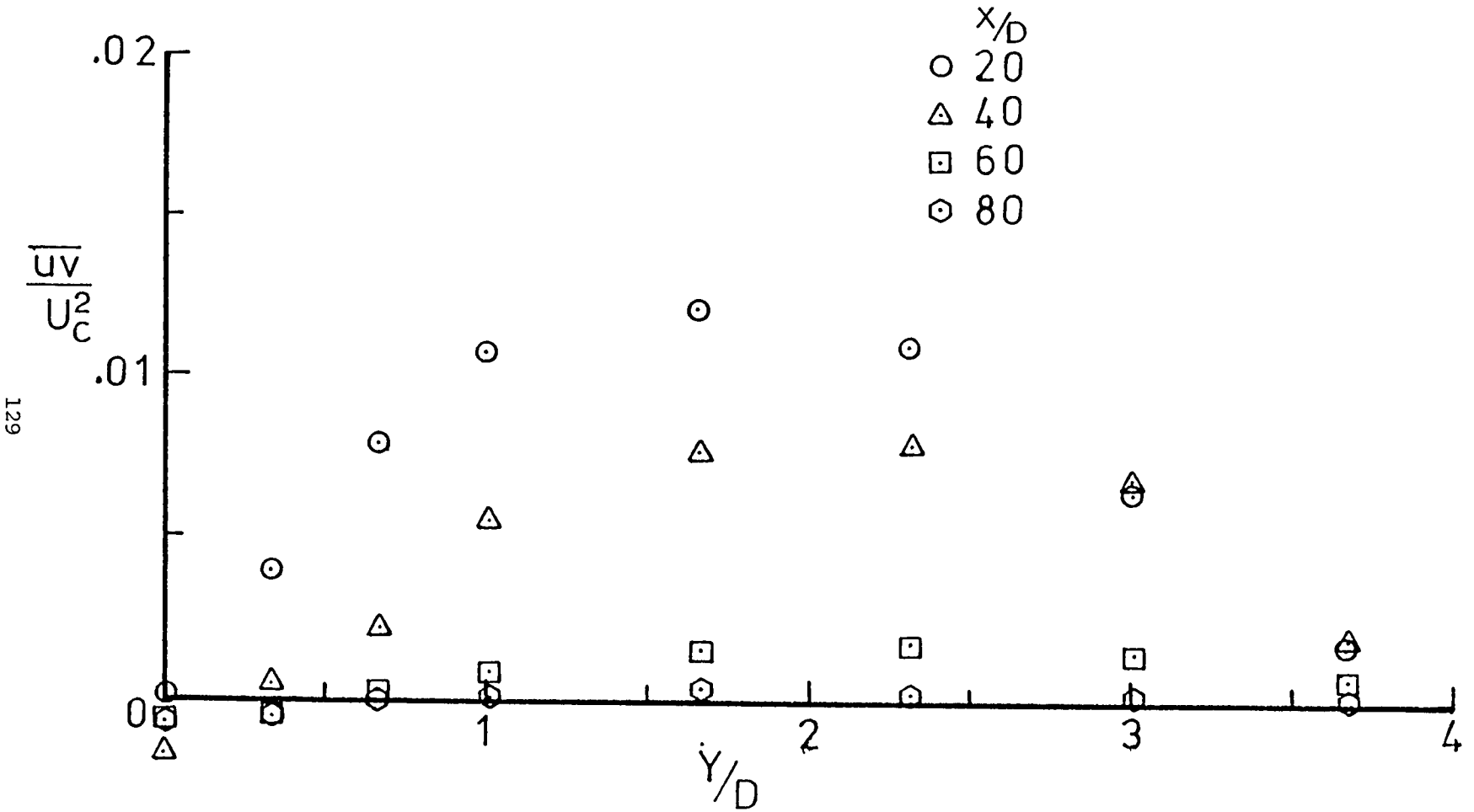

Figure 4.37 The distribution of the turbulent shear stress in the x,y plane

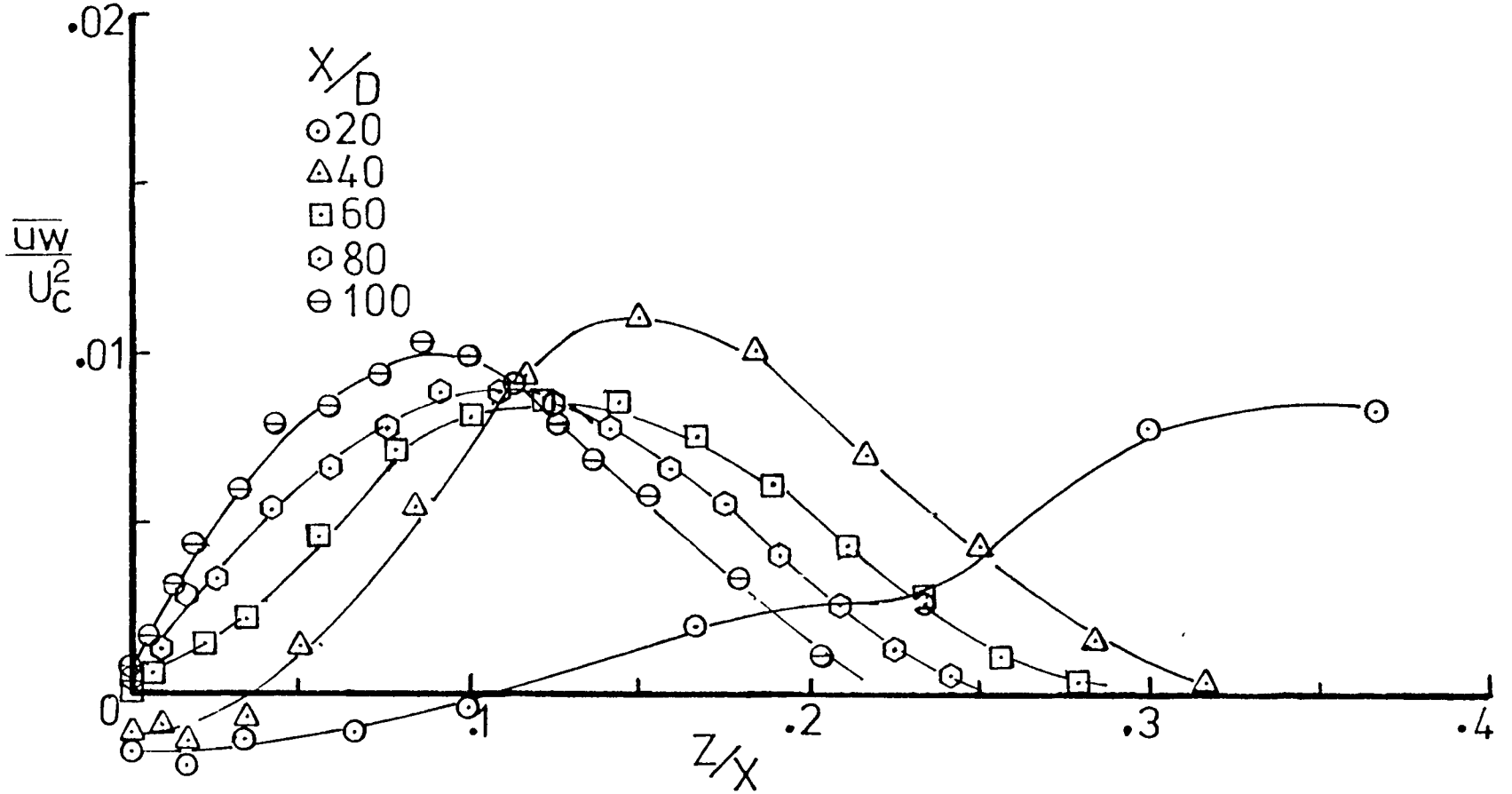

Figure 4.38 The distribution of the turbulent shear stress in the x,z plane

Figure 4.39 Schematic arrangement of an ejector configuration

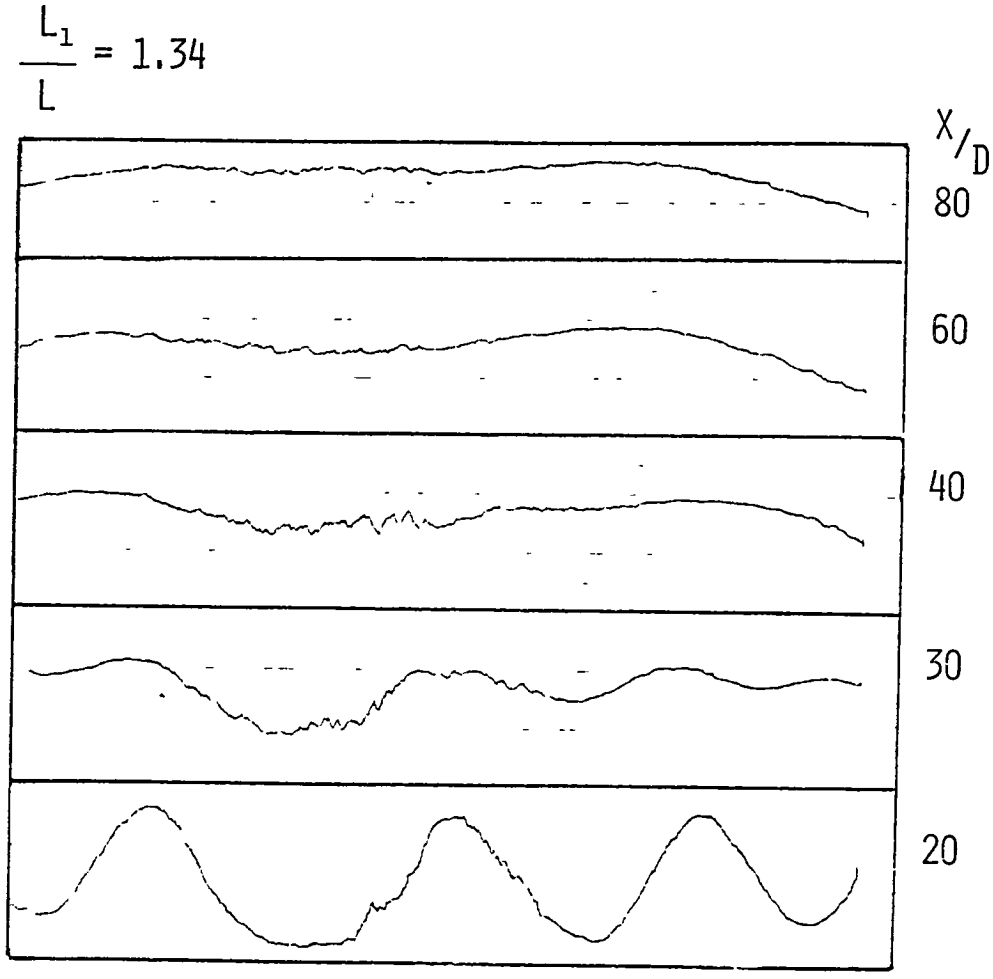

Figure 4.40 Axial mean velocity profiles in the x,y plane

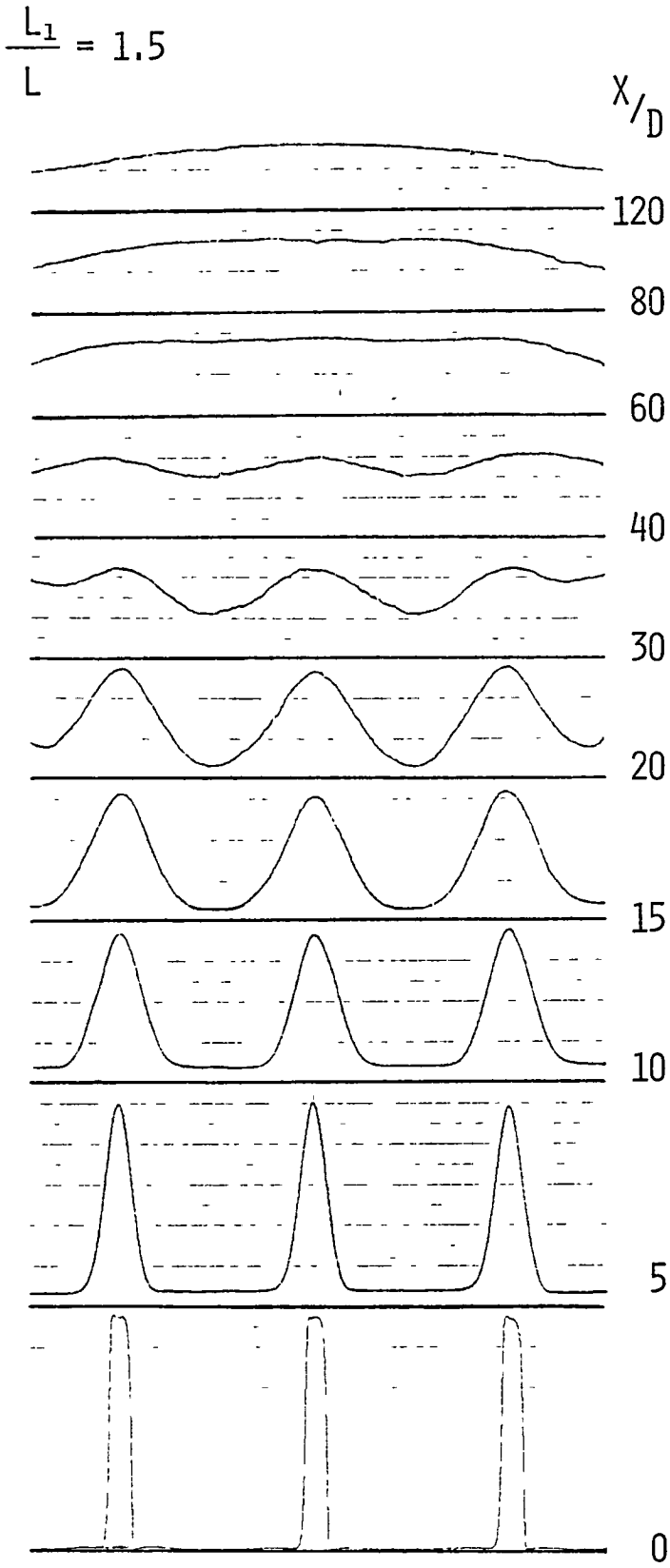

Figure 4.41 Axial mean velocity profiles in the x,y plane

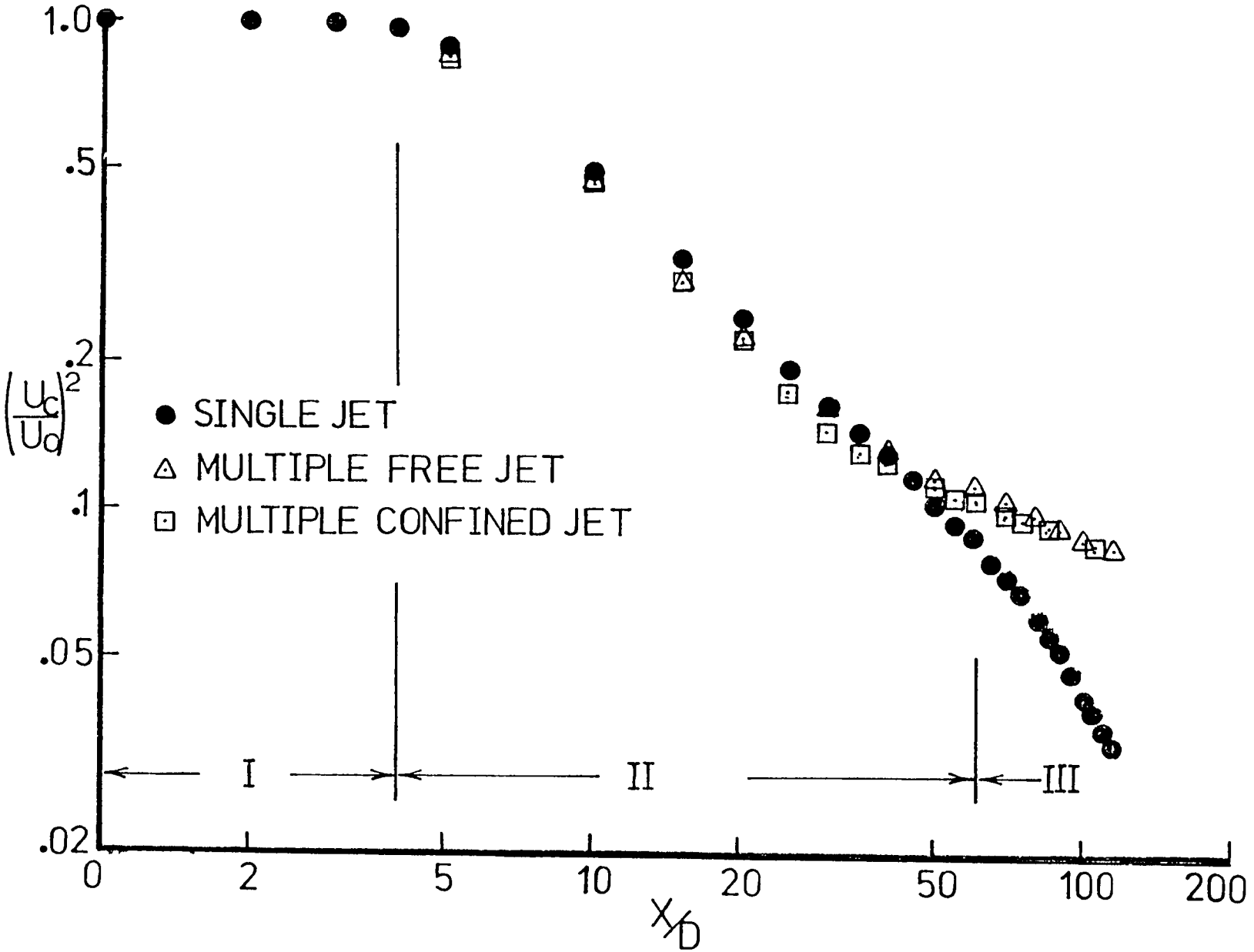

Figure 4.42 The decay of the axial mean velocity along the centerline of the jet

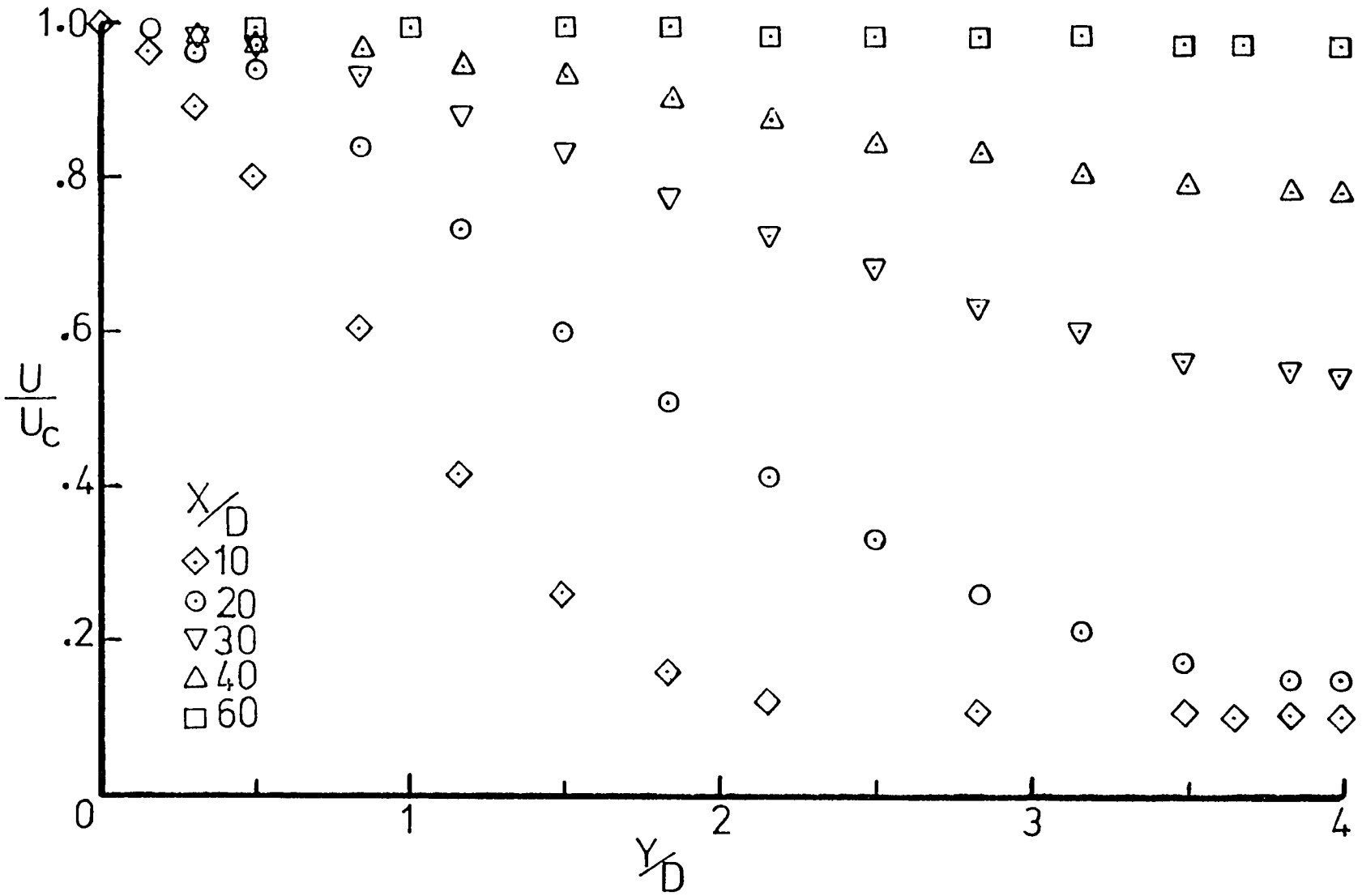

Figure 4.43 Axial mean velocity profiles in the x,y plane

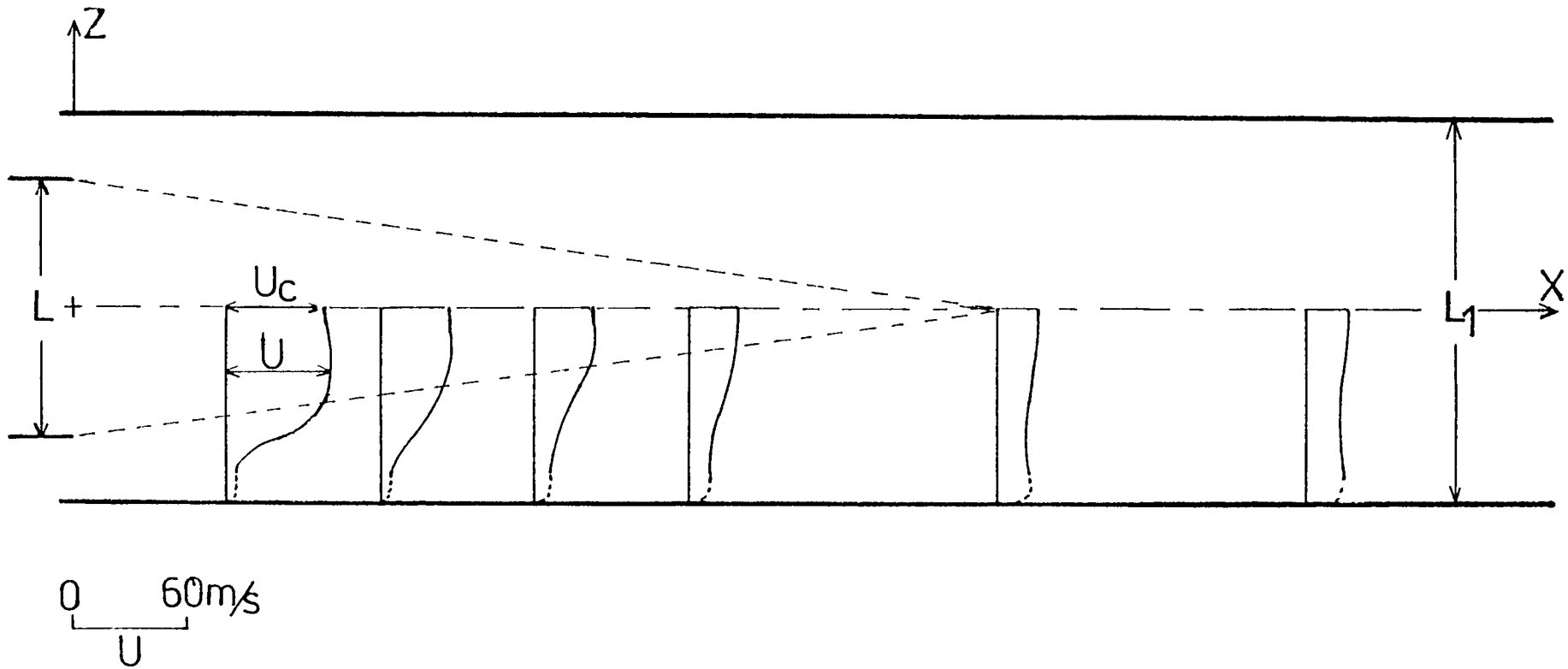

Figure 4.44 A schematic of axial mean velocity profiles in the x,z plane

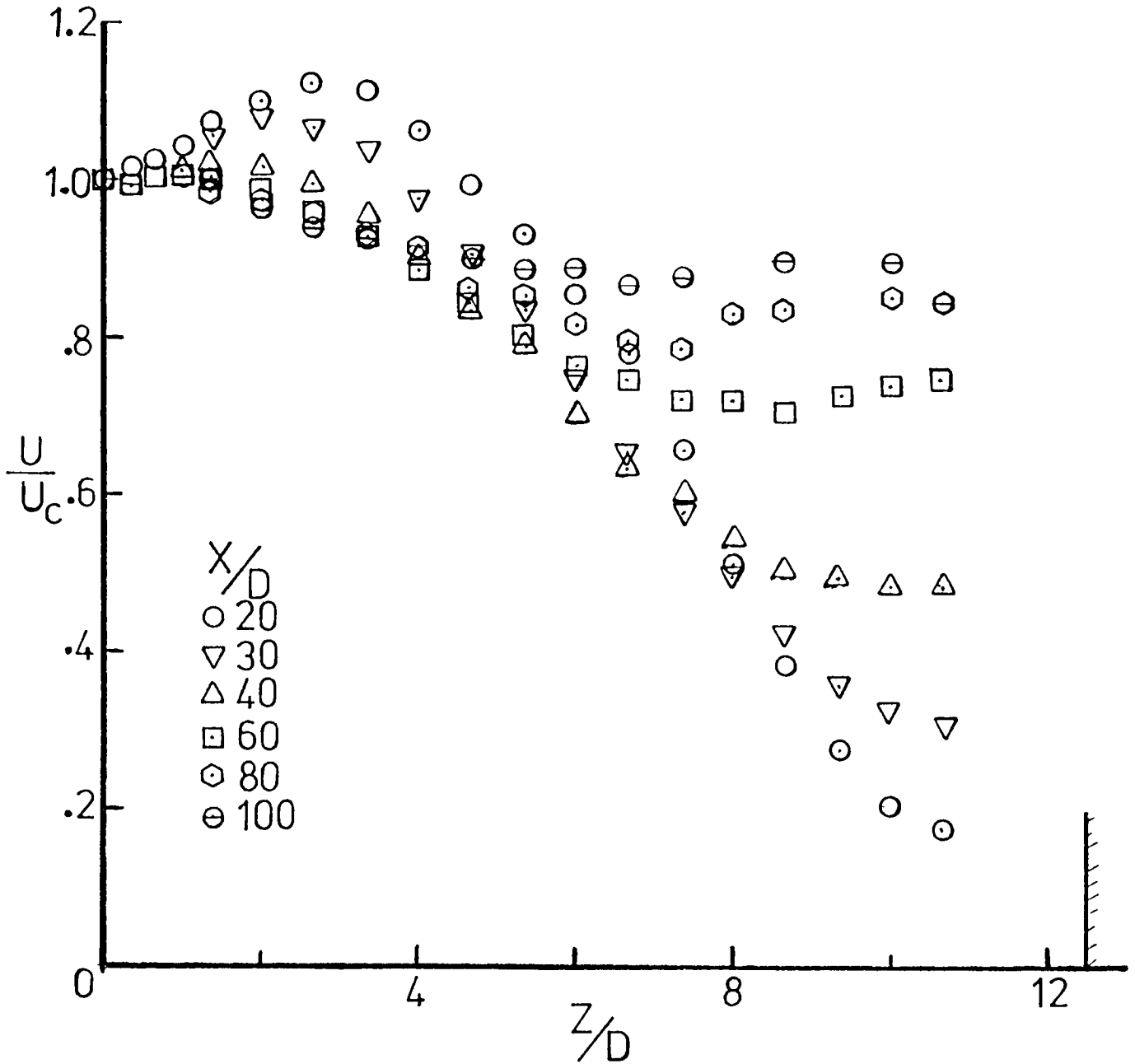

Figure 4.45 Axial mean velocity profiles in the x,z plane

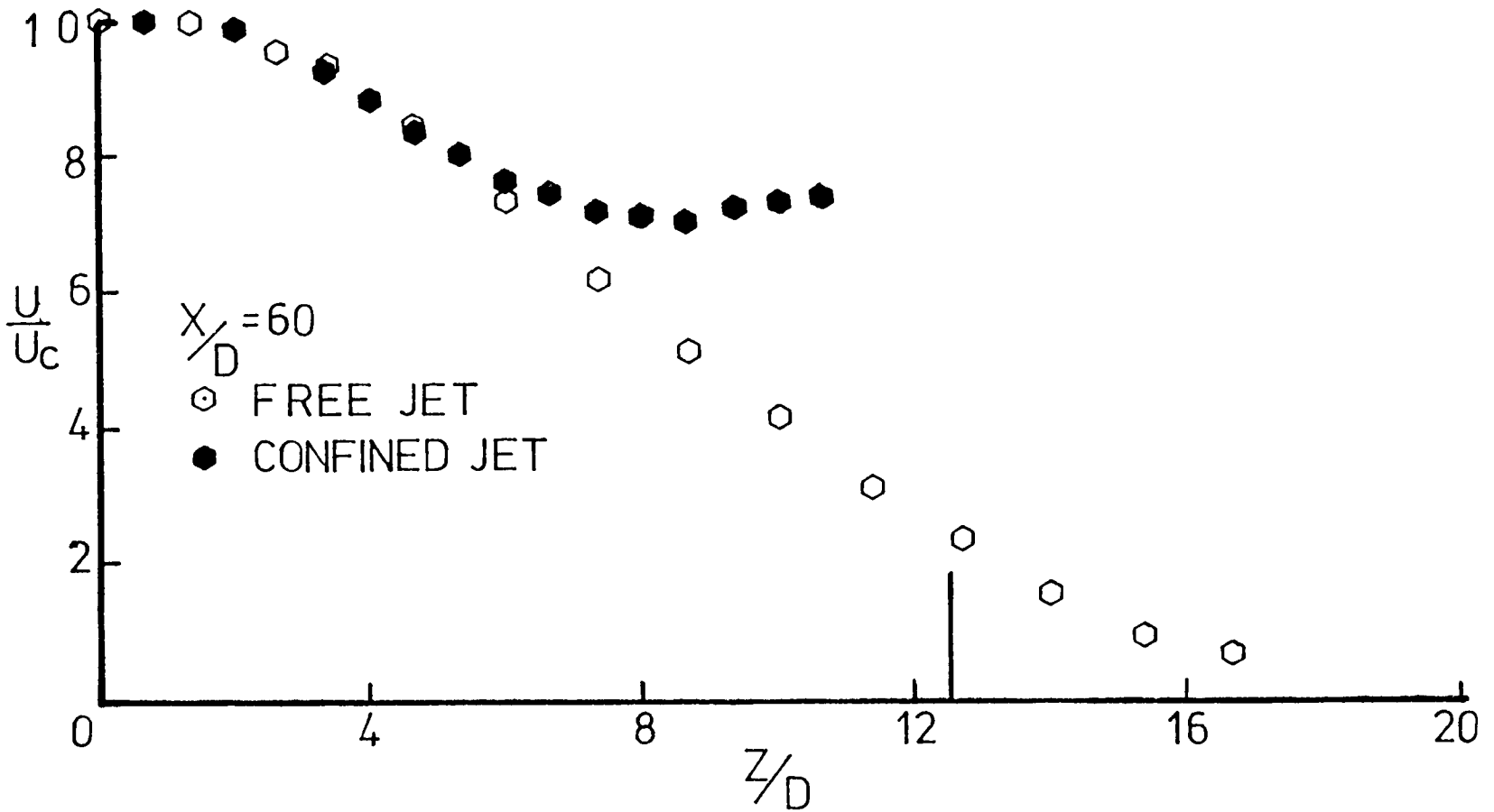

Figure 4.46 A comparison of the mean velocity profiles in the x,z plane

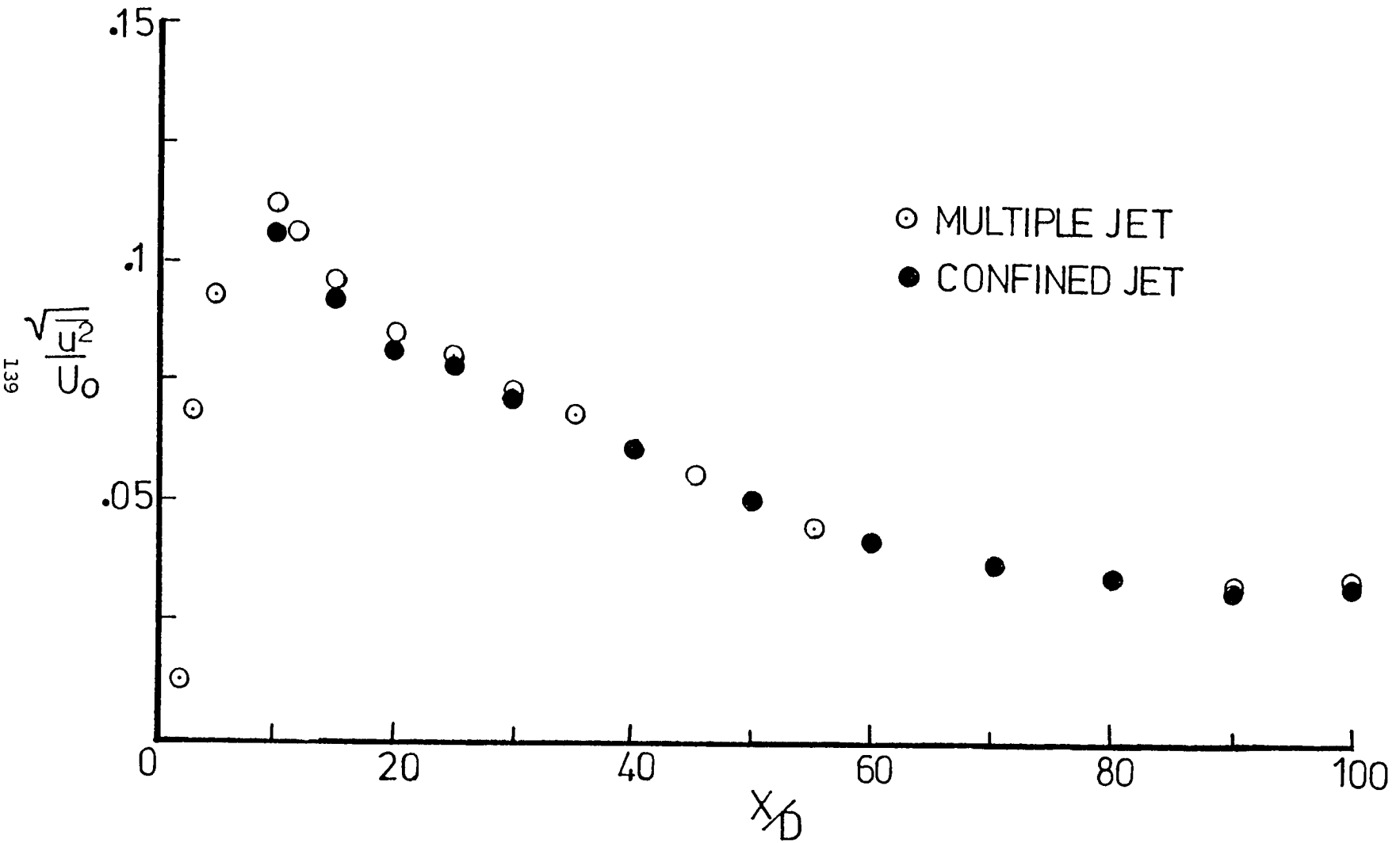

Figure 4.47 The variation of rms value of the u fluctuation along the centerline of the jet

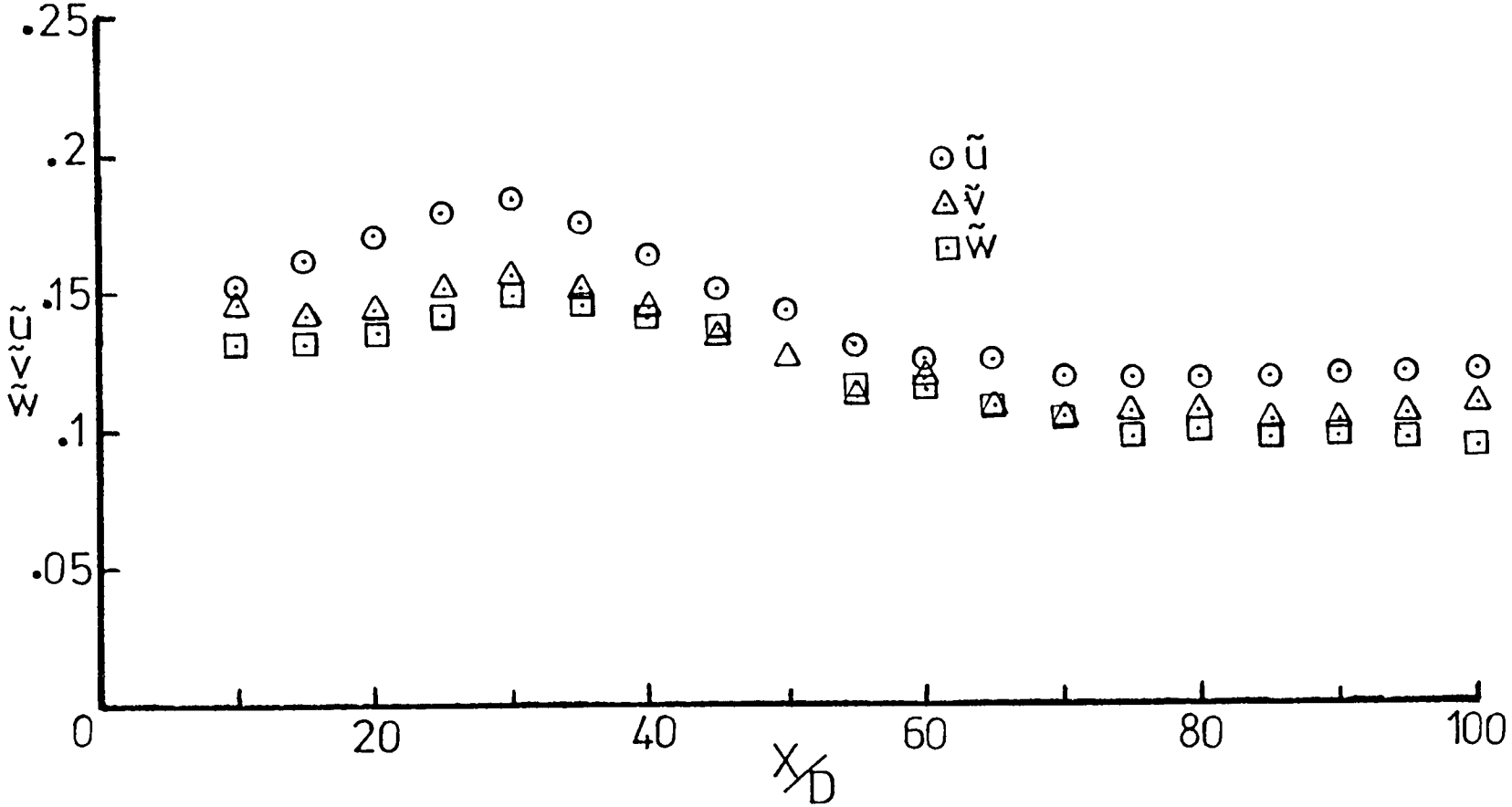

Figure 4.48 Variation of turbulent intensities along the centerline of the jet

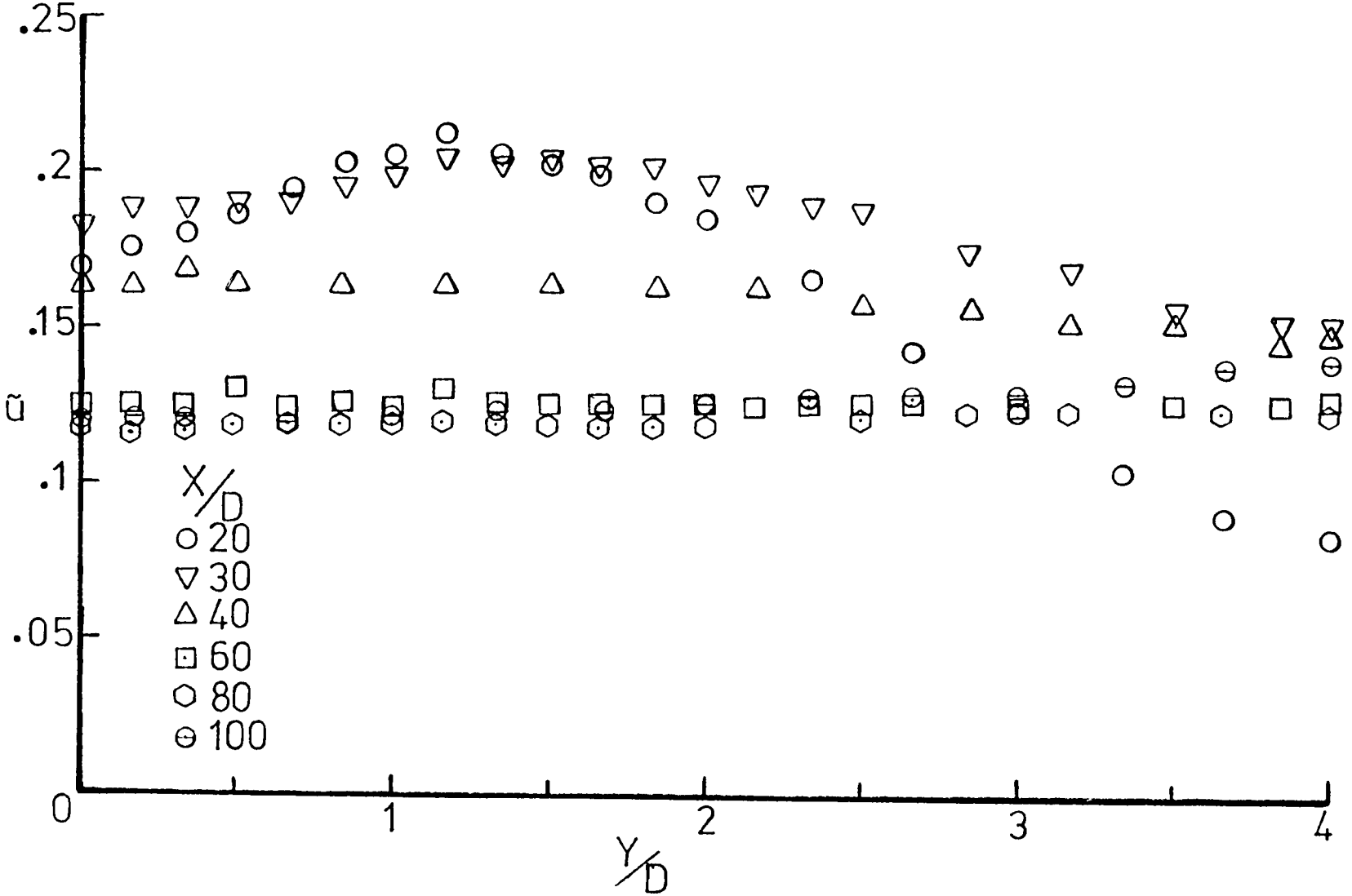

Figure 4.49 The distribution of the axial velocity fluctuations in the x,y plane

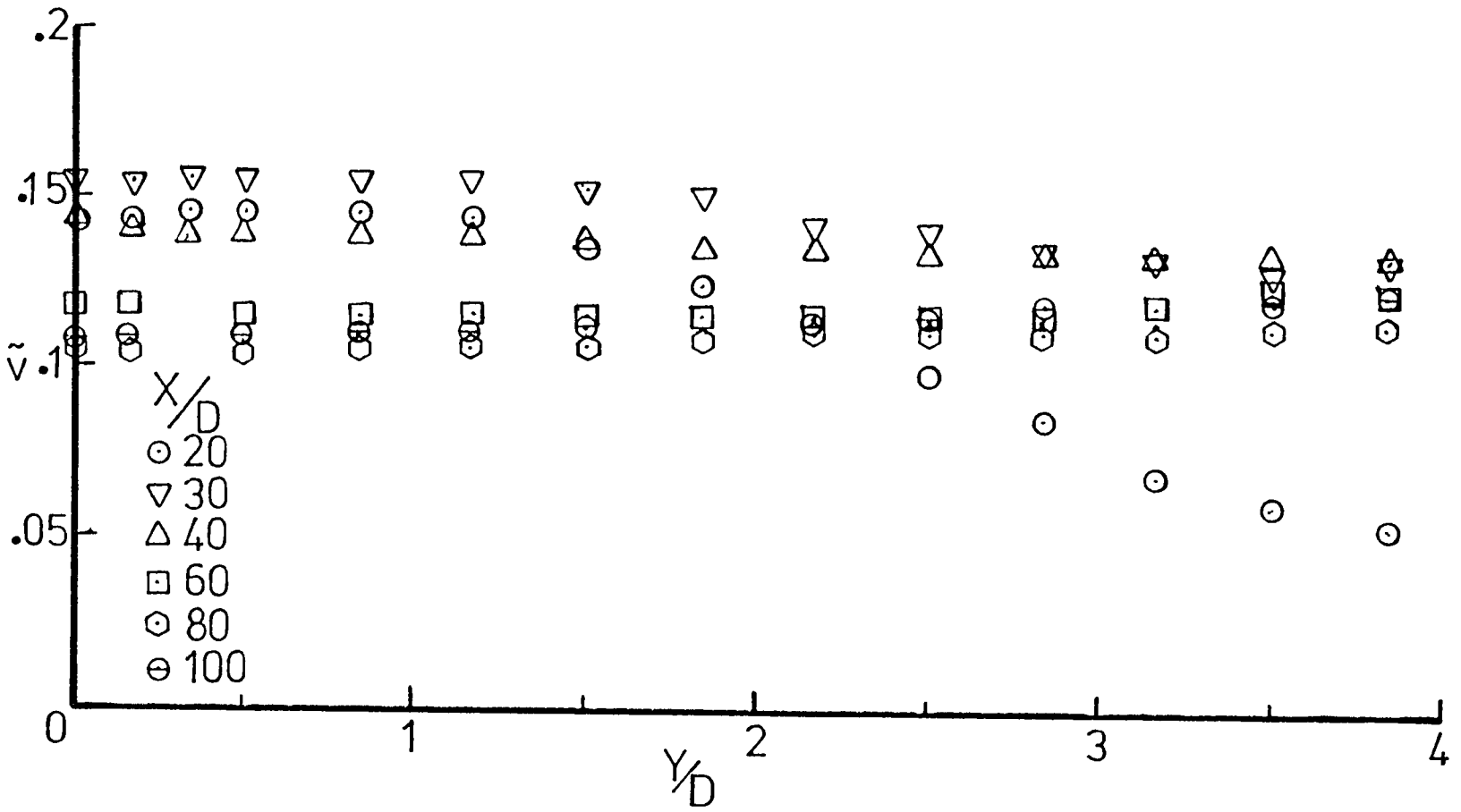

Figure 4.50 The distribution of the lateral velocity fluctuations in the x,y plane

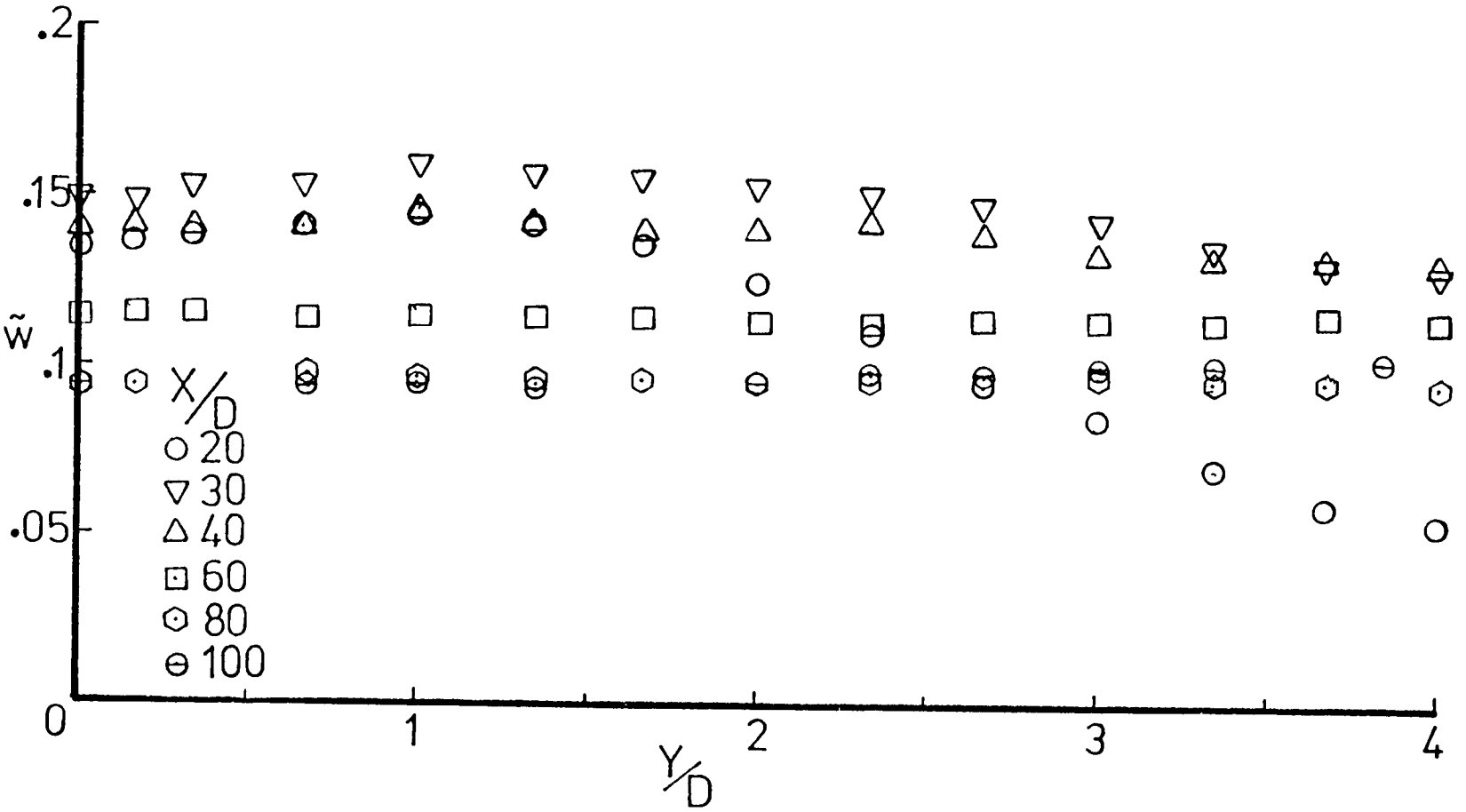

Figure 4.51 The distribution of the transverse velocity fluctuations in the x,y plane

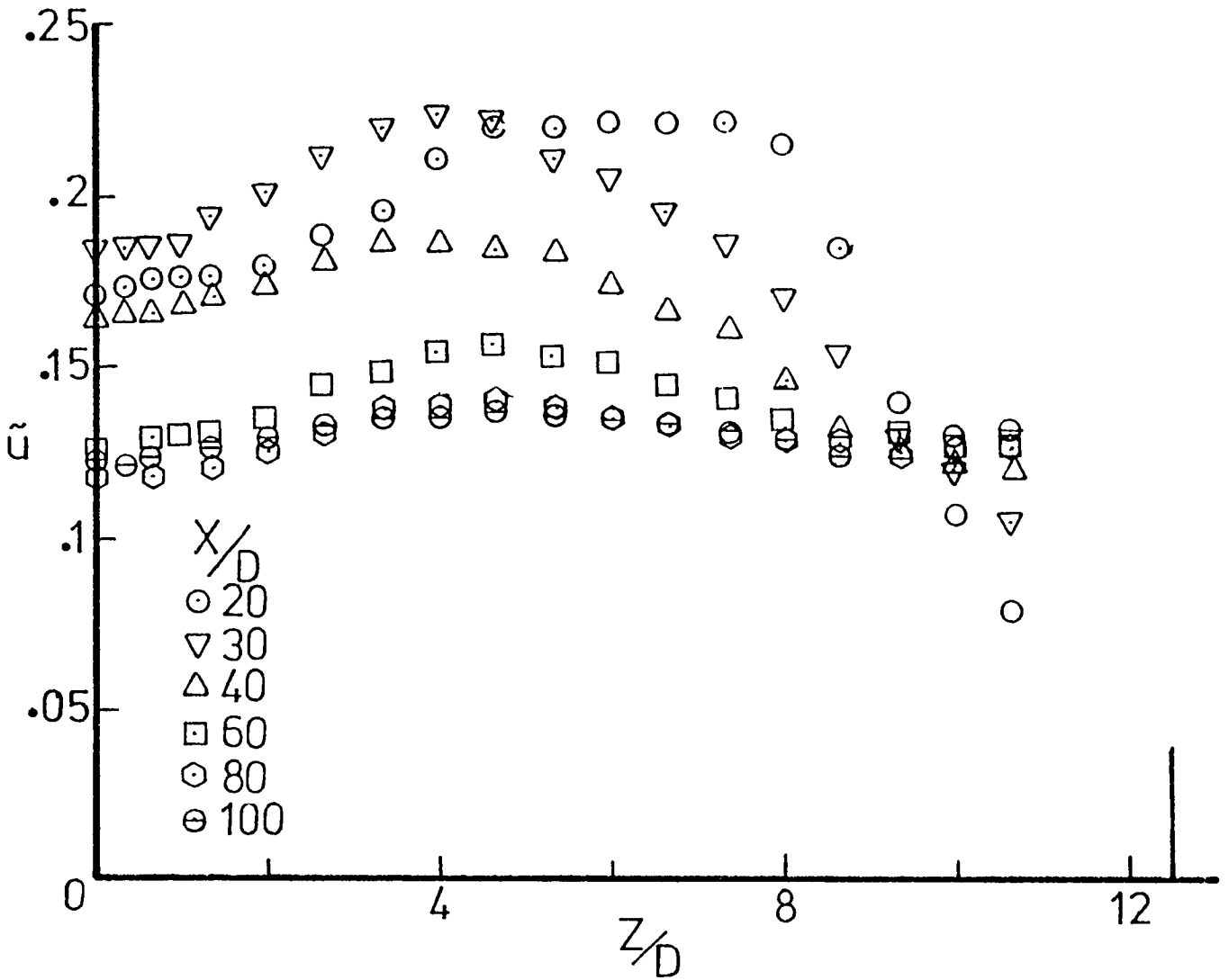

Figure 4.52 The distribution of the axial velocity fluctuations in the x,y plane

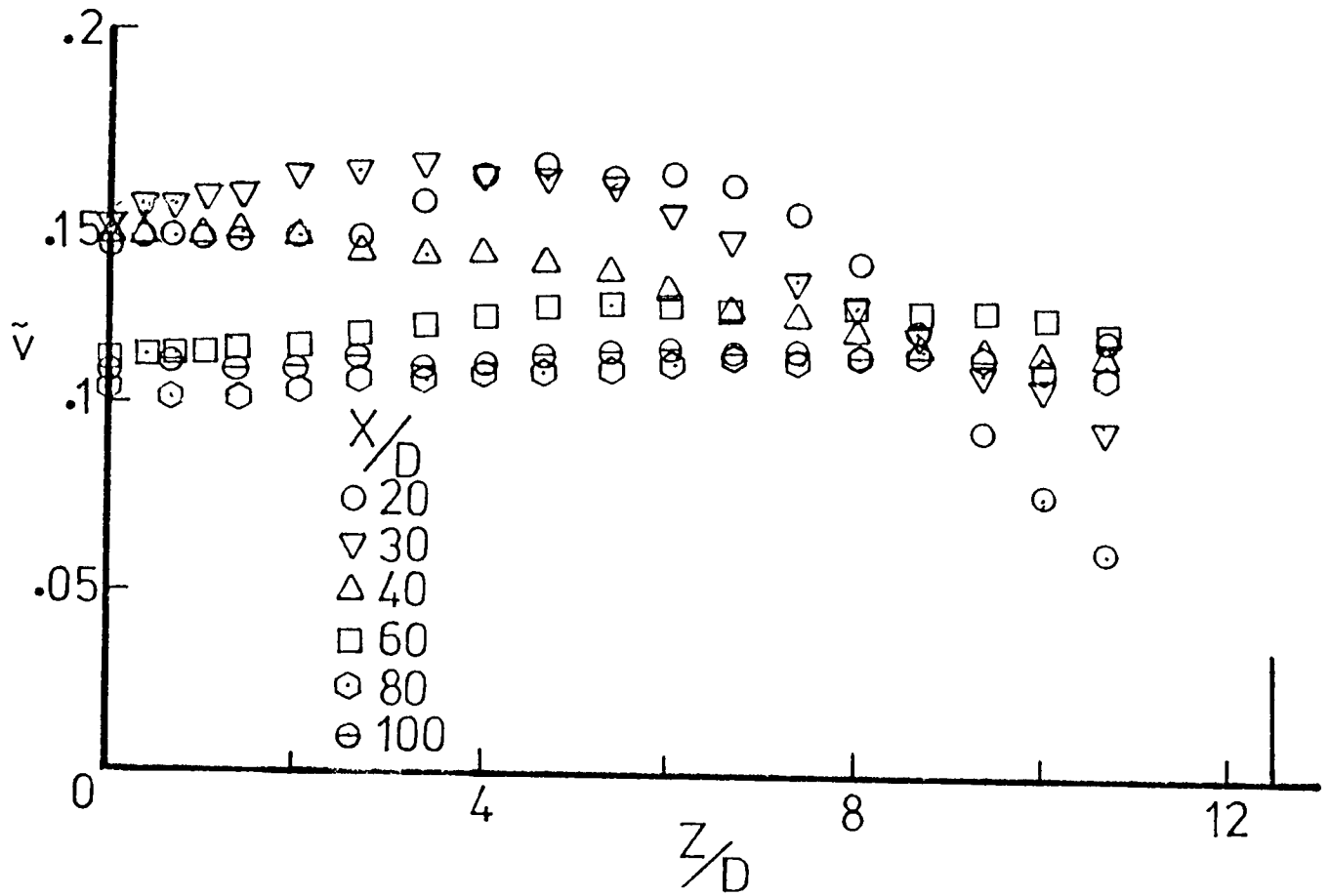

Figure 4.53 The distribution of the lateral velocity fluctuations in the x,z plane

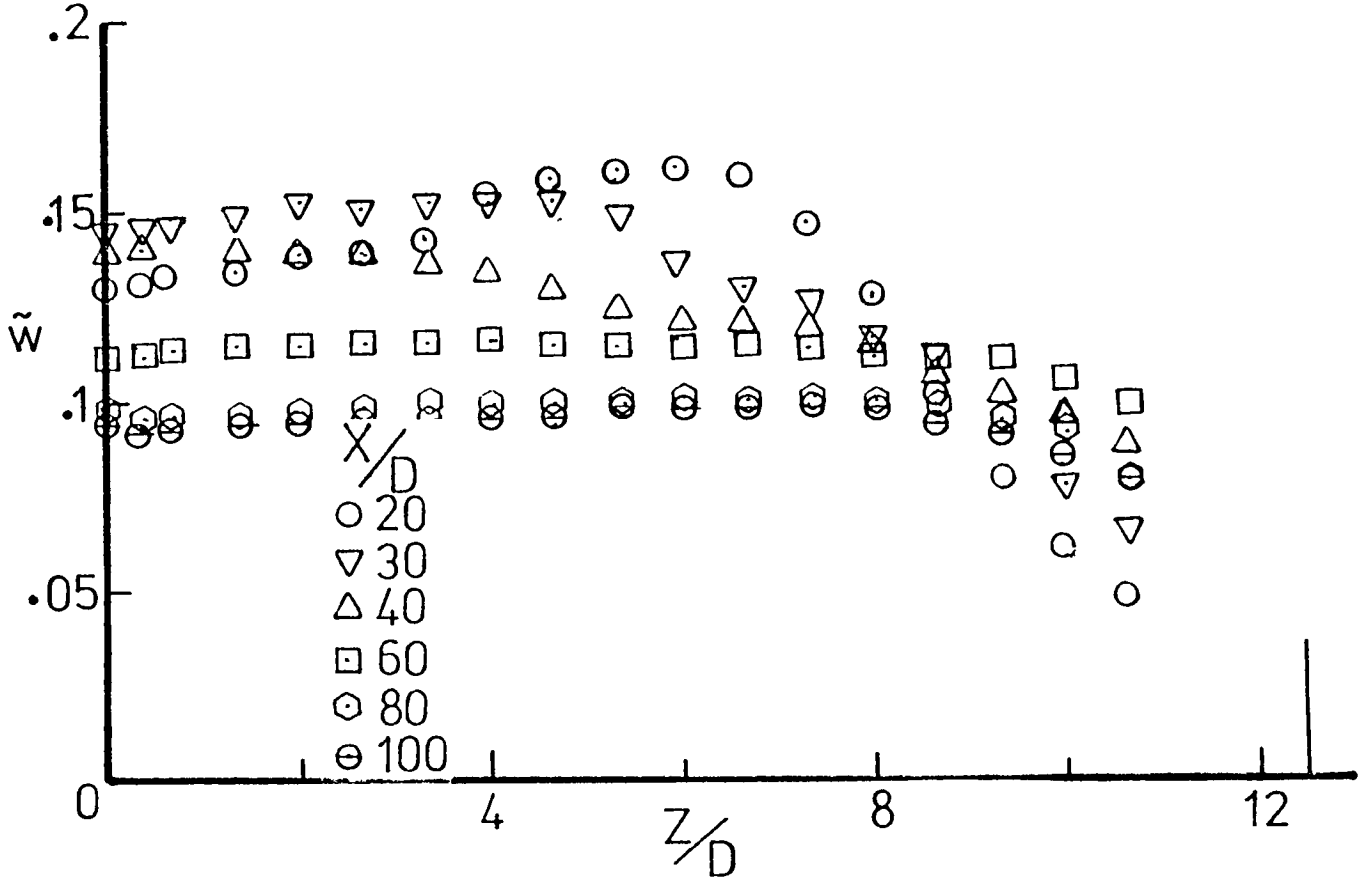

Figure 4.54 The distribution of the transverse velocity fluctuations in the x,z plane

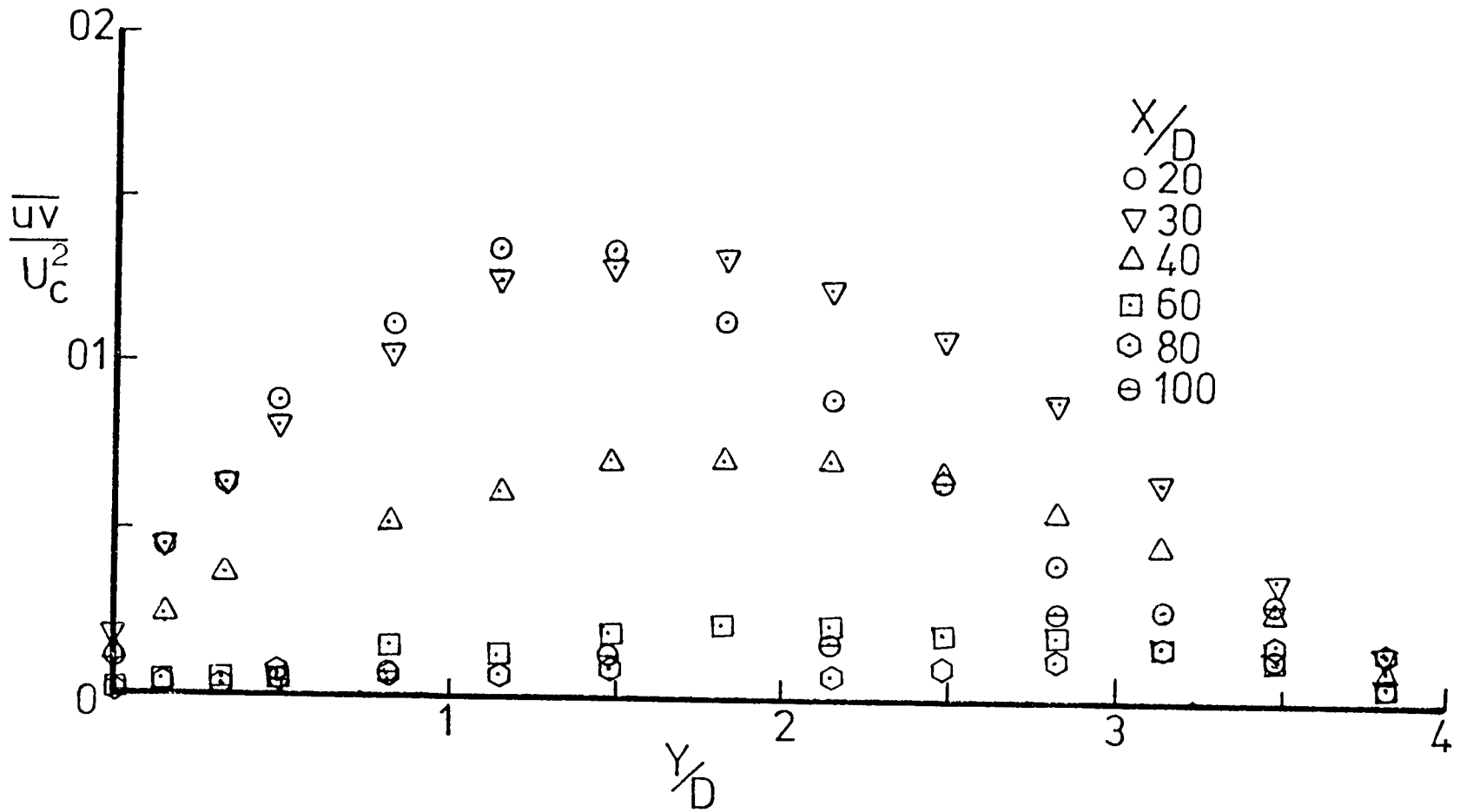

Figure 4.55 The distribution of the turbulent shear stress in the x,y plane

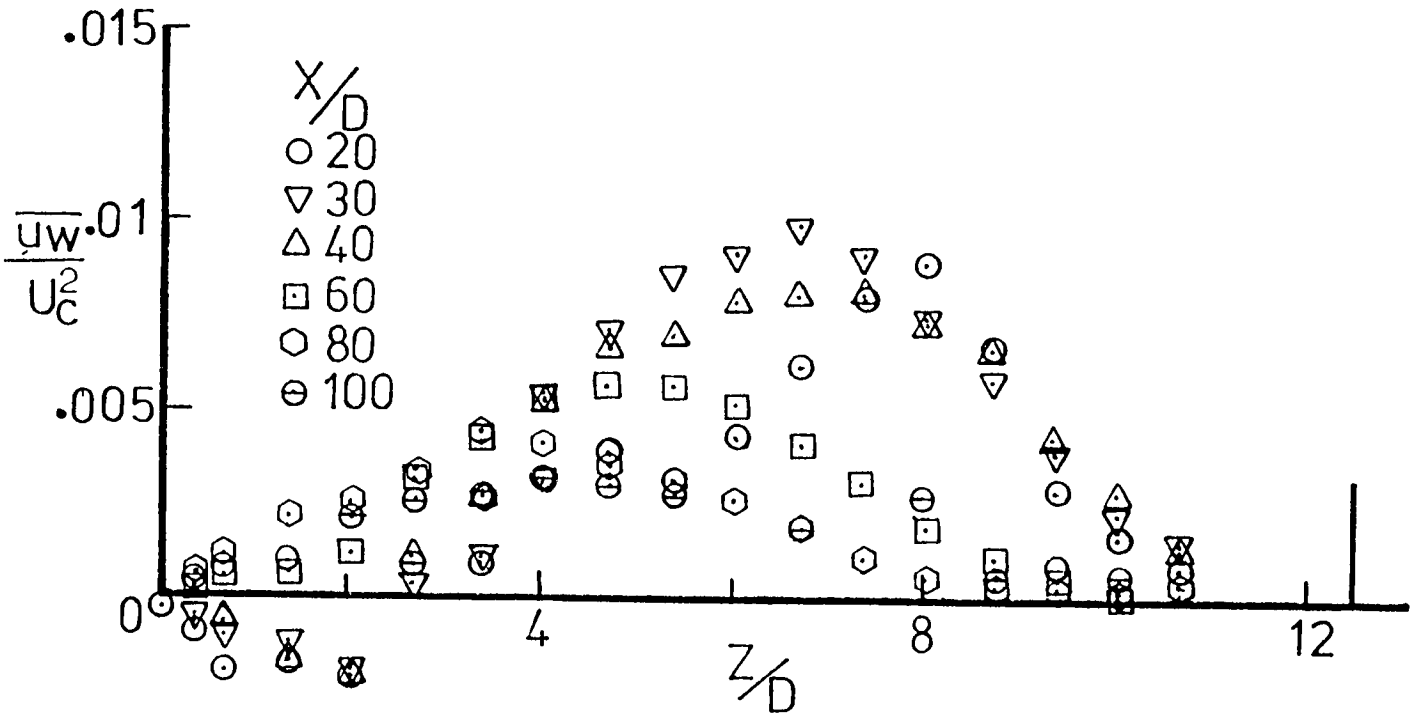

Figure 4.56 The distribution of the turbulent shear stress in the x,z plane

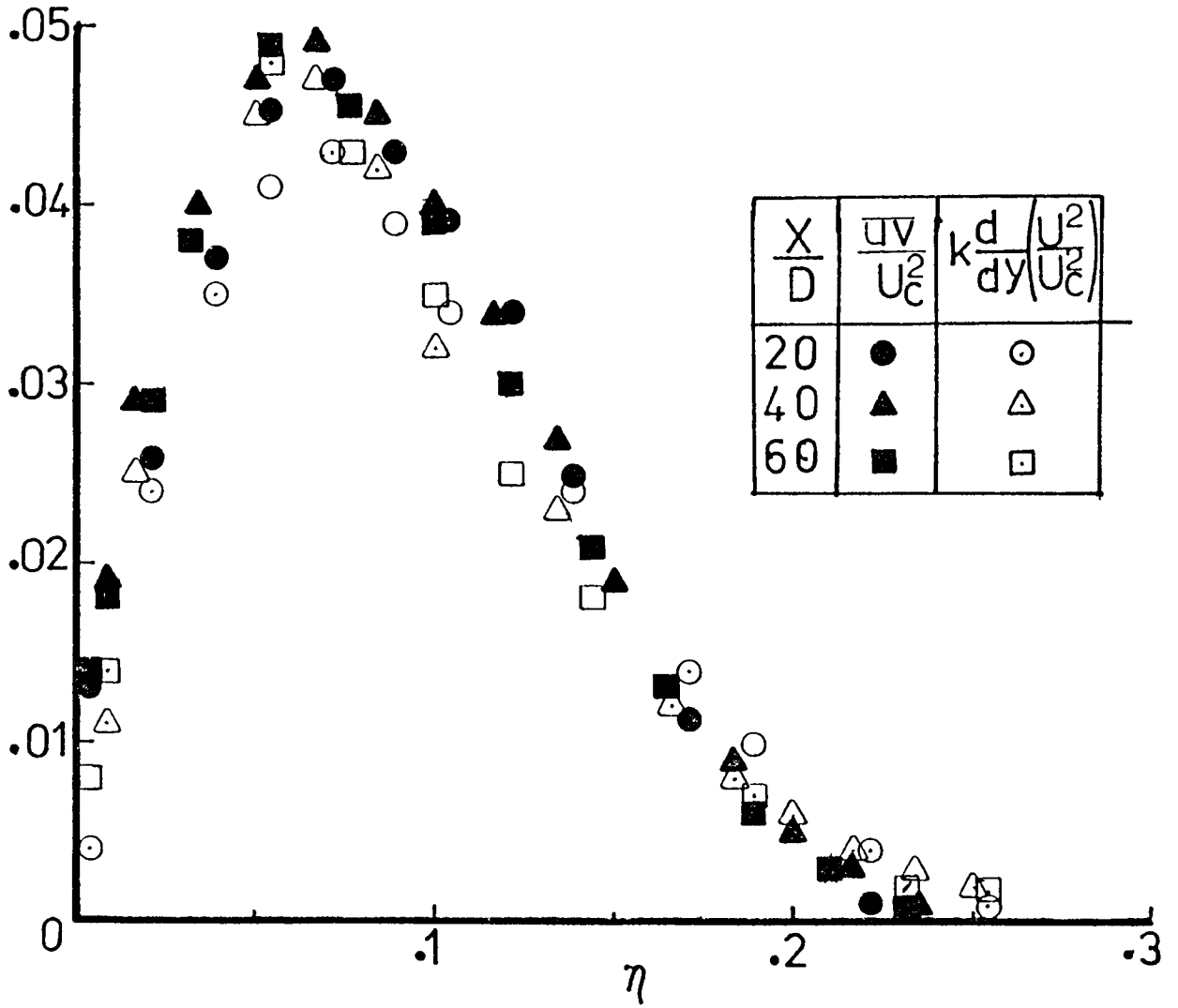

Figure 5.4 Calculation of the Reichardt assumption

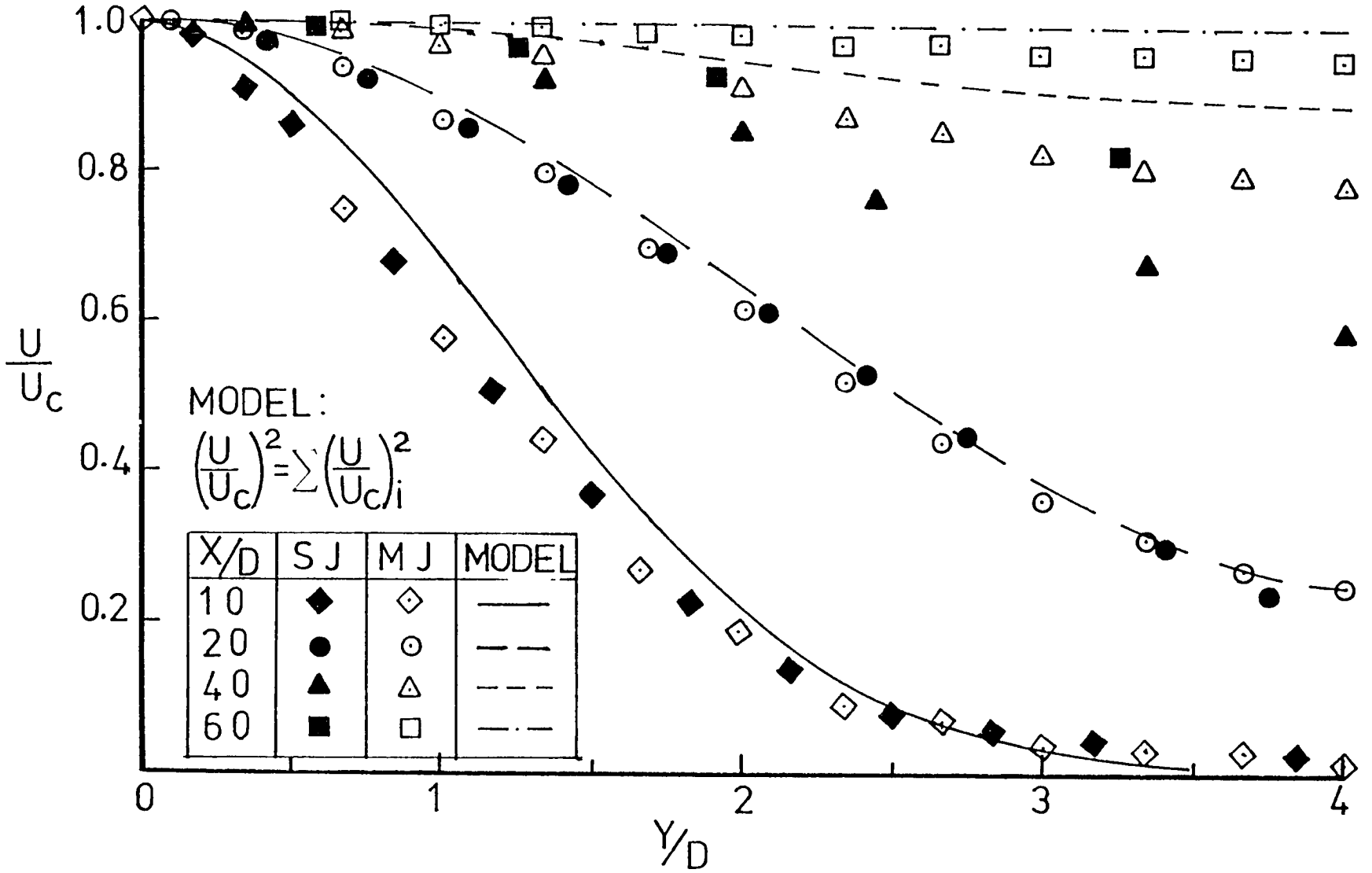

Figure 5.6 Axial mean velocity profiles in the x,y plane

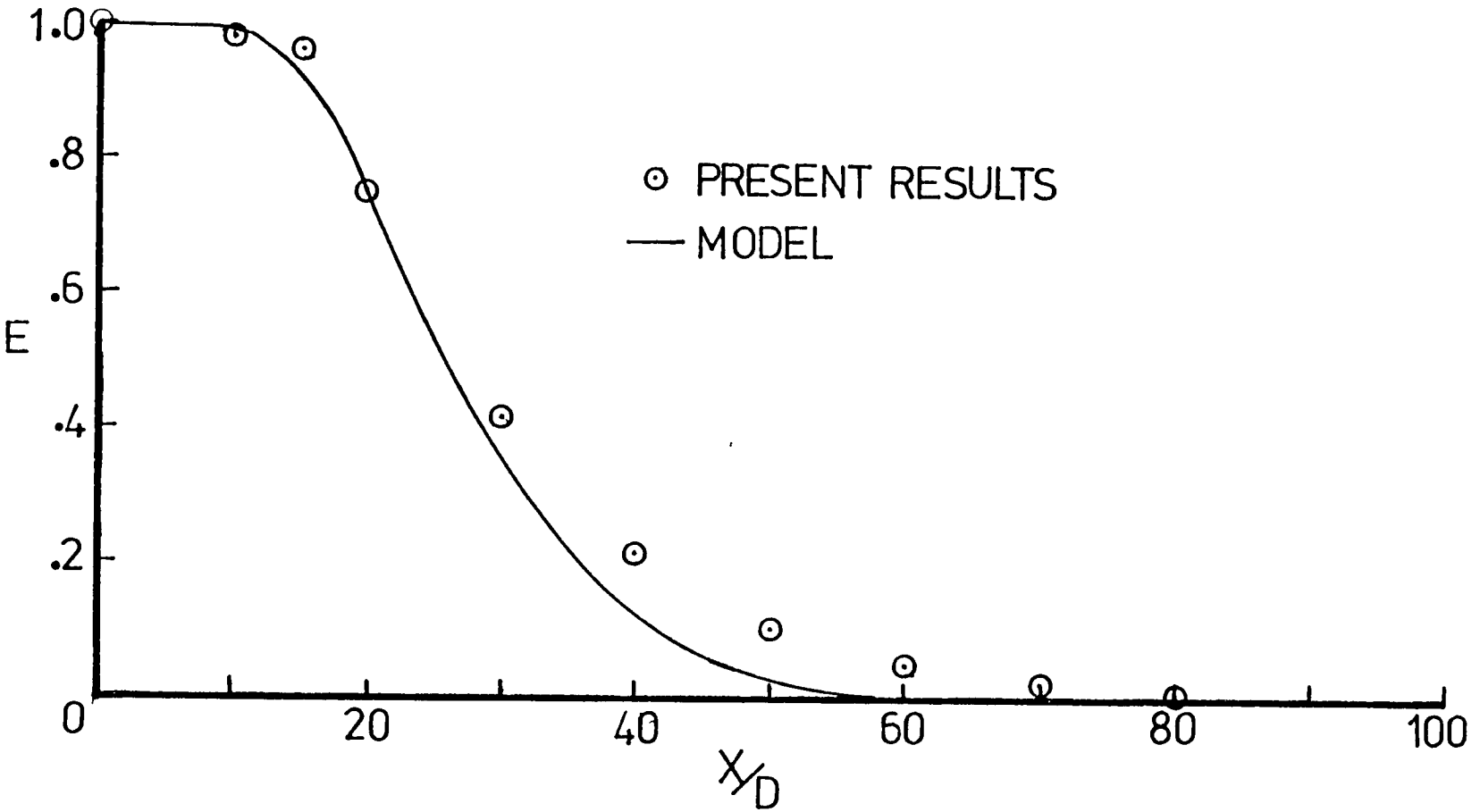

Figure 5.7 The variation of the velocity defect with downstream distance

End of Document